2019

Three-dimensional modeling of fusion yield in plasma jet-driven magneto-inertial fusion

Kevin John Schillo

THREE-DIMENSIONAL MODELING OF FUSION YIELD IN PLASMA JET-DRIVEN MAGNETO-INERTIAL FUSION

by

KEVIN JOHN SCHILLO

A DISSERTATION

Submitted in partial fulfillment of the requirements
for the degree of Doctor of Philosophy in Aerospace Systems Engineering
in
The Department of Mechanical and Aerospace Engineering
of
The School of Graduate Studies
of
The University of Alabama in Huntsville

HUNTSVILLE, ALABAMA

2019

In presenting this dissertation in partial fulfillment of the requirements for a doctoral degree from The University of Alabama in Huntsville, I agree that the Library of this University shall make it freely available for inspection. I further agree that permission for extensive copying for scholarly purposes may be granted by my advisor or, in his/her absence, by the Chair of the Department or the Dean of the School of Graduate Studies. It is also understood that due recognition shall be given to me and to The University of Alabama in Huntsville in any scholarly use which may be made of any material in this dissertation.

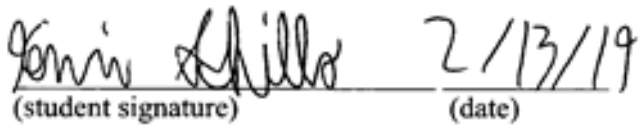

(student signature) (date)

DISSERTATION APPROVAL FORM

Submitted by Kevin Schillo in partial fulfillment of the requirements for the degree of Doctorate of Philosophy in Aerospace Systems Engineering and accepted on behalf of the Faculty of the School of Graduate Studies by the dissertation committee. We, the undersigned members of the Graduate Faculty of The University of Alabama in Huntsville, certify that we have advised and/or supervised the candidate on the work described in this dissertation. We further certify that we have reviewed the dissertation manuscript and approve it in partial fulfillment of the requirements for the degree of Doctorate of Philosophy in Aerospace Systems Engineering.

Dr. Jason Cassibry (Date) 1/14/19 Committee Chair

Dr. Gabe Xu (Date) 2/18/19

Dr. Babak Shotorban (Date) 2/13/19

Dr. Sarma Rani (Date) 01/14/2019

Dr. Mark Gilmore (Date) 2/18/19

Dr. Keith Hollingsworth (Date) 2/19/19 Department Chair

Dr. Shankar Mahalingam (Date) 02/20/19 College Dean

Dr. David Berkowitz (Date) 4/9/19 Graduate Dean

ABSTRACT
The School of Graduate Studies
The University of Alabama in Huntsville

Degree Doctor of Philosophy College/Dept. Engineering/Mechanical and Aerospace Engineering

Name of Candidate Kevin Schillo
Title Three-Dimensional Modeling of Fusion Yield in Plasma Jet-Driven Magneto-Inertial Fusion

Controlled nuclear fusion in a laboratory is a challenging problem. After more than half a century of research, no fusion reactor has been developed that is capable of generating more energy than what is required to operate the reactor. Creating accurate simulations of the fusion plasma conditions at peak compression is crucial to guide the development of future fusion experiments and ultimately determine what is necessary to create a viable fusion reactor.

This dissertation presents an investigation into three-dimensional simulations of neutron and alpha particle yield of deuterium-tritium fusion. An overview of the physics of nuclear fusion presents the attractive features of the deuterium-tritium reaction. This is followed by an overview of fusion confinement methods, with magneto-inertial fusion shown to offer a wide parameter space. The exploration of this parameter space has led to many concepts, with one being plasma jet-driven magneto fusion (PJMIF), the focus of this dissertation. A power balance study and Lindl-Widner diagrams were constructed to determine what conditions are necessary to achieve breakeven in an unmagnetized and magnetized deuterium-tritium target. This analysis was then used to determine what conditions to simulate in the three-dimensional smooth particle hydrodynamic code SPFMax. Among the cases simulated in SPFMax were an unmagnetized target, a

magnetized target, a target with a cold afterburner, and a target with predefined surface non-uniformities superimposed by spherical harmonics. The yield and gain are presented for each of these cases, with an examination of what factors enhance and degrade the yield. Finally, concluding remarks and suggestions for future areas of research are presented.

Abstract Approval: Committee Chair 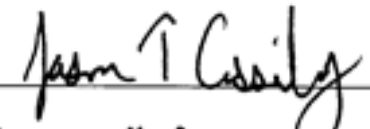

Department Chair 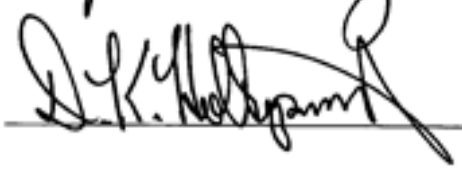

Graduate Dean 

ACKNOWLEDGEMENTS

I would first like to thank my advisor Dr. Jason Cassibry for his ceaseless support of me throughout my graduate studies. I have learned more in my time working with him than I have at any other point in my life. I remain in awe of his commitment and passion for the wide and diverse projects he works on, which made it all the more commendable when he took the time to help me with whatever I might have been struggling with. My dissertation research has been of immense benefit not only to my career, but my personal life as well. Of particular note is the fall of 2014, when Dr. Cassibry arranged for me to work at HyperV Technologies in Chantilly, Virginia as part of my dissertation research. By happenstance, this was located near much of my extended family, including my now deceased paternal grandfather, to whom this dissertation is dedicated. My time at HyperV serendipitously allowed me to be with my grandfather in the last month of his life. No words can do justice to the gratitude I have for Dr. Cassibry.

This work was supported by DOE Award Number DE-Ar0000566, and I will be forever grateful for having been given this incredible opportunity.

Thanks are also given to Scott Hsu, Francis Thio, Doug Witherspoon, and the other members of the PLX-α team. To work with such a brilliant group of engineers on this project is an honor that I shall always cherish.

I owe thanks to all of the members of my committee as well. The feedback from Dr. Rani, Dr. Shotorban, Dr. Xu, and Dr. Gilmore was invaluable in improving my dissertation and polishing it into its finalized form.

I would also like to thank Dr. Frederick, Anthony Edmondson, and the other members of the Propulsion Research Center for helping to make my time as a graduate student among the most enjoyable years of my life. I toured the PRC when I was an undergraduate during a conference in 2009 and was immediately captivated. Seeing the equipment and capabilities of the lab is what enticed me to apply to the University of Alabama in Huntsville for graduate school in the hope of being involved with such an extraordinary part of the nation's propulsion community. Coming to Huntsville will always be one of the best decisions I have made in my life.

Even though the research I did for him was in a completely different field, I also want to thank Dr. Steven Howe for giving me the opportunity to work at the Center for Space Nuclear Research. That invaluable experience greatly expanded my knowledge base and skillset in nuclear engineering, which continues to benefit my ongoing research at UAH.

I owe so much of my success and happiness to the love and support of my family. I want to thank my sisters Mary, Katie, and Megan for tolerating me over all these years and supporting my endeavors. I'll always appreciate my brother Mark for understanding me . I strive to be a good role model for my nephews Michael and Jac and hope that they will one day read and appreciate this dissertation, as well as my other works.

I cannot thank my parents enough for everything they have done for me. They always encouraged me to pursue my interests and dreams, and never once failed support me when I faced crushing failure and disappointment. And of course I must thank them for believing me when I said I would finish my PhD in a timely manner.

I also want to thank all of my aunts, uncles, and cousins for their support and understanding of the importance of what I do and mourn for those who are not here to read this.

Finally, I would like to thank Emily for everything she's done for me. We met during what I believed was the last phase of my dissertation research and stuck with me even after seeing what I'm really like and grown closer to me than anyone has ever been. Before I met you, I had no idea what crucial component was missing from my life. You have helped me grow as a person more than I ever thought possible, opening my eyes to what true happiness is. I love you Emily. I look forward to being your husband.

TABLE OF CONTENTS

PAGE

LIST OF FIGURES ..... **xii**

LIST OF TABLES ..... **xix**

LIST OF SYMBOLS ..... **xx**

CHAPTER 1 INTRODUCTION **1**

1.1 Fusion Criteria 4

1.1.1 Lawson Criterion 4

1.1.2 Triple Product 9

1.2 Fusion Confinement Methods 11

1.2.1 Inertial Electrostatic Confinement 11

1.2.2 Fission-Fusion Hybrids 13

1.2.3 Magnetic Confinement Fusion 13

1.2.4 Inertial Confinement Fusion 14

1.2.5 Magneto-Inertial Fusion 16

CHAPTER 2 MAGNETO-INERTIAL FUSION **21**

2.1 Introduction 21

2.2 Fusion Propulsion 21

2.3 Solid Liner 27

2.3.1 Z-Pinch 28

2.3.2 Inverse Z-Pinch 36

2.4 Liquid Liner 38

2.5 Macron Liner 40
2.6 Plasma Jet-Driven Magneto-Inertial Fusion 41
CHAPTER 3 PJMIF STUDIES 43
3.1 Introduction 43
3.2 PJMIF Propulsion Systems 46
3.3 PJMIF Modeling Studies 48
3.4 PJMIF Experiments 59
3.5 Summary of PJMIF Modeling Studies 61
CHAPTER 4 NUMERICAL MODEL 64
4.1 Introduction 64
4.2 Equations of Motion 65
4.3 Stopping Power 68
4.4 Nonlocal Radiation Transport in SPFMax 69
4.5 Smoothed Particle Hydrodynamics 73
4.5.1 First and Second Order Derivatives 77
4.5.2 Shock Capturing 80
CHAPTER 5 CODE VERIFICATION 82
5.1 Introduction 82
5.2 Optically Thin Radiation Cooling 83
5.3 Thermal Conduction 85
5.4 Couette Flow 93
5.5 Gresho Vortex 96
5.6 Oblique Shock 102

5.7 Taylor-Green Vortex 107

5.8 Fusion Yield 110

CHAPTER 6 FUSION POWER BALANCE 116

6.1 Introduction 116

6.2 Alpha Particle Energy Deposition 117

6.3 Neutron Energy Deposition 119

6.4 Lindl-Widner Diagrams 120

CHAPTER 7 THREE-DIMENSIONAL FUSION SIMULATIONS 127

7.1 Introduction 127

7.2 Baseline Target Case 129

7.2.1 Magnetized Target 138

7.3 Target and Afterburner Cases 140

7.3.1 Magnetized Target and Afterburner 141

7.4 Non-Uniform Cases 156

7.4.1 Spherical Harmonics 156

7.4.2 Non-uniform Unmagnetized Target 159

7.4.3 Non-uniform Magnetized Target and Afterburner 168

CHAPTER 8 CONCLUSIONS 177

REFERENCES 181

LIST OF FIGURES

Figure Page

Figure 1.1. Reactivity of controlled fusion reactions. 3

Figure 1.2. Lawson criterion of controlled fusion reactions. 8

Figure 1.3. Triple product of controlled fusion reactions. 10

Figure 1.4. IEC chamber [11]. 12

Figure 1.5. ITER concept [16]. 14

Figure 1.6. National Ignition Facility [19]. 15

Figure 1.7. Parameter space for MCF, MIF, and ICF [15]. 17

Figure 2.1. Comparison of initial spacecraft mass and transit times for roundtrip Mars mission [15]. 23

Figure 2.2. Orion vehicle concept [34]. 24

Figure 2.3. Icarus interstellar probe concept [43]. 25

Figure 2.4. Collision of FRC plasmoid with lithium liner in FIREBALL concept [44] 26

Figure 2.5. LANL FRX-L [48]. 28

Figure 2.6. MagLIF concept [52]. 30

Figure 2.7. PUFF target compression [55] 32

Figure 2.8. PUFF system [56]. 33

Figure 2.9. Z-pinch vehicle configuration [57]. 33

Figure 2.10. Charger-1 pulsed power machine [58]. 34

Figure 2.11. Z-pinch fusion propulsion concept [26]. 35

Figure 2.12. Pulsed magnetic nozzle [15] 36

Figure 2.13. Inverse Z-pinch [66]. 37
Figure 2.14. General Fusion's acoustically driven MTF concept [70]. 38
Figure 2.15. SLC fusion reactor concept [71]..... 39
Figure 2.16. Macron former liner reactor concept [72]. 40
Figure 3.1. Plasma jet induced magneto inertial fusion concept [75]..... 43
Figure 3.2. Stages of target and liner compression [24]. 45
Figure 3.3. HOPE conceptual vehicle design [27]..... 47
Figure 4.1. Rays shown in a computational domain for a) a spherical MIF target and liner with b) 4π ray. 70
Figure 4.2. The three methods used for calculating density in SPH [43]. 74
Figure 4.3. SPH particle approximations in a two-dimensional problem domain Ω with a surface S [117]. 76
Figure 5.1. Plasma temperature as a function of time. Solid lines indicate exact numerical solution and data points are SPFMax results. 85
Figure 5.2. Initial conditions for heat conduction problem with cylindrical symmetry. .. 87
Figure 5.3. Temperature profile at different times for heat conduction problem with cylindrical symmetry. Solid lines indicate exact numerical solution and dotted lines are SPFMax results. 88
Figure 5.4. Temperature L^2 norm for heat conduction problem in cylindrical symmetry.89
Figure 5.5. Initial condition for heat conduction problem in spherical geometry. 91
Figure 5.6. Temperature slice comparison of SPH solution with exact numerical solution for heat conduction problem with spherical symmetry. Solid lines indicate exact numerical solution and dotted lines are SPFMax results. 92

Figure 5.7. L^2 norm at different times for heat conduction problem with spherical symmetry. 93

Figure 5.8. Incompressible Couette flow velocity profile. 94

Figure 5.9. L^2 norm for Couette flow velocity. 95

Figure 5.10. Gresho vortex pressure contour. 97

Figure 5.11. Gresho vortex azimuthal velocity contour. 98

Figure 5.12. SPFMax Gresho vortex simulation, with vectors indicating direction of flow. 99

Figure 5.13. L^2 norm for Gresho vortex pressure. 100

Figure 5.14. L^2 norm for Gresho vortex azimuthal velocity. 101

Figure 5.15. Scatter plot of jet temperature for the oblique shock test at 0, 5, and 10 μs. The jets intersect with a merging half angle of 10 degrees, with the shock visible at the jet-jet interface. 105

Figure 5.16. Taylor-Green Vortex velocity vectors at a) 0 s and b) 5 s. 109

Figure 5.17. Taylor-Green Vortex pressure contour at a) 0 s and b) 5 s. 109

Figure 5.18. L^2 norm for Taylor-Green a) temperature and b) velocity. 110

Figure 5.19. Initial fusion target configuration. 111

Figure 5.20. Fusion energy yield of SPFMax and ode45. 112

Figure 5.21. Neutron yield of SPFMax and ode45. 113

Figure 5.22. Loglog plot of fusion yield self-convergence. 114

Figure 6.1. Lindl-Widner diagram for varying radii and no magnetic field. 121

Figure 6.2. Lindl-Widner diagram for 1 mm radius target and varying magnetic fields. 122

Figure 6.3. Ion gyroradius for 1 mm target for different magnetic field intensities and plasma temperatures..... 123
Figure 6.4. Ratio of target radius to ion gyroradius for 1 mm target for different magnetic field intensities and plasma temperatures. 124
Figure 6.5. Lindl-Widner diagram for varying radii and 1,000 T magnetic field..... 125
Figure 7.1. Baseline target case temperature (left) and mass density (right) at a) t=0 ns, b) t=0.5 ns, c) t=1 ns, and d) t=2 ns..... 131
Figure 7.2. Fusion power production and power losses from expansion and Bremsstrahlung radiation. 132
Figure 7.3. a) Total fusion energy yield and b) total neutron yield for baseline target case. 134
Figure 7.4. 2D slice of temperature (left) and mass density (right) at a) t=0 ns, b) t=0.5 ns, c) t=1 ns, and d) t=2 ns. 135
Figure 7.5. Temperature line slices through target taken at 0, 0.5, 1, and 2 ns. 136
Figure 7.6. Density line slices through target taken at 0, 0.5, 1, and 2 ns. 137
Figure 7.7. Total fusion energy yield for magnetized and unmagnetized target cases. .. 139
Figure 7.8. Total neutron yield for magnetized and unmagnetized target cases..... 140
Figure 7.9. Magnetized target and afterburner case initial a) temperature and b) mass density. 141
Figure 7.10. 2D slice for magnetized target and afterburner case initial a) temperature and b) mass density..... 142
Figure 7.11. Magnetized target and afterburner case a) temperature s and b) mass density at t=2 ns..... 143

Figure 7.12. 2D slice for magnetized target and afterburner case a) temperature and b) mass density at t=2 ns. 144
Figure 7.13. Magnetized target and afterburner case a) temperature s and b) mass density at t=5 ns. 145
Figure 7.14. 2D slice for magnetized target and afterburner case a) temperature and b) mass density at t=5 ns. 145
Figure 7.15. Magnetized target and afterburner case a) temperature s and b) mass density at t=13 ns. 146
Figure 7.16. 2D slice for magnetized target and afterburner case a) temperature and b) mass density at t=13 ns. 147
Figure 7.17. Temperature line slices through magnetized target and afterburner taken at 0, 2, 5, and 13 ns. 148
Figure 7.18. Density line slices through magnetized target and afterburner taken at 0, 2, 5, and 13 ns. 149
Figure 7.19. Fusion power production and power losses from expansion, Bremsstrahlung, and cyclotron radiation. 150
Figure 7.20. Total fusion energy yield for magnetized target/afterburner and unmagnetized target cases. 151
Figure 7.21. Total neutron yield for magnetized target/afterburner and unmagnetized target cases. 152
Figure 7.22. Temperature line slices for a) unmagnetized target, b) magnetized target, c) unmagnetized target and afterburner, and d) magnetized target and afterburner. 154

Figure 7.23. Density line slices for a) unmagnetized target, b) magnetized target, c) unmagnetized target and afterburner, and d) magnetized target and afterburner. 155
Figure 7.24. Visual representation of spherical harmonics taken from [151]. 158
Figure 7.25. Non-uniform unmagnetized target with l=2, m=1, and amplitude=0.5 initial a) temperature s and b) mass density. 160
Figure 7.26. 2D slice for perturbed unmagnetized target case with l=2, m=1, and amplitude=0.5 initial a) temperature s and b) mass density..... 161
Figure 7.27. Non-uniform unmagnetized target with l=2, m=1, and amplitude=0.5 initial a) temperature s and b) mass density at t=1 ns. 162
Figure 7.28. 2D slice for perturbed unmagnetized target case with l=2, m=1, and amplitude=0.5 initial a) temperature s and b) mass density at t=1 ns..... 162
Figure 7.29. Non-uniform unmagnetized target with l=2, m=1, and amplitude=0.5 initial a) temperature s and b) mass density at t=2 ns. 163
Figure 7.30. Non-uniform unmagnetized target with l=2, m=1, and amplitude=0.5 initial a) temperature s and b) mass density at t=3 ns. 163
Figure 7.31. 2D slice for non-uniform unmagnetized target case with l=2, m=1, and amplitude=0.5 initial a) temperature s and b) mass density at t=2 ns..... 164
Figure 7.32. 2D slice for non-uniform unmagnetized target case with l=2, m=1, and amplitude=0.5 initial a) temperature s and b) mass density at t=3 ns..... 165
Figure 7.33. Fusion energy yield for non-uniform target with l=2, m=1, and amplitude=0.5. 166
Figure 7.34. Neutron yield for non-uniform target with l=2, m=1, and amplitude=0.5 . 167

Figure 7.35. Magnetized target with l=2, m=1, and amplitude=0.5 and uniform afterburner initial a) temperature and b) mass density. 168
Figure 7.36. 2D slice of non-uniform magnetized target with l=2, m=1, and amplitude=0.5 and uniform afterburner initial a) temperature and b) mass density. 169
Figure 7.37. Magnetized target with l=2, m=1, and amplitude=0.5 and uniform afterburner a) temperature and b) mass density at t=5 ns. 170
Figure 7.38. 2D slice of non-uniform magnetized target with l=2, m=1, and amplitude=0.5 and uniform afterburner a) temperature and b) mass density at t=5 ns. 171
Figure 7.39. Magnetized target with l=2, m=1, and amplitude=0.5 and uniform afterburner a) temperature and b) mass density at t=13 ns. 171
Figure 7.40. 2D slice of non-uniform magnetized target with l=2, m=1, and amplitude=0.5 and uniform afterburner a) temperature and b) mass density at t=13 ns. 172
Figure 7.41. Total fusion energy yield for non-uniform target and uniform afterburner. 173
Figure 7.42. Total neutron yield for non-uniform target and uniform afterburner. 174

LIST OF TABLES

Table Page

Table 3.1. Summary of PJMIF modeling studies. 62

Table 5.1. Summary of oblique shock test cases with particle numbers varying from 1386 to 33,728 particles per jet. The exact solution for a stationary ramp gives 12.23 degrees shock angle, and post shock density, temperature, and Mach number of 7.24×10^{-3} kg/m^3, 55054 K, and 10.13, respectively. 106

Table 7.1. Initial conditions of fusion simulations. 128

Table 7.2. Initial conditions and fusion yield for baseline case. 138

Table 7.3. Simulation results for baseline target and afterburner cases. 155

Table 7.4. Simulation results for non-uniform unmagnetized target. 167

Table 7.5. Initial conditions for non-uniform magnetized target and uniform afterburner cases. 175

Table 7.6. Simulation results for non-uniform magnetized target and uniform afterburner cases. 175

LIST OF SYMBOLS

SYMBOL	DEFINITION
A	Particle property
AW	Atomic weight
a	Spherical harmonic amplitude
a_1	Constant for quadratic von Neumann-Richtmyer artificial viscosity
a_2	Constant for linear von Neumann-Richtmyer artificial viscosity
B	Magnetic field
C	Convergence constant
C_v	Heat capacity at constant volume
c	Speed of light
$\frac{de_i}{dt}$	Change in ion energy
$\frac{de_e}{dt}$	Change in electron energy
$\frac{dN_{fus}}{dt}$	Fusion reaction rate
$d\boldsymbol{r}'$	Differential volume element
E_α	Alpha particle energy
E_n	Neutron energy
E_F	Fusion energy
E_k	Initial kinetic energy of fusion product species
e	Specific internal energy
F	Function on a spherical surface

F_0	Fourier modulus
f_n	Neutron fractional power deposition
f_α	Fraction of alpha particle energy deposited in hot spot
$f(v)$	Distribution function of relative velocities
f_l^m	Coefficients of spherical harmonics on spherical surface function
h	Radius of influence
k	Spherical harmonic wave number
k_B	Boltzmann constant
$k_{\perp,e}$	Electron thermal conductivity perpendicular to magnetic field
l	Spherical harmonic degree
l_α	Alpha particle mean free path
l_n	Average neutron mean free path
$\ln \Lambda$	Coulomb logarithm
M	Mach number
m	Spherical harmonic order
m_e	Electron mass
m_i	Ion mass
m_p	Proton mass
n	Number density
n_e	Electron number density
n_i	Ion number density
P_B	Bremsstrahlung power

P_C	Cyclotron power
P_{dif}	Diffusion power
P_E	Average volumetric thermal conduction power
P_F	Fusion power
P_{ion}	Ion deposition power
P_l^m	Associated Legendre polynomial function
p	Pressure
p_e	Electron pressure
p_i	Ion and neutral particle pressure
p_r	Ram pressure
Q_e	Electron heating from fusion reactions
Q_{ei}	Electron/ion equilibration term
Q_i	Ion heating from fusion reactions
q	Charge
$\boldsymbol{r}$	Particle position
r_L	Larmor radius
T	Temperature
T_e	Electron temperature
T_i	Ion and neutral particle temperature
$\boldsymbol{u}$	Vector velocity field
V	Volume
v	Relative velocity

$v_{\alpha 0}$	Velocity of 3.5 MeV alpha particle
W	Smoothing kernel function
x	Hall parameter
x_s	Post-shock x-axis position in which 50% of peak pressure is located
Y_{ph}	Matrix of normalized spherical harmonics Y_l^m
Y_l^m	Spherical harmonic function
Z	Charge state
z_s	Post-shock z-axis position in which 50% of peak pressure is located
α	Diffusivity
β	Shock angle
γ	Specific heat ratio
δ	Delta function
δW_{ir}	Work done by a fast ion
η_ν	Spectral energy emission per mass
θ	Polar angle with respect to the z axis
κ	Smoothing function constant at a given location
λ	Spherical harmonic wavelength
μ	Viscosity coefficient
ν	Frequency
ξ	Convergence value
Π_1	Quadratic von Neumann-Richtmyer artificial viscosity
Π_2	Linear von Neumann-Richtmyer artificial viscosity

ρ	Mass density
ρ_b	Particle density
σ	Cross section
$\boldsymbol{\tau}$	Deviatoric viscous stress tensor
$\tau_{\alpha e}$	Alpha particle energy deposition time
τ_e	Electron collision time
χ_{Planck}	Single group Planck emission opacity
ϕ	Azimuthal angle measured from the x-axis
Ω	Solid angle subtended by ray

To my grandfather Richard Schillo, on whose deathbed I promised that I would become the next Dr. Schillo.

"*It is difficult to say what is impossible, for the dream of yesterday is the hope of today and the reality of tomorrow.*"

—*Robert Hutchings Goddard*

CHAPTER 1

INTRODUCTION

This dissertation presents the results from a three-dimensional numerical modeling technique to simulate energy and neutron yield in a fusion plasma. Generating controlled fusion reactions in a laboratory is a challenging problem, and accurately simulating the plasma is vital in order to guide the development of future experiments. To orient the reader, the first chapter of this dissertation presents the fundamental physics behind nuclear fusion and different engineering concepts that have been or are being explored to develop a viable fusion reactor.

Nuclear fusion is the process by which multiple like-charged atomic nuclei are joined together to form a heavier nucleus. In order for a fusion reaction to occur, two positively charged nuclei must overcome the Coulomb barrier, an energy barrier that results from the electrostatic repulsion of the positively charged nuclei. This barrier can be overcome if the nuclei have sufficiently high temperature and kinetic energy. Quantum tunneling also enables fusion reactions to occur with energies lower than the height of the Coulomb barrier.

Many fusion reactions exist in nature, but only several may be used in reactors. Among the reasons for this limitation is that the fusion fuel isotopes must have large cross sections in order to generate a sufficient reaction rate as given by

$$\frac{dN_{fus}}{dt} = n_1 n_2 \langle \sigma v \rangle V \tag{1.1}$$

with the cross section given by σ being a measure of the number of reactions per target nucleus per unit time when the target is hit by a unit flux of particles. The reactivity $\langle \sigma v \rangle$ is the probability of a fusion reaction per unit time per unit density of target material. Target nuclei move, so the relative velocity is different for each pair, and so the averaged reactivity is needed, which is given by

$$\langle \sigma v \rangle = \int_0^\infty \sigma(v) v f(v)\, dv \tag{1.2}$$

Isotope reactions that may be used in reactors include deuterium-tritium, deuterium-deuterium, deuterium-helium-3, and p-boron-11. The products for each of these reactions are given by

$$D + T \rightarrow {}^4He(3.5\ MeV) + n(14.1\ MeV) \tag{1.3}$$

$$\begin{matrix} D + D \rightarrow T(1.01\ MeV) + p(3.02\ MeV) & 50\% \\ D + D \rightarrow {}^3He(0.82\ MeV) + n(2.45\ MeV) & 50\% \end{matrix} \tag{1.4}$$

$$D + {}^3He \rightarrow {}^4He(3.6\ MeV) + p(14.7\ MeV) \tag{1.5}$$

$$p + {}^{11}B \rightarrow 3\,{}^4He + 8.7\ MeV \tag{1.6}$$

The reactivity for these reactions are shown in Figure 1.1

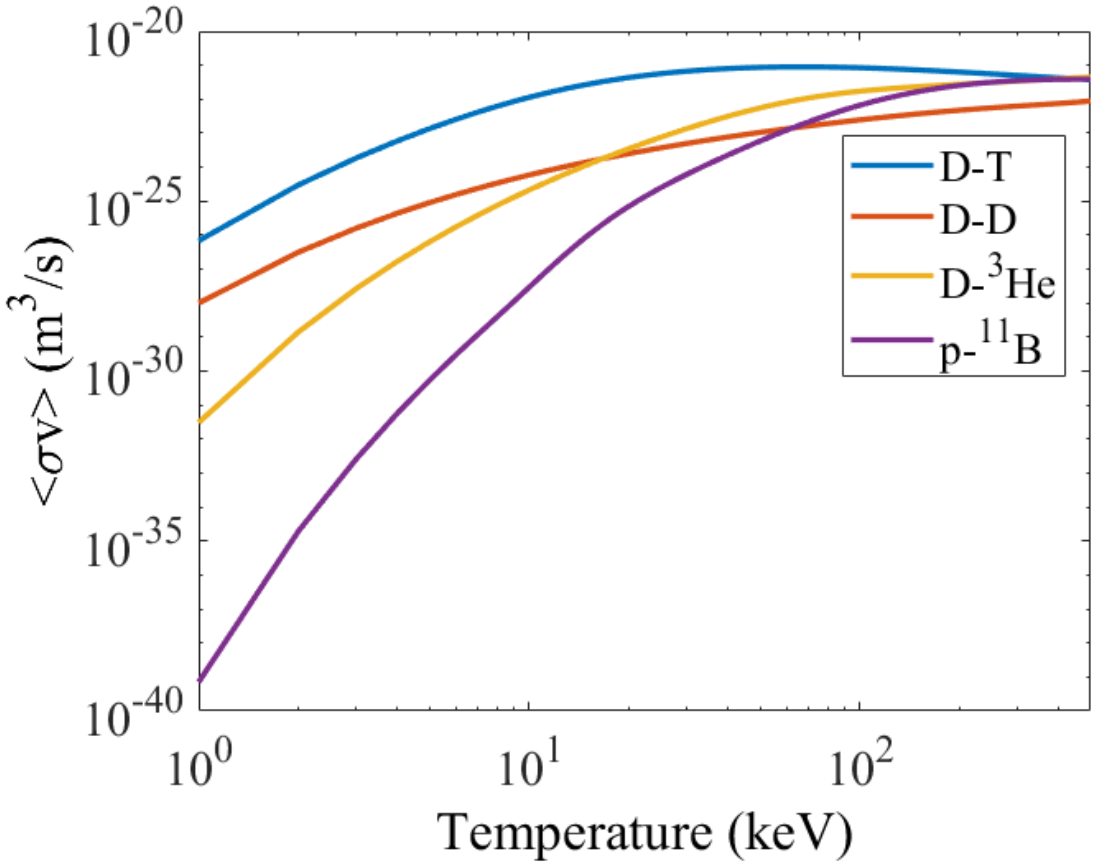

Figure 1.1. Reactivity of controlled fusion reactions.

From this figure, it can be seen that the deuterium-tritium reaction has the highest reactivity at the lowest temperature. This has a major effect on the viability of a fusion reactor design, as will be shown in the following section. For a more complete discussion on advanced fuels, see [1-3].

1.1 Fusion Criteria

Criteria are needed in order to determine the viability of a reactor design based on whether it will be able to achieve thermonuclear ignition and what conditions are required to achieve ignition. Two of these criteria are the Lawson criterion and the triple product, which are discussed in the following subsections for each of the different controlled fusion reactions.

1.1.1 Lawson Criterion

When a fusion reaction occurs, the energy release per unit time per unit volume is given by [4]

$$P_F = n_1 n_2 \langle \sigma v \rangle E_F \tag{1.7}$$

Power losses act against this and impair the viability of a fusion reactor. The Lawson criterion, derived by Lawson in 1955, has often been used to determine what conditions must be met in order for thermonuclear fusion ignition to occur in a reactor. Fusion ignition is a plasma condition in which the fusion products are able to provide sufficient heating to the plasma to maintain fusion conditions against power losses [5]. Sources of power losses include radiation, conduction, and transport across magnetic field lines. For a magnetically confined plasma, the energy confinement time is defined as the time at which the diffusive energy loss equals the total energy content of the plasma, with the total thermal energy of the plasma given by

$$E_{th} = \frac{3}{2}(n_i + n_e)k_B TV \tag{1.8}$$

For a plasma in which $n = n_i = n_e$, the diffusion power loss is

$$P_{dif} = \frac{3k_B TV}{\tau_E} \tag{1.9}$$

Another major source of power loss is radiation emission from Bremsstrahlung, which results from charged particles being deflected by another charged particle's electric field. This radiation can be calculated by first finding the cross section for the emission of photons with energy $h\nu$ by electrons with incident energy v_e and is given by

$$\frac{d\sigma}{d\nu} = \frac{32\pi^2}{3\sqrt{3}} \frac{Z_i^2 q^6}{m_e^2 c^3 v_e^2 h\nu} \tag{1.10}$$

To obtain the spectral emission for a plasma with a Maxwell distribution of free electrons, the velocities are integrated from the lowest velocity sufficient to produce a photon with energy $h\nu$, which is obtained from

$$v_{min} = \sqrt{\frac{2h\nu}{m_e}} \tag{1.11}$$

The spectral energy emission per mass is then given by

$$\eta_\nu = \frac{h\nu}{4\pi A m_p} \int_{v_{min}}^{\infty} dv\, f(v)\, v\, \frac{d\sigma}{d\nu} \tag{1.12}$$

Which can be integrated to give

$$\eta_\nu = \frac{16\pi q^6}{3\sqrt{6\pi} m_e^2 c^3} \frac{Z_i^2 n_e}{\sqrt{\frac{k_B T_e}{m_e}} A m_p} \exp\left(-\frac{h\nu}{k_B T_e}\right) \tag{1.13}$$

The total specific power of Bremsstrahlung radiation per unit mass is then given by

$$P_B = 4\pi \int_0^\infty \eta_\nu \, dv \tag{1.14}$$

This can be integrated to give

$$P_B = \frac{32\pi}{3\sqrt{6\pi}} \frac{q^6}{m_e \hbar c^2} \sqrt{\frac{k_B T_e}{m_e c^2}} \frac{Z_i^3 \rho}{(A m_p)^2} \tag{1.15}$$

When a magnetic field is used in magnetic or magneto-inertial confinement fusion, cyclotron radiation is emitted when charged particles are accelerated by the Lorentz force. This is given by [6, 7]

$$P_C = \frac{4q^2}{3c^3} \frac{k_B T_e}{m_e} \omega_c^2 n_e \tag{1.16}$$

in which

$$\omega_C = \frac{qB}{m_e c} \tag{1.17}$$

Electrons dominate thermal conduction due to their mobility. The electron thermal conductivity perpendicular to a magnetic field is given by

$$k_{\perp,e} = \frac{9.6958 \times 10^3 T_e^{5/2}}{Z \ln \Lambda} \left(\frac{f_{\gamma_1} x^2 + f_{\gamma_0}}{\Delta} \right) \tag{1.18}$$

in which the Hall parameter is given by

$$x = \frac{5.5127 \times 10^{-8} B T_e^{5/2}}{n_e Z^2 \ln \Lambda \, m_e} \tag{1.19}$$

the coefficient Δ is given by

$$\Delta = x^4 + f_{\delta_1} x^2 + f_{\delta_0} \tag{1.20}$$

the four f coefficients are defined as

$$f_{\gamma_0} = 11.92\left(0.10067 + \frac{0.58456}{-0.35 + Z^{1.1}}\right) \tag{1.21}$$

$$f_{\gamma_1} = 4.664\left(0.69683 + \frac{0.30317}{Z}\right) \tag{1.22}$$

$$f_{\delta_0} = 3.7703\left(0.025489 + \frac{0.63343}{-0.35 + Z^{3/2}}\right) \tag{1.23}$$

$$f_{\delta_1} = 14.79\left(0.50588 + \frac{0.40765}{-0.175 + Z}\right) \tag{1.24}$$

The average volumetric thermal conduction power can be modeled as

$$P_E = -\frac{k_e \nabla T_e S}{V} \tag{1.25}$$

For a spherical geometry, this can be approximated as

$$P_E = -\frac{2.91 \times 10^4 T_e^{7/2}}{Z \ln \Lambda R_h^2}\left(\frac{f_{\gamma_1} x^2 + f_{\gamma_0}}{\Delta}\right) \tag{1.26}$$

The Lawson criterion requires for the fusion heating to be greater than all of the losses, expressed by

$$\frac{1}{4} n^2 \langle \sigma v \rangle E_F \geq \frac{3 n k_B T}{\tau_E} \tag{1.27}$$

This can be rearranged as

$$n \tau_E \geq \frac{12 k_B}{E_F} \frac{T}{\langle \sigma v \rangle} \tag{1.28}$$

The Lawson criterion for each of the four examined fusion reactions is shown in Figure 1.2

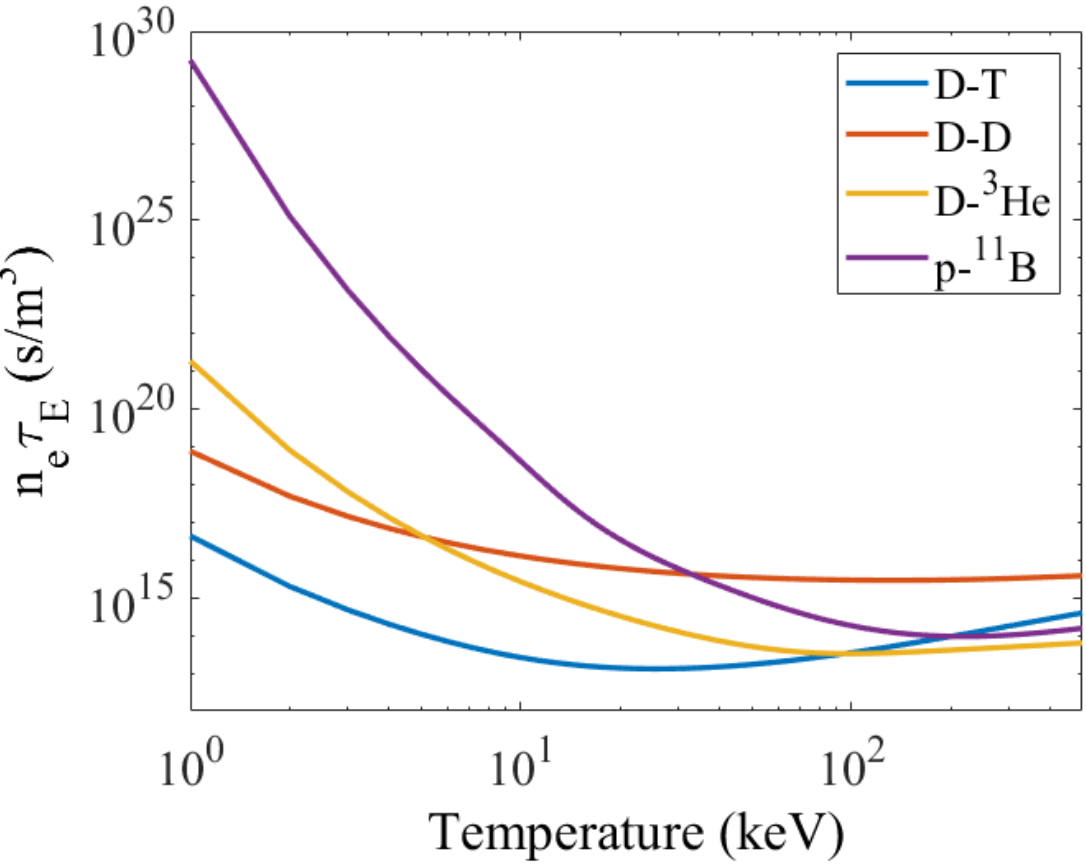

Figure 1.2. Lawson criterion of controlled fusion reactions.

The deuterium-tritium reaction can be seen to achieve a minimization of the Lawson criterion at the lowest temperature due to the high cross section shown in Figure 1.1. This, coupled with the triple product described in the following subsection, makes the deuterium-tritium reaction particularly attractive for fusion research.

1.1.2 Triple Product

The product of a fusion plasma's density, confinement time, and temperature is another useful figure of merit for the design of fusion reactors. The triple product inequality is given by

$$n\tau_E T \geq \frac{12k_B}{E_F}\frac{T^2}{\langle\sigma v\rangle} \tag{1.29}$$

If a fusion reactor has a triple product greater than the value on the right side of the inequality, then the fusion energy generated by the reactor will be greater than the energy needed to generate and confine the fusion plasma. This achievement has not yet been made in any fusion reactor.

The triple product for each of the four examined fusion reactions is shown in Figure 1.3

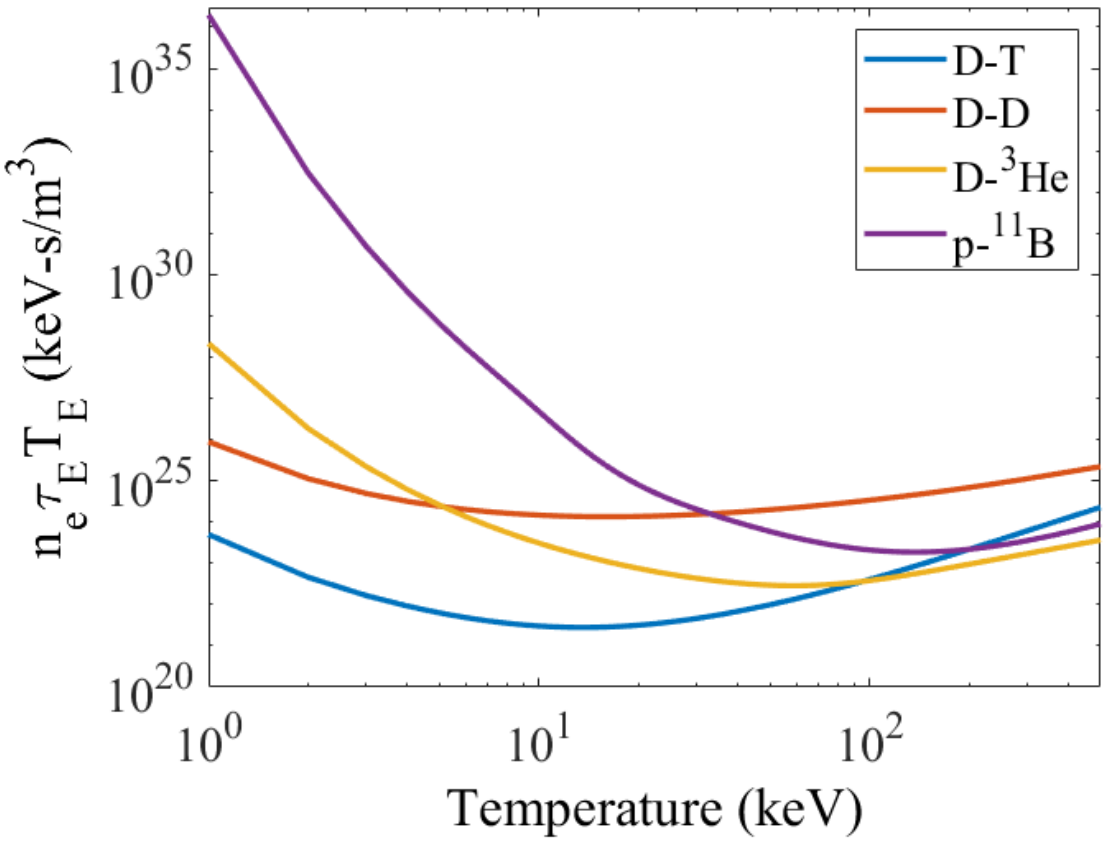

Figure 1.3. Triple product of controlled fusion reactions.

This figure shows that the deuterium-tritium reaction has the lowest triple product at the lowest temperature, which occurs at 14 keV, with this temperature being equivalent to 162.47 million Kelvin. The low triple product of the D-T reaction makes this reaction particularly attractive for reactor design. However, for completeness, some of the challenges associated with the D-T reaction should be discussed. As shown in Equation 1.3, the D-T reaction produces a 3.5 MeV alpha particle and a 14.1 MeV neutron. As will be shown in Chapter 6, neutrons deposit very little energy in fusion plasmas, and so alpha particles are the main source of self-heating.

In addition, tritium has a half-life of 12.32 years and must be produced by neutron activation of lithium-6 in nuclear reactors in the reaction

$$^{6}Li + n \rightarrow {}^{4}He + T + 4.86\ MeV \tag{1.30}$$

Alternatively, tritium may be produced from the interaction of high-energy neutrons with lithium-7 in the endothermic reaction

$$^{7}Li + n \rightarrow {}^{4}He + T + n - 2.87\ MeV \tag{1.31}$$

Another difficulty with the D-T reaction is that the neutrons produced can cause neutron activation and damage to reactor materials.

Despite these obstacles, the D-T reaction remains attractive to researchers due to its high reactivity and low triple product. It is for this reason that the focus of this dissertation is on simulating fusion in a deuterium-tritium plasma.

1.2 Fusion Confinement Methods

Decades of research have led to many different concepts for confining plasma and bringing it to conditions necessary to initiate nuclear fusion. These include inertial electrostatic confinement, inertial confinement, magnetic confinement, magneto-inertial confinement, and fission-fusion hybrids.

1.2.1 Inertial Electrostatic Confinement

In inertial electrostatic confinement (IEC), a spherical electrostatic field is used to create a potential well to confine fusion fuel ions [8]. The high voltage accelerates the ions

toward the center of the field, where they collide and undergo fusion reactions [9]. Many IEC devices are of low enough cost and complexity that many universities and hobbyists are able to assemble and operate them. However, the IEC method has thus far proven unable to bring fusion fuel to thermonuclear conditions, and so the plasma within IEC apparatuses has non-thermal energy distributions. This causes many power losses as the ions that are hot enough to undergo fusion collide with other, colder ions that will be unable to undergo fusion reactions. This major obstacle has proven difficult for IEC researchers to overcome [10].

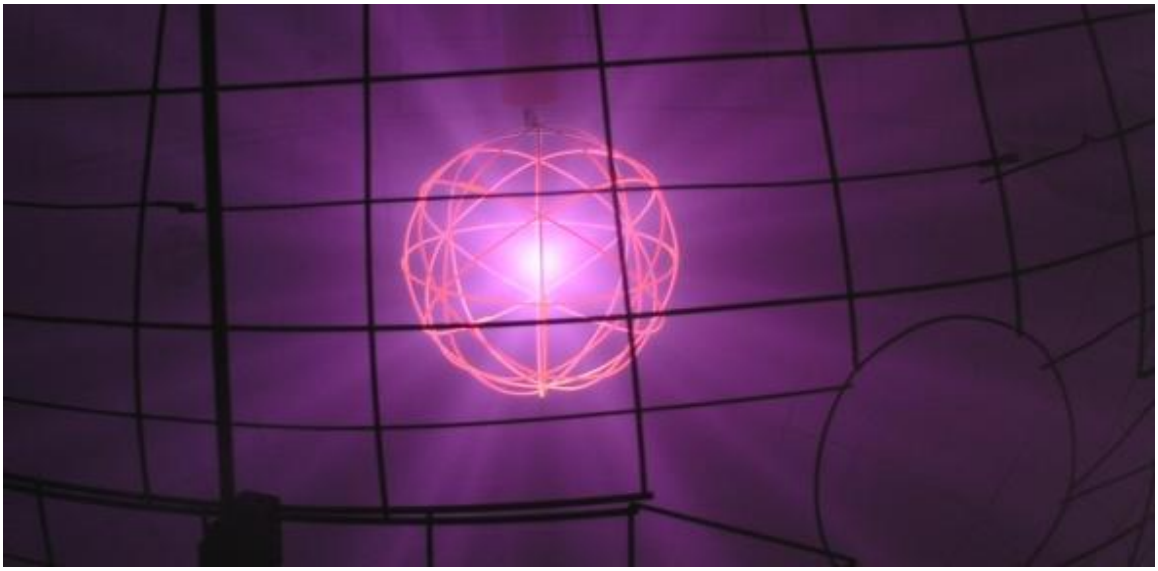

Figure 1.4. IEC chamber [11].

1.2.2 Fission-Fusion Hybrids

A fission-fusion hybrid consists of fusion fuel plasma surrounded by a liner that may consist of thorium, natural uranium, or depleted uranium. A mechanism such as a laser or particle beam initiates fusion reactions in the plasma. High-energy neutrons generated by the fusion reactions then initiate fission reactions in the surrounding liner, causing the liner to implode on the plasma. This increases the plasma's density and temperature, which releases more fusion neutrons that further amplify the fission reaction rates in the liner. This continues until a detonation wave propagates through the system [12, 13]. Research on using fission-fusion hybrids for power generation or propulsion has been restricted due to their weapons applications.

1.2.3 Magnetic Confinement Fusion

Magnetic confinement fusion (MCF) uses strong magnetic fields to confine low-density plasmas in a large volume reactor. For MCF, the ion density of the plasma is on the order of $\sim 10^{15}$ cm^{-3}, the plasma may occupy a volume in the range hundreds of cubic meters, and the reactor has continuous steady-state operation over long time frames. The magnetic fields keep the ions from touching the material of the walls, which reduces thermal losses. The International Thermonuclear Experimental Reactor (ITER) is one of the most ambitious MCF projects ever pursued and seeks to produce 500 MW of fusion power in a tokamak reactor with a fusion gain of about 10 with operating times of 300-500

seconds [14]. Other magnetic fusion energy (MFE) concepts include dynamic mirrors, spherical toruses, spheromaks, and field reversed configurations (FRC) [15].

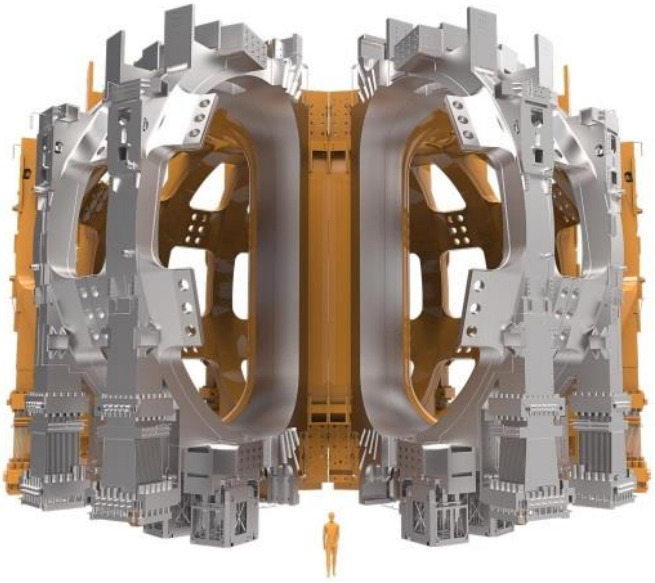

Figure 1.5. ITER concept [16].

1.2.4 Inertial Confinement Fusion

Inertial confinement fusion (ICF) uses a spherically symmetric distribution of high-energy laser pulses or heavy ion beams to compress a target of fusion fuel. The implosion of the target has five stages, which consist of ablation, implosion, stagnation, ignition, and burn. Laser energy is deposited into the outer layer of the target during the first phase. This ablates the outermost layer of the target and causes the remaining material to implode. Shock waves then form, and once these shock waves reach the inner layer of the target, the

power of the laser is increased. The pressure then peaks, at which point the majority of the target's plastic layer has been removed. The inner material then reaches the center of the target, and a hot spot is created that has a pressure and temperature great enough for fusion reactions to occur. These conditions last for tens of piocseconds, during which ignition occurs, and a burn wave is generated that flows outward and consumes the surrounding fuel layer of the target [4, 15]. One of the most ambitious ICF projects is the National Ignition Facility (NIF) operated by the Lawrence Livermore National Laboratory. NIF is the largest and most energetic laser facility ever built and seeks to achieve fusion ignition with deuterium-tritium fuel [17, 18].

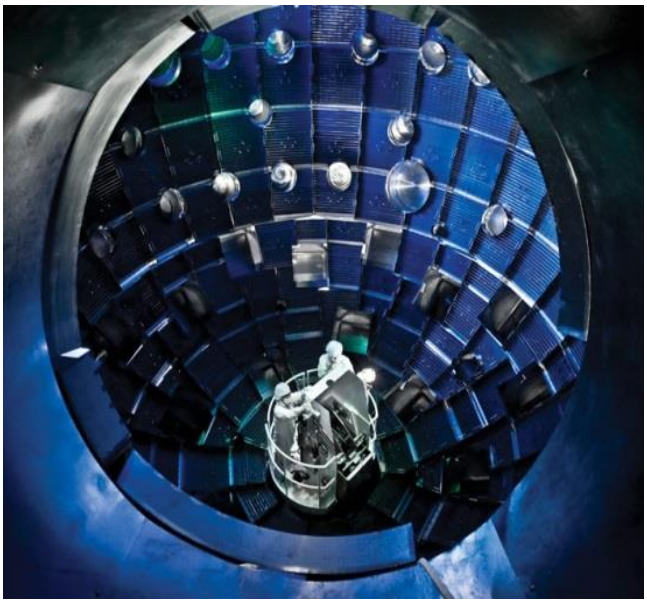

Figure 1.6. National Ignition Facility [19].

1.2.5 Magneto-Inertial Fusion

In magneto-inertial fusion (MIF), a strong magnetic field is used to implode a liner onto a fusion fuel target until fusion reactions occur [20, 21]. There are four stages of target compression in MIF. In the first stage, a seed magnetic field is generated inside the fusion target. This magnetic field provides the fusion fuel with thermal insulation from the plasma liner. As the magnetic field is compressed, the plasma pressure is also increased, which provides heating of the fuel. The strength of the magnetic field is increased as the temperature and pressure of the fuel increase [22]. There are limits for the maximum convergence ratio of the compression, and this makes it necessary for the seed magnetic fields to be large enough such that a field strength in the mega-gauss range will reached upon compression [23].

The plasma conditions in which magneto-inertial fusion operates exist in the density and energy parameter space between MCF and ICF, with MIF requiring lower densities than what is required for ICF and lower plasma energies than MCF requires. This is illustrated in Figure 1.7, with the line plots representing the scaling of a reactor needed for a 10 keV deuterium-tritium plasma to overcome thermal conduction and radiation power losses from electron transport of energy [15]

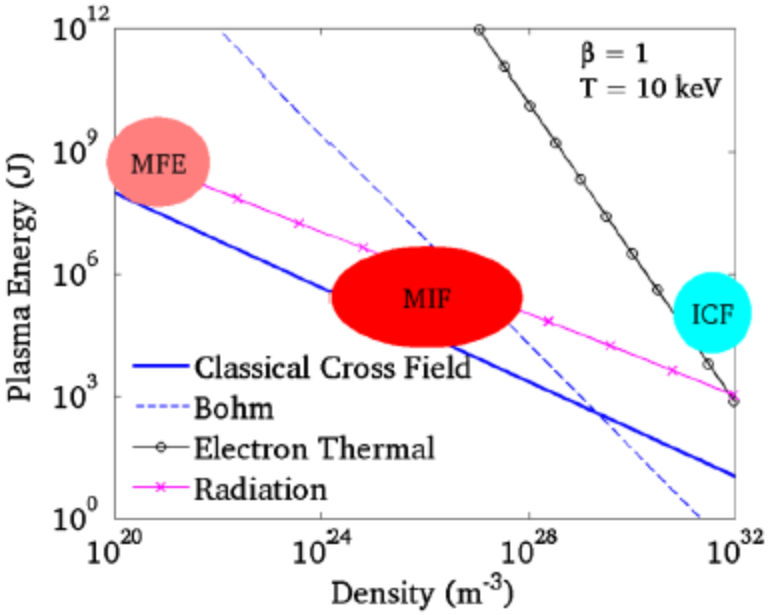

Figure 1.7. Parameter space for MCF, MIF, and ICF [15].

The parameter space that MIF exists within offers several advantages over MCF and ICF methods. Compared to MCF, MIF operates at much higher fuel densities. Fusion reactivity scales as a function of the fuel density squared, allowing for the reactivity rate of MIF to be much higher than that of MCF. An increase in the fuel density also corresponds to a decrease in the characteristic scale-lengths of the fusion plasma, which allows for the reacting volume of an MIF reactor to be much smaller than that needed for an MCF reactor. The magnetic field embedded within the target plasma is greatly enhanced when the target is compressed. This reduces thermal conduction losses and allows the target to be compressed slower than what is required for ICF.

This has a major effect on the size of the fusion reactor, which must be scaled to generate sufficient power from fusion reactions to exceed power losses [15]. MIF enhances

alpha particle self-heating of the fuel while also reducing thermal losses. This helps to reduce the areal density threshold needed for fusion ignition to occur. This in turn allows for lower implosion velocities to be used for the liner, or allowing for higher gain to be achieved for given implosion velocity [24]. This raises the possibility that further development of magneto-inertial concepts could result in much smaller reactor sizes and enable near term development of terrestrial power and spacecraft propulsion systems.

In order for this concept to be feasible, the liner must be sufficiently energetic to compress the target until ignition occurs while also conserving the magnetic flux in a stable manner and confining the target long enough for the fusion yield to exceed the liner driver and target generation energies. The powerful lasers or ion beams needed for ICF require large capacitor banks that would be prohibitively massive for a spacecraft propulsion system. MIF utilizes embedded magnetic fields that lower the amount of power that the drivers must deliver to the fusion target, which in turn can require smaller capacitor banks than what is needed for ICF.

Fusion ignition occurs when the fusion energy released in the form of energetic products such as neutrons and alpha particles is at least partially deposited in the fusion plasma as the particles pass through it. It is not necessary for all fusion concepts, but is necessary for ICF in order for it to be viable. For ignition to occur, the areal density must exceed 0.3 g/cm^2 [25].

In MIF, a critical value required for ignition is the product from the magnetic field strength multiplied by the radius. The magnetic field enhances energy deposition from charged particles and allows for ignition to occur in plasmas with much lower densities than what is required for ICF systems. Because MIF targets are larger and can be imploded

slower than what is required for ICF targets, the power and intensity needed for achieving fusion ignition are orders of magnitude lower than that for ICF. However, for the same mass of fusion fuel, the energy required to achieve ignition is about the same. Ignition of a fusion target requires that the fusion driver simultaneously supply sufficient energy, power, and intensity [15].

Another attractive feature of MIF is that the reduced power and intensity requirements needed for the targets allow pulsed-power machines to be used as drivers for the system. Pulsed power devices are not viable contenders for ICF targets due to their inability to supply the necessary power and intensity needed for ignition to occur in ICF. Pulsed power devices are capable of meeting the requirements for MIF and are more efficient than laser or other beam drivers. This allows lower gain targets to be a viable option for MIF [25].

The primary objective of this dissertation is to present fusion yield in a three-dimensional numerical code and the effect that three-dimensional non-uniformities have on fusion yield. Previous studies that have incorporated burn physics have been limited to one-dimensional codes, making the results of this dissertation paramount to the study of the plasma jet magneto-inertial fusion (PJMIF) concept.

The rest of this dissertation is organized as follows. Chapter 2 reviews different magneto-inertial fusion reactor concepts and applications. Chapter 3 reviews studies of the PJMIF concept, which will be shown to have attractive features for both spacecraft propulsion and terrestrial power. Chapter 4 outlines the governing equations for the fusion plasma and smoothed particle hydrodynamic (SPH) method used to discretize the equations. The specific code utilized in the simulations which implements the SPH method

is Smooth Particle Fluid with Maxwell equation solver (SPFMax) and is described in Chapter 4 as well. Chapter 5 covers a code verification analysis to verify the capability of using SPFMax to accurately simulate test cases that incorporate the physics of radiation cooling, thermal conduction, viscosity, shock capturing, stopping power, and fusion yield. Chapter 6 covers power balance diagrams that were necessary to guide the development of fusion target simulations in the SPFMax code. The results of the SPFMax fusion simulations are then presented in Chapter 7. Additional fusion simulations with non-uniformities on the target surface are also presented in Chapter 7. Finally, conclusions and recommended future research are outlined in Chapter 8.

CHAPTER 2

MAGNETO-INERTIAL FUSION

2.1 Introduction

Many different MIF concepts have been studied, each with their own advantages and disadvantages. These include Z-pinches, inverse Z-pinches, and magnetized target fusion that use macron liners, liquid liners, and plasma liners. The applications for MIF consist primarily of terrestrial power production and spacecraft propulsion. As shown in Chapter 1, the plasma density and energy parameter space for MIF offer favorable scaling for a reactor. This is crucial for the development of a propulsion system, as shown in the next section.

2.2 Fusion Propulsion

In a fusion propulsion system, the plasma exhaust from fusion reactions can be converted directly to thrust, eliminating the need to generate electricity that would be needed for an electric propulsion system. A fusion system would be capable of sending a

spacecraft to the furthest reaches of the solar system and possibly beyond far more rapidly than any other propulsion system that can be expected to be developed.

Studies by Cassibry et al [15], Miernik et al [26], and Adams et al [27] have shown that fusion propulsion rapidly reduces interplanetary trip times when compared to other propulsion systems for spacecraft. This can be seen in the following figure, which compares the initial spacecraft mass in low Earth orbit and the corresponding transit times required for a roundtrip Mars mission for different propulsion systems. It is extremely difficult for a chemical propulsion system to be used for a human piloted mission due to the corresponding long transit times. Nuclear thermal and nuclear electric propulsion systems could allow for two-year manned Mars mission. A fusion propulsion system with specific powers of 1-10 kW/kg could enable roundtrip Mars missions lasting less than a year.

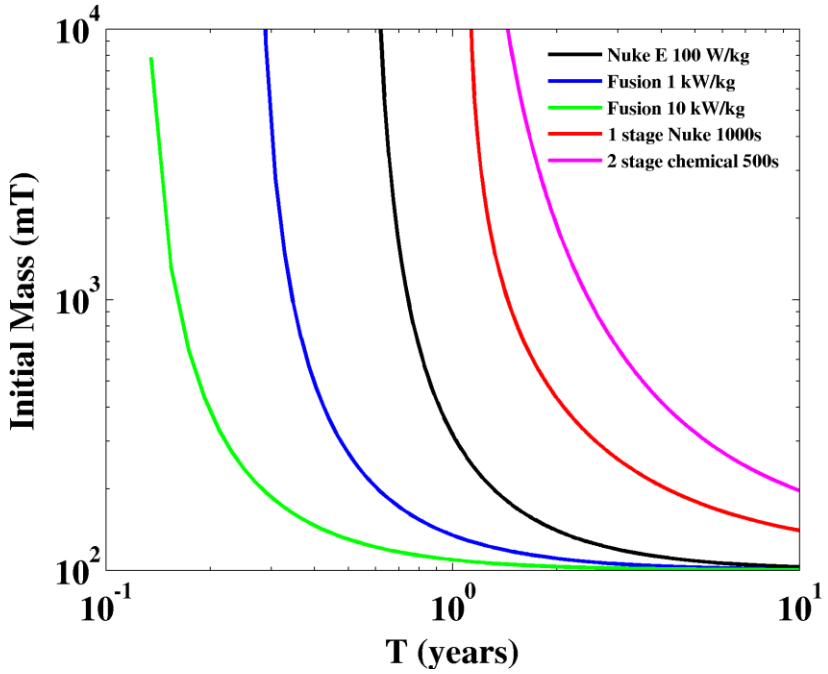

Figure 2.1. Comparison of initial spacecraft mass and transit times for roundtrip Mars mission [15].

The model used to obtain this figure was derived from work by Moeckel, which assumes gravity-free trajectories to examine the relationship between distance traveled and transit times based on propulsion system parameters [28, 29]. An attractive feature of Moeckel's approach is that it provides analytical models for propulsion systems that use continuous and impulsive burns. For impulsive burns, the burn time is small compared to the transit time while for continuous burns, the burn time is comparable to the transit time. Chemical and nuclear thermal propulsion are among the systems that use impulsive burns while nuclear electric and fusion propulsion systems use continuous burns.

Compared to other propulsion systems, fusion offers significant payload mass and short transit times. Fusion propulsion also been identified as an attractive candidate for making interstellar missions possible [30-32].

One of the earliest nuclear propulsion concepts explored by engineers was Project Orion, in which a spacecraft carries a large number of nuclear explosives. The explosives are ejected one at a time and detonated at a certain distance from the vehicle. Plasma from the explosion impinges upon a pusher plate at the spacecraft's rear and propels the vehicle forward [33-35]. A vehicle design concept of the Orion is shown in Figure 2.2

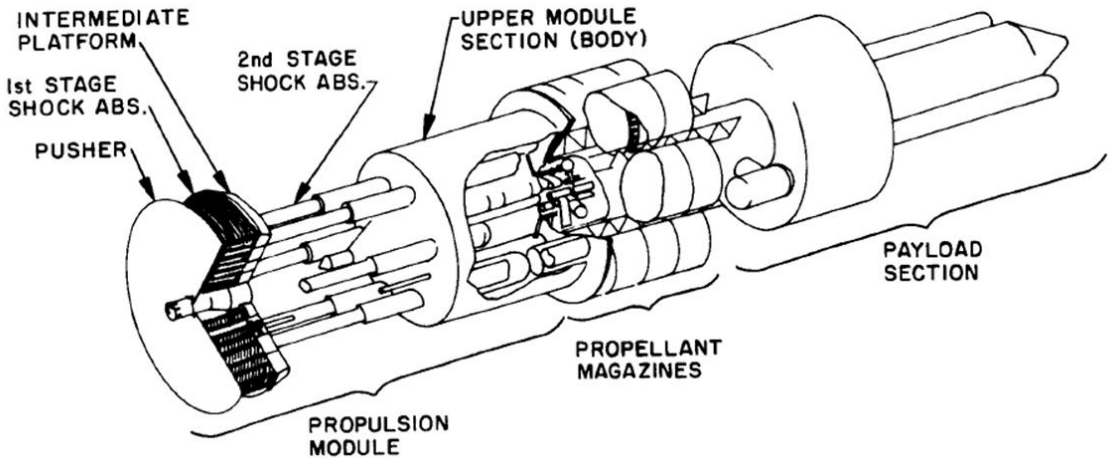

Figure 2.2. Orion vehicle concept [34].

Many pulsed nuclear propulsion concepts followed Project Orion, with several using pulsed lasers to induce fusion microexplosions in fuel pellets, which have been investigated by Los Alamos National Laboratory [36], Lawrence Livermore National

Laboratory [37, 38], Hyde [39]. Winterberg, the British Interplanetary Society, and the U.S. Naval Academy have also investigated electron beams for use in initializing fusion microexplosions to propel interplanetary and interstellar spacecraft [40-42].

Project Icarus is an engineering design study that seeks to build upon the work of Project Daedalus to design an unmanned interstellar probe capable of reaching the nearest stars using pulsed fusion propulsion. An illustration of the Icarus interstellar probe concept is shown in Figure 2.3

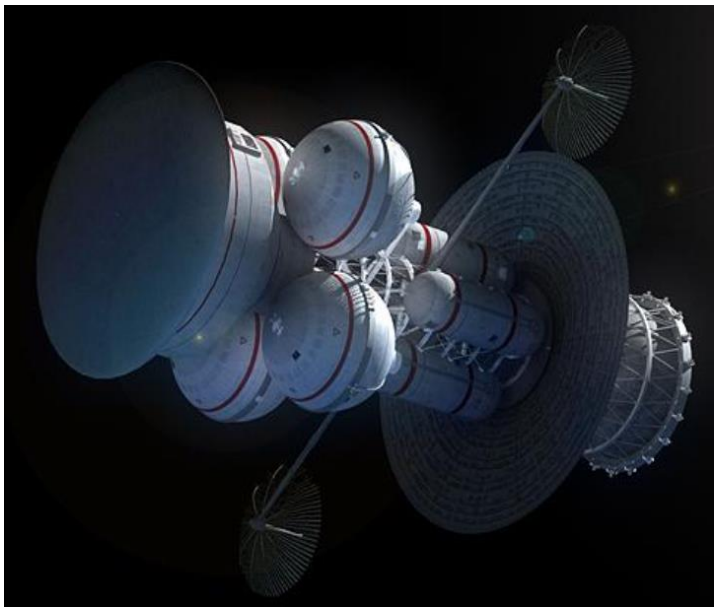

Figure 2.3. Icarus interstellar probe concept [43].

The FIREBALL (Fusion Ignition Rocket Engine with Ballistic Ablative Lithium Liner) concept explored at Marshall Space Flight Center consists of an Orion-like spacecraft that uses a pusher-plate, shock absorbers, and a magazine of pulse-units. For

propulsion, a lithium liner and a dense field reversed configuration (FRC) plasmoid of deuterium and tritium are ejected from the main spacecraft. The liner slows the FRC, compressing and heating it until fusion reactions occur [44]. This is illustrated in Figure 2.4

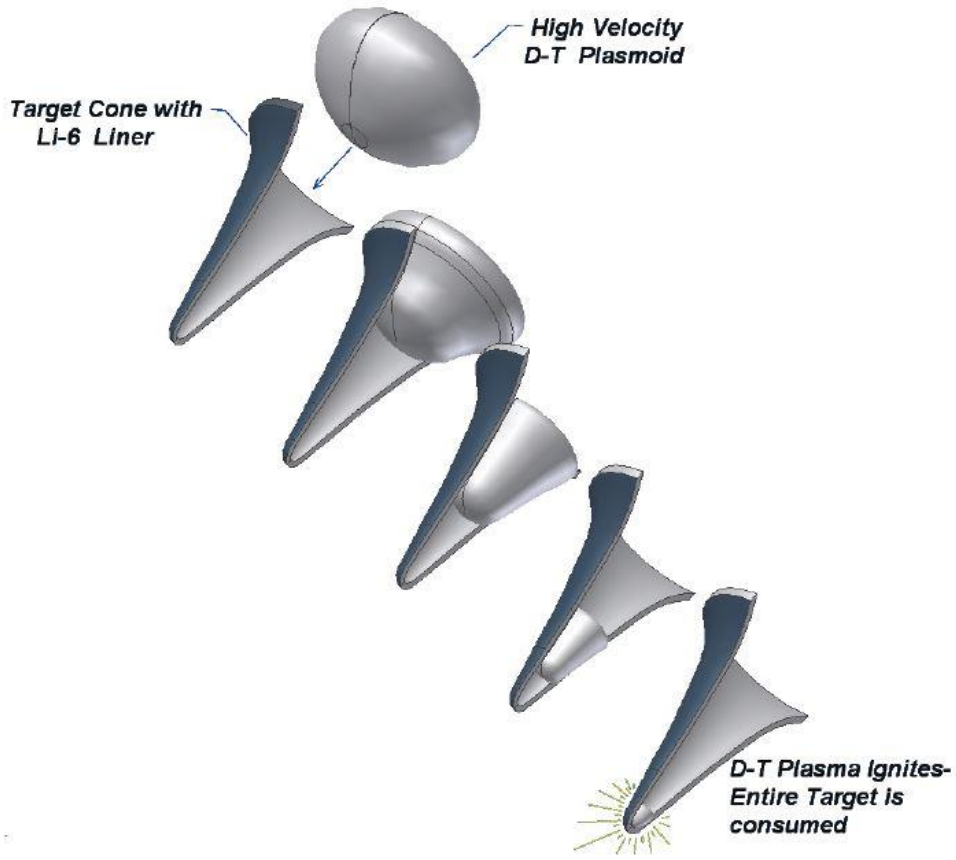

Figure 2.4. Collision of FRC plasmoid with lithium liner in FIREBALL concept [44].

Similar to the Orion, plasma resulting from the nuclear reactions upon a pusher plate and imparts propulsive momentum onto the vehicle.

2.3 Solid Liner

Many experiments have imploded solid liners onto plasmas. Among these are the Russian MAGO experiments. One of the systems investigated in the MAGO experiments consisted of a thermonuclear target displaced in the center of a compression vessel with one or several cylindrical or spherical liners to compress the target. The target was heated by accelerating a plasma with a magnetic field and then heating, followed by deceleration that results in a shock wave. Calculations suggest that an energy source with a range of 500 to 1,000 MJ with a characteristic operation time of 5-10 μs would be required in order to ignite the target [45]. The compressed plasma parameters needed to achieve ignition were determined to include a number density of ~20^{20} cm^{-3}, a characteristic size of 1-2 cm, a confinement time of ~1 μs, 10-20 MJ of total energy in the compressed plasma volume, and a temperature of 10-15 keV. Preheating the plasma would result in a decrease of requirements for the compression velocity of the liner [45].

Ryutov and Thio explored an MTF concept consisting of a spherical blanket of lithium hydride. The MTF system is installed inside the LiH sphere and then the entire assembly is placed inside a reaction chamber. Once the target reaches the center of the reaction chamber, plasma electrodes are used to connect the target with the terminals situated in the walls of the reaction chamber [46].

The field reversed configuration liner experiment (FRX-L) at LANL seeks to form and translate an FRC into a metallic liner and then compress the liner and plasma to fusion conditions. The experiment aims to form the FRC using the field-reversed theta pinch

method, with the plasma having a density on the order of 10^{17} cm^{-3} and a peak magnetic field of 5 T [47].

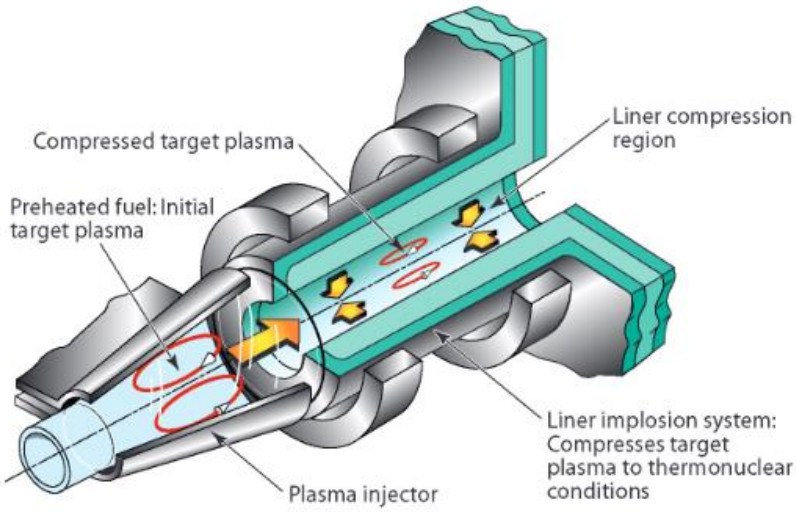

Figure 2.5. LANL FRX-L [48].

The design of the FRX-L was guided mainly be existing hardware at LANL and plans for future experiments that could be conducted with compressions of the metallic liner and FRC.

2.3.1 Z-Pinch

Z-pinch fusion is an MIF concept that consists of running current in the MA range through a plasma over microsecond timescales. The current generates a strong magnetic

field due to the Loretnz force, which compresses the plasma until fusion reactions occur [25, 49].

The MagLIF concept explored by Sandia National Laboratory uses a pulsed-power machine to implode a cylindrical liner onto a fusion fuel [50]. Slutz et al conducted one-dimensional simulations of MagLIF and found that magnetizing and preheating the fusion fuel is necessary for achieving significant fusion yield. Two-dimensional simulations found that a liner with a thickness 10-20% of the radius is needed to mitigate the magneto-Rayleigh-Taylor instabilities [51]. The 2D simulations also found that a hot spot with a sufficiently high areal density was needed for a burn wave to propagate radially through the fusion fuel. A liner aspect ratio of 6 was found to be effective in preventing Rayleigh-Taylor instabilities. The fusion gain was found to exceed 100 for a current of 60 MA and 1,000 for a current of 70 MA [21]. Experiments conducted by Gomez et al. involved a target of deuterium gas pre-magnetized with a 10 T field that was heated by a 2.5 kJ, 1 TW laser and imploded by a 19 MA current. The experiment resulted in deuterium-deuterium and secondary deuterium-tritium fusion reactions. These experiments verified the capability of MagLIF to achieve fusion conditions with laser heating and magnetization, as well as compressing a seed magnetic field [52].

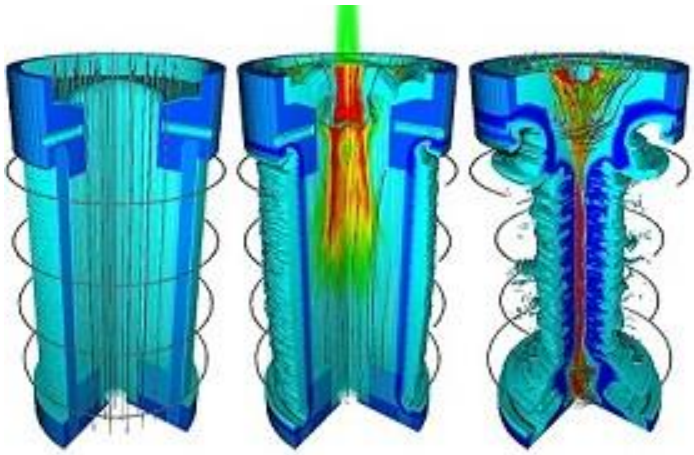

Figure 2.6. MagLIF concept [52].

Slutz et al. investigated magnetizing fusion fuel within a liner with external field coils and then using a pulsed laser to implode the fuel and the liner. The magnetic field strength increases as the fuel is compressed to inhibit energy losses that would otherwise result from electron thermal conduction and the escape of alpha particles. The liner is imploded on a timescale of ~100 ns. The short implosion time is needed due to the preheating of the fuel scaling unfavorably with longer implosion times. In addition, larger liners are more difficult to implode due to larger inductances and require more complicated magnetic field lines [51].

The Laboratory Directed Research and Development (LDRD) project at Los Alamos National Laboratory (LANL) performed experiments with the High Density Zeta Pinch (HDZP), Marx bank pulsed-power machine. In these experiments, a discharge through cryogenic deuterium fibers created a strong pinch and produced a neutron generating plasma. The goal of this project was to create a very fast Z-pinch that would be able to reach a stable condition inside the plasma before instabilities could develop. If this

state could be achieved, then it might also have allowed for fusion gain to be achieved. Unfortunately, it proved to be impossible to do this with the HDZP machine [25].

While the HDZP direct Z-pinch approach was unsuccessful, it demonstrated a technology that could create a very hot, magnetized plasma. Even though instabilities did develop in the plasma, they did not disturb the pinch, but rather allowed the magnetic field to diffuse into the plasma as it expanded. The wall limited the expansion of the plasma, causing it to evolve into a one-dimensional configuration and adjusted to what appeared to be a Kadomtsev stable profile. The combined average values for temperature, density, and magnetic field profiles exceed what was calculated to be the minimum that would be needed for an MTF target plasma [25].

The ZaP Flow Z-pinch experiments at the University of Washington produce hydrogen Z-pinch plasma columns 100 cm long and 1 cm in radius with flow velocities on the order of 100-200 km/s. The experiments explore the possibility of stabilizing plasma formed from a Z-pinch using sheared axial flows and have produced plasmas that are stable for much longer than classical instability times [53, 54].

The Pulsed Fission-Fusion (PUFF) is a spacecraft propulsion system concept being researched at Marshall Space Flight Center that utilizes a Z-pinch to compress a cylindrical target of lithium deuteride that is surrounded by a layer of fissionable material such as uranium, which is in turn surrounded by another layer of lithium deuteride. This is illustrated in Figure 2.7

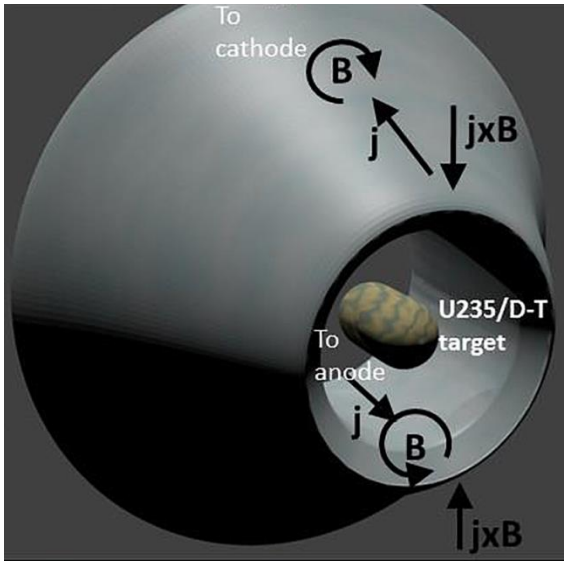

Figure 2.7. PUFF target compression [55].

As the target compresses, uranium atoms begin to fission. These neutrons turn some of the lithium-6 atoms to tritium. As the target continues to compress, deuterium and tritium atoms begin to fuse together, increasing the temperature and pressure while generating more neutrons, which initiate more fission reactions. This sustains the energy release and further compresses the fusion fuel. This fortuitous cycle continues until a detonation wave propagates through the target, and allows for a more complete burnup of both the fissionable and fusion materials. The high power pulses will be delivered with linear transform drivers, inductive transformers with a primary inductor consisting of a fast-switch, low inductance cavities to induce a current. A stack of cavities can produce extremely high voltages with pulse widths of less than 100 ns [55].

An illustration of a PUFF spacecraft propulsion system is shown in Figure 2.8 with a vehicle configuration shown in Figure 2.9

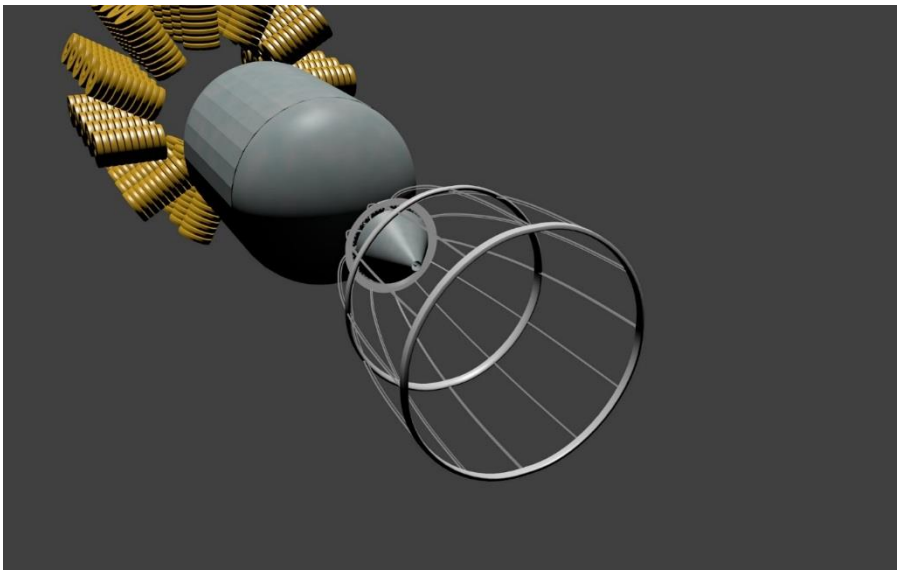

Figure 2.8. PUFF system [56].

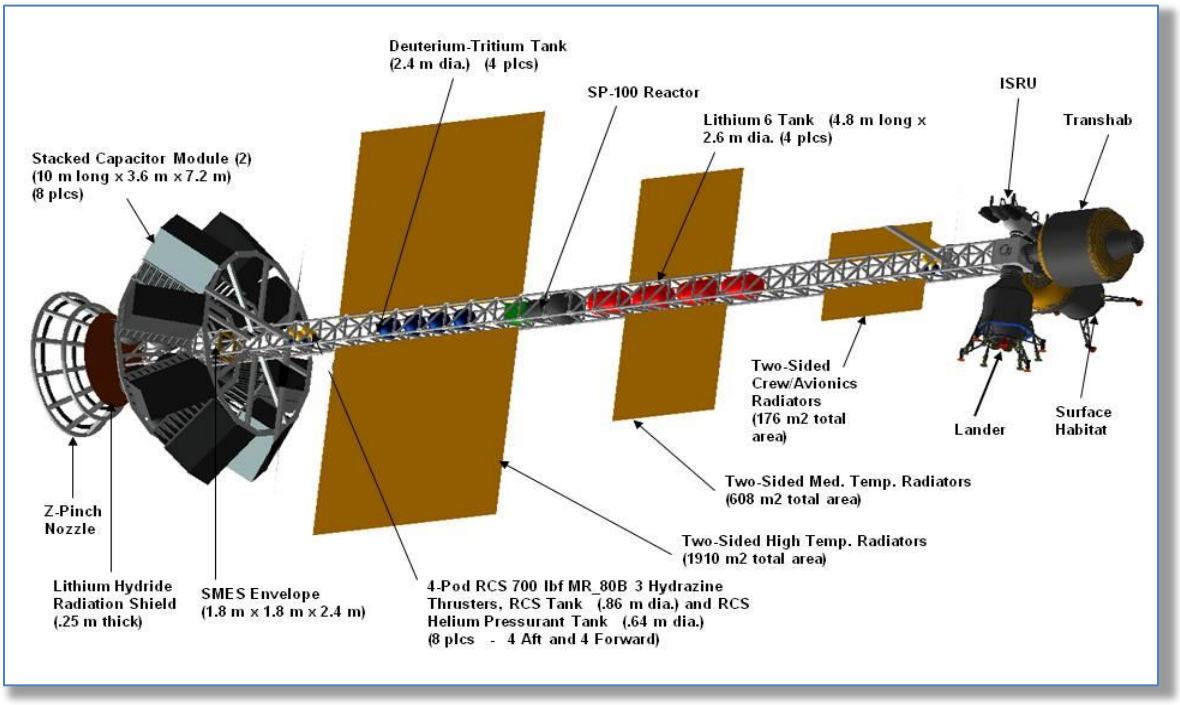

Figure 2.9. Z-pinch vehicle configuration [57].

One of the most crucial pieces of hardware for the PUFF project is the Charger-1, which is shown in Figure 2.10

Figure 2.10. Charger-1 pulsed power machine [58].

The Charger-1 is a 550 kJ, 3 TW pulsed power machine located at the Aerophysics Research Center on Redstone Arsenal. Once operational, the Charger-1 will discharge a powerful electrical current to compress PUFF targets in a Z-pinch [58].

Miernik et al. investigated another Z-pinch fusion propulsion system. In this concept, a Z-pinch is formed using an annular nozzle. Deuterium-tritium is injected through the inner nozzle and lithium-six is injected through the outer nozzle. The lithium-six is focused in a conical manner so that it will mix with the D-T at a point, with this point

acting as a cathode. The lithium-six acts as the current return path while also reacting with neutrons generated by D-T fusion reactions. This results in more tritium being produced, thus creating high-energy products that boost the engine's energy output, allowing for very high exhaust velocities [26].

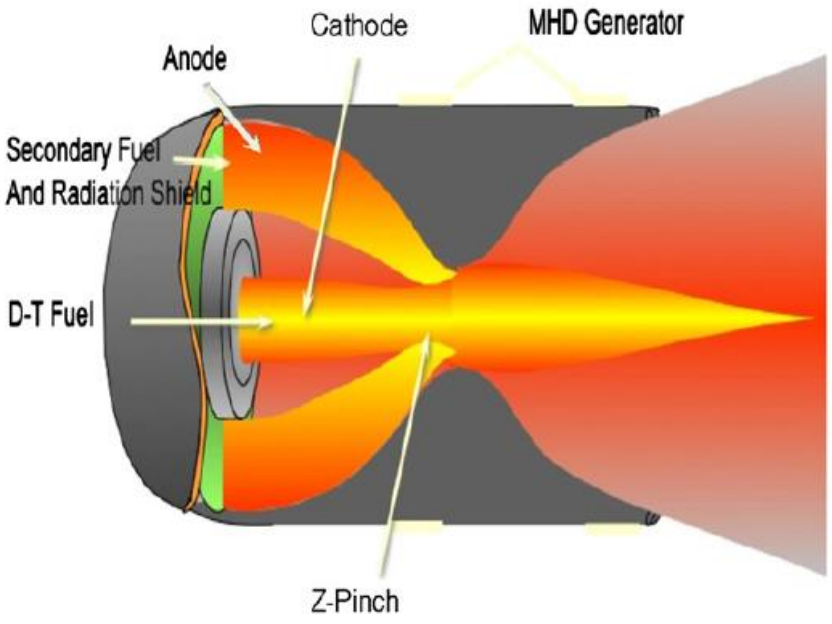

Figure 2.11. Z-pinch fusion propulsion concept [26].

A magnetic nozzle is needed to convert the resulting fusion energy into a propulsive impulse. This magnetic nozzle consists of current-carrying rings arranged in a parabola focused on the location where fusion reactions occur. Once the Z-pinch initiates fusion reactions, the resulting hot plasma expands rapidly and compresses the magnetic flux. As this occurs, the magnetic field strength and magnetic pressure increase until the magnetic

pressure is equivalent to the dynamic pressure of the plasma. The magnetic field lines then rebound to their original configuration, ejecting the plasma and imparting propulsive momentum onto the space vehicle [26]. An illustration of this process is shown in Figure 2.12

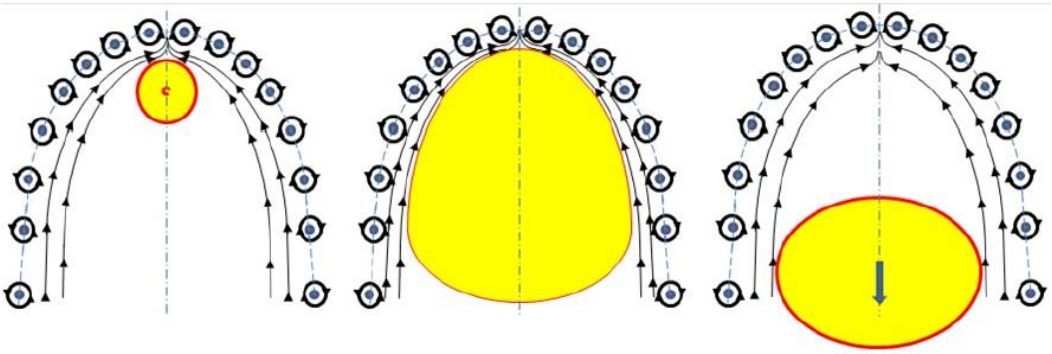

Figure 2.12. Pulsed magnetic nozzle [15].

Currents are also induced in the coils during the plasma's expansion phase. This electrical power can then be used to recharge the system and repeat the cycle [59]. Pulsed magnetic nozzles have been investigated in several fusion propulsion concepts [60-64].

2.3.2 Inverse Z-Pinch

In an inverse Z-pinch, a cylindrical conductor is surrounded by a liner, with the space between the conductor and liner filled with fusion fuel plasma that contains magnetic flux trapped in place by an azimuthal magnetic field. The magnetic flux is generated by an

electrical current that moves in the axial direction through the conductor [65]. Another current is then driven through the liner by a pulsed power device. An electric connection outside of the liner is needed in order to provide a return path for the current [66]. This is illustrated in the following figure

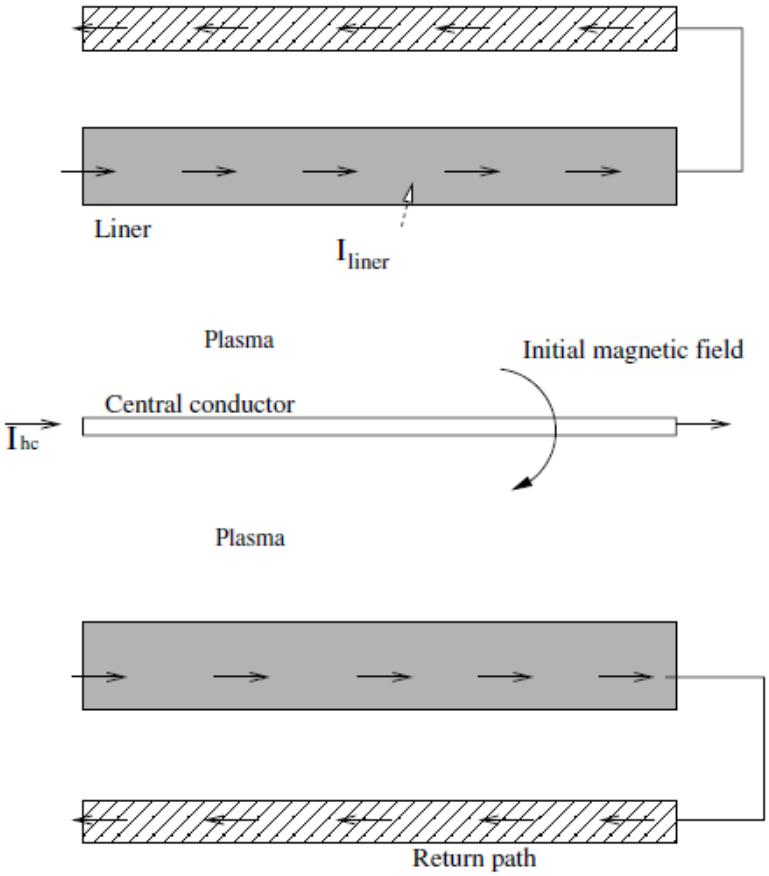

Figure 2.13. Inverse Z-pinch [66].

Joule and compressional heating have a major effect on the outer surface of a liner in a Z-pinch. For an inverse Z-pinch, the inner and outer surfaces of the liners will be affected by compressional heating. This would also cause spatial profiles of the material strength of a solid liner, which in turn would affect the critical wavelength and amplitude of the liner.

2.4 Liquid Liner

General Fusion is investigating an acoustically driven MTF system that uses a sphere filled with molten lead-lithium pumped to form a vortex. Magnetically-confined plasma is injected into the vortex. An array of pistons is used to compress the liquid metal and drive a pressure wave into the plasma and bring it to fusion conditions [67-69].

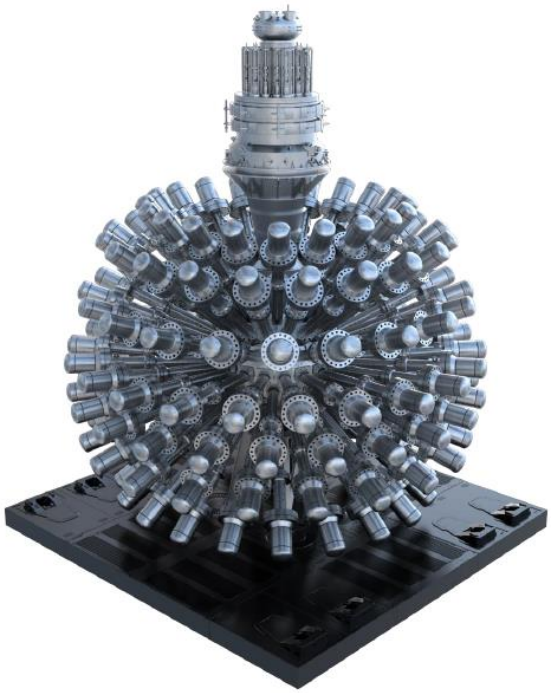

Figure 2.14. General Fusion's acoustically driven MTF concept [70].

The liquid metal absorbs energy from the fusion reactions that can then be used to drive turbines and generate electricity. The liquid metal also protects the outer wall of the reactor from damage by the fusion plasma and breeds tritium from the lithium.

The stabilized liner compressor (SLC) is another fusion reactor concept uses pistons to compress a liquid metal liner concept, although only two pistons are used in this design. The pistons implode the liquid metal liner onto a magnetized target plasma, with adiabatic compression initiating fusion reactions in the target [71].

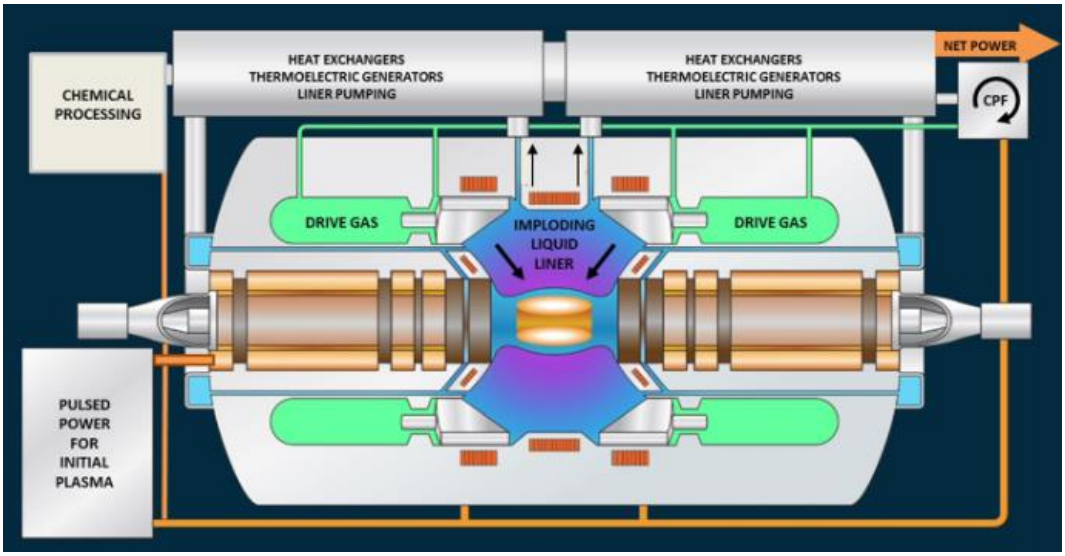

Figure 2.15. SLC fusion reactor concept [71].

Like the General Fusion reactor concept, the liquid metal provides shielding from the high-energy fusion neutrons and allows for the breeding of tritium.

2.5 Macron Liner

Kirtley and Slough investigated a concept that uses a macroparticle (macron) formed liner to compress an FRC plasma [72]. In this concept, two FRCs are injected into the reactor chamber and merge at the center to form a single FRC that acts as the fusion target. The decay time of this larger FRC must be long compared to the time needed to assemble and compress the FRC. The liner formation time must in turn be longer than the FRC decay time.

A cluster of metallic masses are also injected into the reactor, which form a metallic liner. This allows the compression energy for the FRC to be delivered on a smaller timescale than what is required to actually compress the FRC.

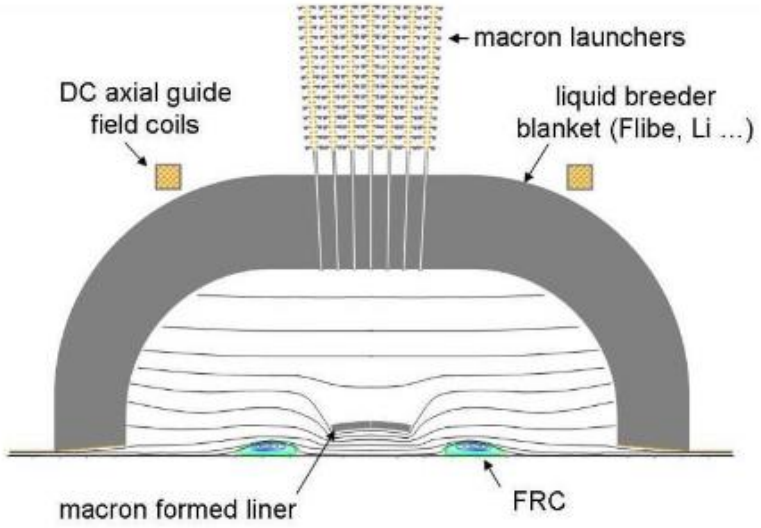

Figure 2.16. Macron former liner reactor concept [72].

The size, mass, and number of macrons selected are based on the need to form a liner that will be able to compress the FRC sufficiently enough to reach fusion conditions. Kirtley and Slough expected for the macrons to have a mass of four grams and accelerated to 3 km/s by the launchers. This would give the macrons a kinetic energy on the order of 20 kJ. If the macrons have a radius of one centimeter, they will begin to merge at a radius of 10 centimeters.

The macron liner has several advantages over solid liners. Compression efficiency is enhanced by the axial compression of the FRC. The concept does not require electrical contacts, which simplifies the overall system. A specified rotation rate can also be imparted on the macrons. This rotation can help to prevent instabilities from emerging during compression.

The accuracy and timing of the macron injection must be capable of achieving the desired behavior in the liner. Electromagnetic and gas dynamic schemes can be implemented to accelerate the macrons to their required velocities. The axial gradient in the force that is imparted on the macrons by the propagating field allows for self-correction of the macrons' response to different sizes and masses.

2.6 Plasma Jet-Driven Magneto-Inertial Fusion

A major disadvantage of solid liners is that they are not reusable, with a new liner having to be manufactured and then injected into the reaction chamber for each shot that is made. Debris may also be deposited on the interior wall of the reaction chamber when solid liners are used, damaging the system. In order for the fusion system to be reusable, the

reactor chamber wall and the hardware used to inject the liner into the reactor chamber must be located far enough away from the fusion target in order for the system to be reusable.

To address these issues, Thio developed the concept of plasma jet magneto-inertial fusion (PJMIF) [73], which is the focus of the next chapter.

CHAPTER 3

PJMIF STUDIES

3.1 Introduction

In the PJMIF concept, a series of plasma jets is used to form a cylindrical or spherical liner, which then implodes on a magnetized fusion fuel target and brings it to fusion conditions [74]. This is illustrated in Figure 3.1

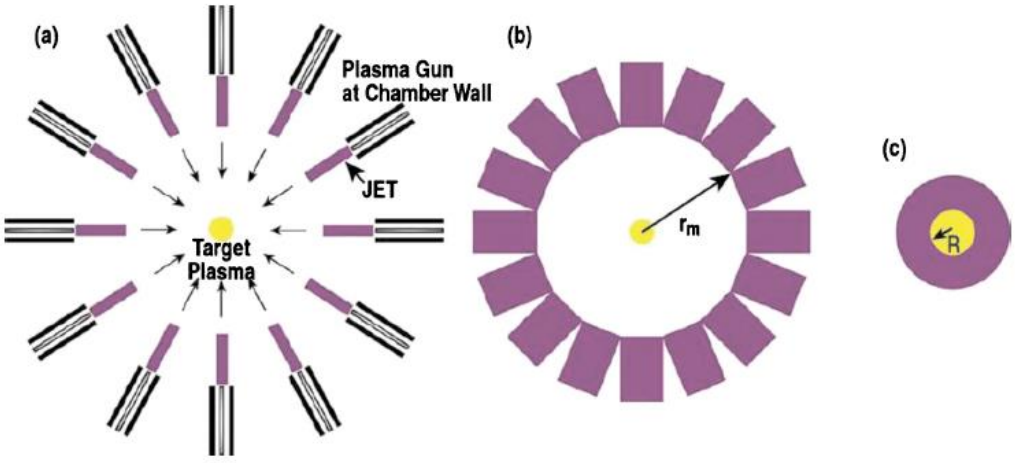

Figure 3.1. Plasma jet induced magneto inertial fusion concept [75].

Once the plasma liner has been formed and reaches the boundary of the target, the target and shock boundaries go through five stages. In the first stage, the plasma liner forms and begins to implode to the target. Then a radially inward shock is launched at the interface of the target and liner. In order for this to be done, the liner velocity exceeds the local target sound speed. A layer of shocked target material forms behind the shock and begins to move inward. The liner compression continues and is a primarily isentropic process.

The shock then reaches the origin, at which point the target has been entirely heated by the compressing shock. Immediately after shock collapse, a reflected shock begins to propagate radially outward. The material in the target that is behind the reflected shock will reach its peak temperature and pressure during this process. Once the reflected shock reaches the boundary of the target and liner, it will either continue propagating outward or be reflected inward. The reflected shocks become progressively weaker until the pressure of the inner target is equivalent to the dynamic pressure of the liner, at which point a stagnation shock will begin to propagate outward through the liner. The existence and number of secondary converging or reflected shocks that may occur at this point will depend on the strength of the mismatch between the dynamic pressure of the liner and the static pressure of the target.

After this point, the liner has completely stagnated. A rarefaction wave will then travel radially inward, disassembling the stagnated system of the liner and target, with the target no longer being confined once the wave reaches the origin. The dwell time can be approximated as the time it takes for the outgoing shock to propagate through the target

and liner plus the time of the rarefaction wave [24]. These stages are illustrated in Figure 3.2

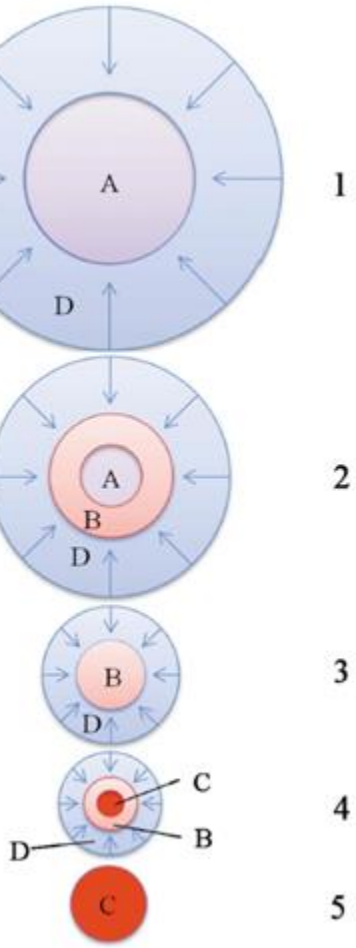

Figure 3.2. Stages of target and liner compression [24].

During confinement, there are four characteristic velocities of interest. These are the expansion speed of the target, the rate of propagation of the outgoing shock wave through the liner, the incoming liner velocity, and the rarefaction velocity.

Because the expansion speed of the target is relatively small, the compressed target does not expand significantly until after the rarefaction wave reaches the target. The dwell time can then be approximated as the duration from peak compression to the outgoing shock reaching the outer liner boundary plus the rarefaction time. Dwell times are expected to approach 1 μs [24].

The PJMIF concept does not have many of the problems associated with solid liners. The driver hardware can be far away from the fusion target so that it is not damaged or destroyed with each shot. This would avoid the high cost associated with destroying the materials in solid liners and transmission lines. The standoff driver of a plasma driver would also have higher repetition rates than the driver for a solid liner. The standoff distance and reusability offered by plasma liners may be opening a path that could lead to a viable reactor concept.

3.2 PJMIF Propulsion Systems

Several studies have researched using PJMIF as a spacecraft propulsion system [76]. Among these is the HOPE study, which was a conceptual design for a crewed vehicle to the outer solar system investigated by Adams et al [27, 77]. An illustration of the HOPE vehicle concept is shown in Figure 3.3.

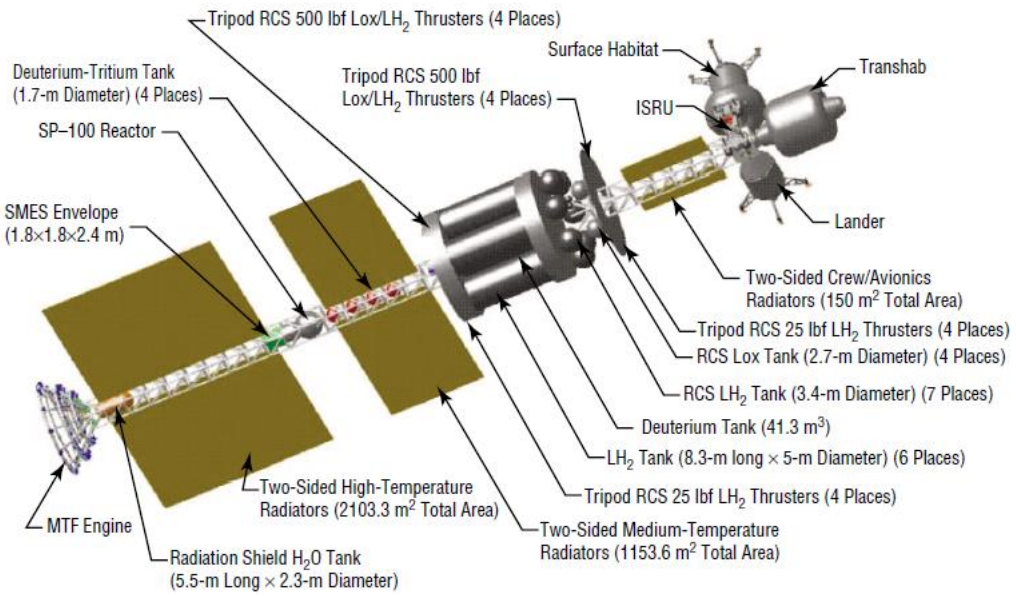

Figure 3.3. HOPE conceptual vehicle design [27].

The propulsion system for the HOPE vehicle has the target plasma located at the focus of the magnetic nozzle. A pair of conical theta pinches are positioned at diametrically opposite locations on each side of the nozzle's focus. These theta pinches launch a pair of spheromak plasmoids at the focus of the nozzle. The toroidal magnetic fields of the spheromak plasmoids are oriented in opposite directions, which allows for the two spheromaks to merge with each other upon collision, forming a field reverse configuration (FRC) plasmoid. Once the FRC plasmoid has been formed, the plasma guns are fired, and the liner compresses the plasmoid.

The plasma gun used in this system consists of two concentric electrodes connected to a capacitor. Plasma enters through the gap between the electrodes, after which a switch is closed, which allows for the formation of a high potential gradient between the inner and outer electrodes. This causes the gas to ionize, completing the circuit and discharging the

capacitor. The plasma gun has a converging two-barrel arrangement with internal contouring so that the plasma jet can be focused. A PJMIF propulsion system has also been investigated for use on an interstellar probe as part of Project Icarus for unmanned interstellar missions [30].

3.3 PJMIF Modeling Studies

Simulations of the PJMIF concept have been conducted since the 1990s, with different studies focusing on different physics regimes pertinent to this fusion concept [74]. One of the early modeling studies focused on the drivers for the plasma jets, with one option being coaxial plasma guns. These devices consist of a pair of coaxial cylindrical electrodes, with an electrical current passing through a plasma that is located between the gaps in the electrodes. The current flow generates a magnetic field, which produces a Lorentz force that accelerates the plasma to a high velocity. Two-dimensional magnetohydrodynamics simulations of coaxial plasma guns have been conducted to advance the technology needed for plasma liner experiments. The merging and implosion of twelve plasma jets of deuterium have been simulated using the MACH2 code by Cassibry. In Cassibry's study, each jet has an initial radially inward velocity of 200 km/s and a mass of 500 μg. The simulations assumed that the flow was inviscid, with artificial viscosity used to dissipate pressure oscillations behind the shock waves formed by the liner implosion. The liner was found to form at 350 ns, with the leading edge having a hypocycloid shape. When a magnetized fusion fuel target was included in the simulations, the magnetic field gradient drove a current along the surface of the target. Ohmic heating

further raised the temperature at the surface of the target. A rarefaction wave then propagates through the target. When the plasma liner begins to compress the target, the magnetic flux is compressed. This causes magnetic field gradients in the center of the target, which induces further currents and provides additional heating [77].

Knapp and Kirkpatrick investigated the effect that the plasma liner implosion velocity has on the fusion energy gain of PJMIF. Their test cases consisted of one-dimensional implosions of several shells of xenon plasma, with each of these shells having a different density but the same inward velocity. The liner implodes on a shell of deuterium and tritium, and within this shell is a spherical target of deuterium-tritium. The inner D-T target is warmer and less dense than the outer shell of D-T. It was found that reducing the number of layers of xenon gas in the liner reduced the amount of input energy more than it reduced the fusion energy yield. Different cases were run that had no electron heat conduction, full electron heat conduction, and electron heat conduction that was suppressed by a B-theta field [78]. Front tracking features were used to prevent diffusion across material interfaces. The gain was found to increase as the implosion velocity increased up until about 100 km/s. The reason for this is because the initial kinetic energy increases with the implosion velocity, but the fusion energy yield is eventually unable to keep up. Gains greater than 30 were also attained in the simulations. This is the gain range in which PJMIF becomes a viable energy concept. When full electron heat conduction was included in the simulations, higher gains were achieved. Gains were about the same for cases that had no electron heat conduction and full electron heat conduction that was suppressed by a B-theta magnetic field. For a liner of xenon plasma that has an implosion velocity greater than 60

km/s, a magnetic field reduces energy loss by electron thermal heat conduction sufficiently enough for fusion ignition to occur [78].

Cassibry et al. investigated a scaling relationship of the peak pressure for an imploding plasma liner as a function of the plasma jet velocity, number of plasma jets, mass of the plasma, jet Mach number, radius of the reaction chamber, initial jet diameter, initial jet length, initial arrangement of the jets, the weight of the jet species, and the specific heat ratio [79]. Identifying this scaling relation aids in determining what the peak stagnation conditions will be for the liner. Deviations from this scaling relation allow for the determination of what variables most directly affect the peak pressure of the imploding liner. Simulations for this study were conducted using SPHC, a three-dimensional Lagrangian code that used an ideal gas equation of state and ignores effects from radiation and thermal conduction losses. Some simulations included adiabatic gas targets. Other cases included random perturbations for the jets' initial radial positions in order to mimic jittering that would result from plasma guns being fired in a real experiment. The jet Mach number had values that ranged between 1 and 100. The initial jet velocity ranged from 50 km/s to 200 km/s, while the initial jet temperature ranged from 0.032 eV to 796 eV. The simulations used 12, 18, 34, 30, 36, and 60 plasma jets. The number density of jets ranged from $9.13\times10^{21}/m^3$ to $8\times10^{24}/m^3$. The ratio of specific heats ranged from 1.1 to 1.67. The peak pressure was approximated as the ram pressure of the imploding plasma liner. The greatest value for the peak pressure occurs at the origin right when the liner implodes on the void. An average value for the pressure was obtained at a fixed radius over a solid angle in order to generate radial profiles at different times in the simulation. When the jets merge, the radial pressure profile has a sharp leading edge that peaks and decreases. The void was

found to fully collapse at about 17.5 μs. The profile of the pressure was found to be flat at around 17.9 μs, which was followed by an increase in the pressure at the center and a peak value occurring at 19.2 μs. The center of the hot spot had a single symmetric peak and a region surrounding this peak that has a lower pressure and sharp gradients. After maximum pressure occurred, a smoother pressure profile formed. The study found a dimensionless scaling relation for pressure, which showed that for a given Mach number, the peak pressure increases linearly with the density and the number of jets, increases quadratically with the radius and initial velocity of the jets, and has an inverse relationship with the square of the wall radius. With a larger chamber wall radius, the jets have a larger merging radius, which in turn requires a greater amount of compression. This in turn necessitates a higher temperature and a lower Mach number for the liner. Having fewer jets caused the jets to have a wider angular separation. This causes stronger shocks to develop when the jets merge, which in turn causes the temperature of the liner to increase and the Mach number to decrease. Some cases were observed to deviate from this scaling relation due to an increase in the initial Mach number of the jets. Larger deviations were observed when perturbations were included in the timing of the jets [80].

Santarius used the BUCKY code to simulate fusion burns with different geometric configurations [81]. The BUCKY code is a one-dimensional Lagrangian hydrodynamics code that solves the fluid equations by incorporating the effect on pressure caused by electrons, fast particles, ions, and radiation. The simulations were assumed to have an initial magnetic field strength of 1 T. The fusion reaction rates for the fuel and the peak pressure were found to occur at about the same time and peaked in value for tenths of a microsecond. The code predicted a peak interface ram pressure of about 14 Mbar. The

same simulation was then performed with a two-temperature model, which showed greater compression and dwell time. Differences between the single and two-temperature physics models indicate that simulations are very sensitive to the timing of the plasma jets and the parameters defining the thermodynamic state and motion. The code incorporates Braginskii perpendicular thermal conductivities that are enhanced by magnetic fields for both the ions and the electrons. The burn time was enhanced by extending the compression phase through the utilization of the liner inertia. One case investigated a liner with an initial thickness of 15 centimeters and examined the convergence and expansion for both the plasma liner and the target in both the initial zones occupied by the target and the plasma jets as well as the edge of the plasma [81]. The results showed a large radial compression of the target. The plasma reached a peak temperature within the center of the target and climbed to a value of about 8.8 keV, while the average temperature of the target was on the order of 2.3 keV. The simulation found the target remained compressed for about 2 μs and then expanded to twice of this compressed radius after an additional 2.15 μs. The code also found a minimum radius about 0.62 centimeters and a peak interface ram pressure of about 14 Mbar. Another simulation was done that examined a liner that was five centimeters in thickness. The results of this simulation indicated that it only took 0.7 μs for the minimum radius to double in value and 0.15 μs for the maximum pressure to decrease by half. However, the thinner liner was also found to produce a higher fusion yield [81].

Kim et al. studied cases for PLX using the FronTier code, a Lagrangian-Eulerian code that tracks Lagrangian meshes that move through an Eulerian grid [82]. The code is able to resolve and obtain time evolutions of material topological changes in two and three dimensions. A drawback with using the FronTier code is that the front tracking method has

lower accuracy than untracked methods when resolving discontinuities across material interfaces. Simulations conducted in this study ignored radiation transport and heat conduction in order to show the impact that atomic processes had on the behavior of the plasma liner. Simulations that used argon and deuterium for the liner material incorporated atomic physics. Before the liner interacts with the target, the ionization energy is very small. When the target was compressed by the liner, the front edge of the liner was ionized significantly enough to overcome the effects of dissociation. The liner had an initial temperature of 2.8 eV and an initial average ionization level of 2.25. During the liner implosion, the ionization level increased slowly, reaching a level of 7.2 in the center of the reactor chamber. Within the chamber, the density was observed to increase by a factor of 6.5, the stagnation pressure doubled, and the temperature was reduced by a factor of 2.3. The Mach number was also 1.5 times larger when the polytropic model was used compared to simulations that used the plasma EOS model. Nearly 95% of nuclear fusion reactions that occurred within the target were completed between the time when maximum compression occurred and when the pressure decreased by a factor of two. The stagnation time was found to increase as the thickness of the liner increased, which provides a characteristic time for the high energy density region around the collapsed liner. The mass, thickness, temperature, and velocity of the liner were kept constant in order to investigate the effect that a realistic longitudinal density profile would have on the final pressure of the liner [82]. Another case investigated by Kim et al. involved an imploding deuterium liner that had a total amount of 164 MJ in stored energy [82]. The mean dissociation fraction in the liner reached a value of 0.02 during the end of the implosion process, and the ionization fraction was negligible at this point. The temperature of the liner was found

to be three times smaller than the value that was obtained for a simulation that used the polytropic equation of state for the same problem. The Mach number was also found to be larger by a factor of two. This contributed to the target being compressed more. The fusion energy gain was also found to be 1.5 times greater when the atomic processes were included in the simulation [82].

Kim et al. investigated three-dimensional simulations of a plasma liner formed from 30 argon jets. The results were compared to a one-dimensional simulation that had the same liner mass, pressure, and density. The reduction in the Mach number was found to occur faster for the three-dimensional simulation than the one-dimensional simulation. The implosion pressure for the three-dimensional liner reached a value of 6.4 kbar, which was ten times smaller than what was obtained for the one-dimensional simulation. This is due to the energy sinks that result from ionization occurring and the mitigation of residual vacuum gas compression caused by the application of the plasma equation of state in the vacuum region. In post-shock regions, pressure and density for three jet interactions are about ten times greater than what is seen in jet main bodies. The results for the shocks formed by the jet merging were in good agreement with theoretical results for oblique shock formation. The merging of jets is affected by secondary shock formation, the spreading of jets in transverse and longitudinal directions, an increase in the ionization fraction, and adiabatic compression heating. Large variations were observed in the density and pressure of the liner along surfaces where the liner edge would likely interact with the fusion target [83].

Samulyak et al studied a concept involving a 15 cm thick liner of deuterium that implodes and compresses a target of plasma [75]. The liner has an initial radius of 60 cm,

an initial density of 3.8×10^{-5} g/cm^3, a temperature of 415.4 K, a pressure of 0.65 bar, a velocity of 100 km/s, a Mach number of 60, and total stored energy of 164 MJ. The plasma target has an initial radius of 5 cm, an initial density of 8.3×10^{-6} g/cm^3, a temperature of 100 eV, and a pressure of 640.3 bar. A magnetic field was included in the simulation, which acts to suppress the electron and ion heat conduction during the compression of the target. During implosion, the density of the liner increases proportionally to r^{-2} [75]. When the liner impacts the target, it is compressed until it reaches stagnation at 6 μs. The compressed target had a radius of 0.73 cm, giving it a compression ratio of 6.8. This was much greater than the compressed radius of 0.5 cm that was predicted in the theoretical model. This can be attributed to the pressure increasing proportionally to the fifth power of the compression ratio while the target is being compressed. This resulted in the target having a lower stagnation pressure than what the theoretical model predicted. When the target begins to expand, it has an initial expansion velocity of about 0.58 cm/μs [75]. The theoretical value of the deconfinement time was calculated to be 100 ns, whereas the code used in this paper found the deconfinement time to be about 220 ns. The fusion fuel burnup fraction was found to be 6.67×10^{-4}. This is much lower than the theoretical prediction of 0.011. The fusion gain was calculated to be 0.012, which was 10.8 times lower than the predicted value. This difference can be attributed to the liner failing to compress the target to the radius of 0.5 cm that was predicted in the theoretical model [75].

Awe et al. investigated using a one-dimensional radiation hydrodynamic simulation to study the scaling of the stagnation pressure after a plasma has undergone a shock and the useful lifetime of a plasma liner [84]. This model assumes that a spherically symmetric imploding liner exists at the merging radius, ignoring the merging of the plasma jets and

compression of the fusion target. The initial conditions of the simulation consist of a spherical liner plasma that initially has a uniform density, temperature, and implodes toward the origin with a uniform velocity. The edge of the liner is initially sharp due to the transition across a single cell from the plasma to a vacuum. The collision frequency is greater than the electron and ion gyro-frequency for dense and cool plasma jets that have an initial embedded magnetic field that is less than 1 kG. Because of this low magnetic field, the study ignored magnetohydrodynamics effects. Simulations consisted of plasmas that have an initial temperature of 2.8 eV, initial velocities of 50 km/s and 100 km/s, and merging radii of 32.9 cm and 24.1 cm. The simulation codes use RAVEN and HELIOS with SESAME and PROPACEOS table lookups. Increasing the resolution of the grid increased the expansion at the leading edge of the liner, as well as the time averaged stagnated pressure of the plasma close to the origin. Simulations were conducted with and without radiation and thermal conduction. When there was no energy transport, the leading edge of the liner had a large effect on the stagnation pressure. Stagnation pressure was found to increase as a function of both the initial velocity and the initial density for high Mach number plasma liners. Increasing the thickness of the plasma liner was found to increase the stagnation time, reduce the stagnation pressure, and leave the maximum pressure almost unaffected. A correlation between the initial Mach number and the stagnation pressure was also observed [84].

Davis et al. added a more detailed ESO model to the Awe study and investigated the effect of ionization on liner implosion by reducing compression [85]. Argon jets were used for all of the simulations, with the jets having a merging radius of 24.1 centimeters and form a liner that is spherically symmetric with a uniform mass density, a temperature

of 1 eV, and a uniform implosion velocity. This study used HELIOS-CR, a one-dimensional Lagrangian radiation-hydrodynamic code that used LTE and non-LTE equation of state tables that are obtained from PROPACEOS. Energy and pressure were obtained using an isolated atom model that utilized Boltzmann statistics and either the Saha equation or a collisional radiative model to determine the number of atoms that should be present. Photoionization and photoexcitation effects were ignored for the collisional-radiative model when the temperature and density were calculated. A radiation transport model was used to calculate different radiation frequency groups. The pressure was found to increase as the initial implosion velocity increases. A shock was also found to propagate outward for the simulations. Simulations that used LTE and non-LTE yielded results that were nearly indistinguishable from each other over the range of pressure, temperature, density, and time that were investigated. A comparison was also made between simulations that used tabular and polytropic equations of state. When the polytropic equation of state was used, radiative losses were responsible for differences between the initial kinetic energy and the thermal energy of the liner after stagnation. When the tabular equation of state was used, about half of the liner's initial kinetic energy went into ionization of the liner gas. The mean charge reached a maximum value of approximately seven, causing a dramatic reduction in the compression and stagnation pressure of the liner. Different liner species were simulated that had the same initial density and implosion velocity. The pressure was found to increase with atomic number. The thermal and ionization energies were dependent on the type and quantity of heavy element species that were present. There was a larger amount of lighter elements than heavier elements, causing the peak mean charge of the heavy elements to vary between five and ten. The heavier species can be used

to fully strip ions from the liner and eliminate further losses that may result from ionization effects [85].

Cassibry et al. performed three-dimensional simulations of plasma jets using the smooth particle hydrodynamic code (SPHC) [86]. The objective of this study was to investigate the process of plasma liner formation, vacuum implosion, and expansion. The simulations consisted of thirty plasma jets that had parameters anticipated to be used in PLX. These include a total mass of 300 mg, a kinetic energy of 376 kJ, and an initial Mach number of 25. Simulations were run for a case that had a uniform liner and another case that had thirty discrete jets, with the different cases having the same total mass and thermal energy. For the discrete jet case, pressure spikes occurred between jet pairs at the beginning of the liner formation as a result of oblique shock formation. The uniform liner was observed to be thicker than the liner formed by the discrete jets due to the thermal energy expansion only occurring in the radial direction for the uniform liner. The pressure gradient was observed to become less steep for after peak pressure occurred, and then rising sharply toward the stagnated region of the plasma. The uniform liner was found to expand more rapidly than the thirty-jet case after stagnation occurred. Compressional heating was ubiquitous for the uniform liner during the beginning of the implosion process. For the thirty discrete jets, the compressional heating occurred primarily between the leading edge of the jets and the merging radius. This results in the uniform liner having both a higher mean temperature at stagnation and faster rarefaction waves. The regions where jet merging occurred and the origin at liner collapse were found to be prone to the development of Rayleigh-Taylor instabilities. These simulations did not account for ionization, thermal conduction, radiative transfer, or magnetic fields [86].

Parks examined a spherically symmetric, one-dimensional model of an imploding liner of deuterium-tritium plasma. Heating of the liner was done by deposition of energy from alpha particles that escape from the hot spot of the compressed target. Adiabatic compressional heating causes the Mach number to decrease in converging supersonic flows, with a lower Mach number also causing expansion in the jets. Radiative cooling in the liner can help prevent jet Mach numbers from decreasing too much. The model assumed that the plasma jets would only expand in the transverse direction. Jet collisions cause oblique shocks to occur, with the resulting heat causing a loss in the performance of the plasma liner as an effective pusher. Finite backpressure on the target was also neglected until stagnation occurred. The model required the liner to remain supersonic at the stagnation radius in order for a self-consistent flow solution to be possible for the modeling of the liner as it continues to implode upon the target. The model found that deuterium-tritium plasma jets with Mach numbers on the order of 60 and implosion velocities on the order of 100 km/s are needed in order to compress the fusion target fuel to a pressure on the order of 60 Mbar and achieve ignition [87].

3.4 PJMIF Experiments

One of the experiments intended to further the advancement of the PJMIF concept is the PLX project, a collaborative effort among several institutions led by Los Alamos National Laboratory. The objective of the PLX project is to explore the feasibility of forming a spherically imploding plasma liner by merging 30 plasma jets fired from plasma guns. Future experiments may use series of jets to form a D-T target at the center of a

fusion reaction chamber, followed by another set of jets firing an afterburner layer of D-T along with the liner gas [88]. The plasma jets may consist of argon, krypton, or xenon. Another approach is to fire jets that contain all the required target and liner materials simultaneously.

Using a heavier element provides higher mass for a limited number density while providing the necessary kinetic energy at a lower velocity. A heavier element also enhances the Mach number of the jets, which helps achieve higher stagnation pressures. The heavier gas has many bound electrons that provide atomic line radiation and cooling that help to keep the liner cool and compressible. The heavy gas in the liner also traps radiation from the burning fusion fuel, which helps to enhance confinement time. Higher jet masses and velocities require a larger amount of gun current, which in turn requires more charge voltage and energy stored in capacitors [89].

Many factors influence the number of jets that are to be used. When the jet merging radius is large, a large number of jets is favored. This offers better symmetry and uniformity of the liner, minimizes the merging angle and resulting shock heating between adjacent jets, and helps to reduce the size, energy, and mass required for each jet. A smaller number of jets is favored if the merging radius is small. Fewer jets also have less demanding engineering and maintenance requirements. Adiabatic expansion and radiation cooling causes the temperature of the jets to and the Mach number to rise. An ionized plasma jet that has a modest Mach number may be formed and accelerated such that the Mach number doubles once the jet reaches the merging radius. When the jets begin to merge, it is possible that oblique shocks may form. However, the ion collisional mean free path of the jets is on the order of the jet radius. This could cause interpenetration of the ions in the jets, and it

possible that a shock may not form at all. As the liner implodes on the target, non-uniformity will evolve and may reduce peak pressure and exacerbate instabilities in the plasma [89].

Merritt et al. conducted experiments with merging two supersonic plasma jets at Los Alamos and found oblique shocks formed, measuring the time evolution of the oblique shock formation as well as the formation of a stagnation layer [90, 91]. These experiments illustrate the importance of accurate shock capturing when simulating liner formation. This is another physics realm that SPFMax has been shown to offer accuracy [92, 93].

Hsu et al. have designed experiments for the PLX project to form a spherically imploding plasma liner from six supersonic plasma jets [94]. SPFMax simulations were shown to yield density variations consistent with experimental data [93].

3.5 Summary of PJMIF Modeling Studies

Table 3.1 summarizes the studies that focused on simulating the PJMIF concept outlined in Section 3.3, listing the number of dimensions, transport physics, and equations of state that were used in each study, as well as whether or not burn physics were incorporated.

Table 3.1. Summary of PJMIF modeling studies.

Reference	Number of Dimensions	Burn Physics	Transport	EOS
Knapp et al. [78]	1	Yes	Radiation Electron and ion thermal conduction Two-temperature	Tabular
Cassibry et al. [86]	3	No	Thermal convection	Ideal gas
Santarius [81]	1	Yes	Radiation Electron and ion thermal conduction Two-temperature	Tabular
Samulyak et al. [75]	1	Yes	No heat transport	Ideal gas
Kim et al. [82]	1	No	Heat conduction	Tabular
Kim et al. [83]	3	No	Heat conduction	Tabular
Awe et al. [84]	1	No	Radiation Electron and ion thermal conduction Two-temperature	Ideal gas and tabular
Davis et al. [85]	1	No	Radiation Heat conduction Two-temperature	Tabular
Parks [87]	1	No	Heat conduction Radiation	Ideal gas

From this table, it can be seen that the majority of PJMIF studies used one-dimensional simulations, with all of the studies that incorporated burn physics being one-dimensional. The studies that used three-dimensional simulations used fewer transport physics compared to the one-dimensional studies. This illustrates the contribution that this

dissertation makes to the field of fusion research by simulating the PJMIF concept in three dimensions while incorporating pertinent transport physics and burn physics, which no previous study in the open literature has done.

CHAPTER 4

NUMERICAL MODEL

4.1 Introduction

Many future experiments must be conducted in order to develop a viable option for fusion and spacecraft propulsion. Due to the high cost of building experimental fusion devices, it is crucial that thorough mathematical models of fusion concepts are developed before an experimental apparatus is built.

The University of Alabama in Huntsville is developing a smoothed particle hydrodynamics code (SPH) entitled Smooth Particle Fluid with Maxwell equation solver (SPFMax) [95, 96] with the goal of simulating magneto-inertial fusion applications. The code has been benchmarked and found to accurately simulate radiation cooling, heat transfer, oblique shock capturing, angular momentum conservation, and viscous effects, and the accuracy was found to be consistent with what has been reported in other SPH studies [93, 97]. This code has been used to simulate both solid-state and magnetic nozzles for pulsed fusion propulsion applications [98, 99], as well as electrode erosion for Z-pinch

fusion systems [95]. The equations of motion and implementation of the smooth particle hydrodynamic method are described in the following sections.

4.2 Equations of Motion

In a typical Lagrangian code, conservation of mass is given by [100]

$$\frac{d\rho}{dt} + \rho\nabla \cdot \boldsymbol{u} = 0 \tag{4.1}$$

where $\frac{d}{dt}$ indicates the material derivative.

SPFMax solves conservation of mass exactly by obtaining density from the particle mass divided by the particle volume, with particle mass being a constant property. Particle positions are updated with a time integration of the velocity vector,

$$\frac{d\boldsymbol{r}}{dt} = \boldsymbol{u} \tag{4.2}$$

Particle acceleration is computed with the single fluid momentum equation [100],

$$\frac{d\boldsymbol{u}}{dt} = -\frac{1}{\rho}\nabla p + \frac{1}{\rho}\nabla \cdot \boldsymbol{\tau} \tag{4.3}$$

where the viscous stress tensor is given by

$$\boldsymbol{\tau} = \begin{bmatrix} \tau_{xx} & \tau_{xy} & \tau_{xz} \\ \tau_{yx} & \tau_{yy} & \tau_{yz} \\ \tau_{zx} & \tau_{zy} & \tau_{zz} \end{bmatrix} \tag{4.4}$$

The momentum equation expands into three vector components, and for an x, y, z coordinate system expands to [100]

$$\frac{du}{dt} = \frac{1}{\rho}\left(-\frac{\partial p}{\partial x} + \frac{\partial \tau_{xx}}{\partial x} + \frac{\partial \tau_{yx}}{\partial y} + \frac{\partial \tau_{zx}}{\partial z}\right) \tag{4.5}$$

$$\frac{dv}{dt} = \frac{1}{\rho}\left(-\frac{\partial p}{\partial y} + \frac{\partial \tau_{xy}}{\partial x} + \frac{\partial \tau_{yy}}{\partial y} + \frac{\partial \tau_{zy}}{\partial z}\right) \tag{4.6}$$

$$\frac{dw}{dt} = \frac{1}{\rho}\left(-\frac{\partial p}{\partial z} + \frac{\partial \tau_{xz}}{\partial x} + \frac{\partial \tau_{yz}}{\partial y} + \frac{\partial \tau_{zz}}{\partial z}\right) \tag{4.7}$$

For a Newtonian fluid, the sheer stress terms are given by

$$\tau_{xy} = \tau_{yx} = \mu\left(\frac{\partial v}{\partial x} + \frac{\partial u}{\partial y}\right) \tag{4.8}$$

$$\tau_{yz} = \tau_{zy} = \mu\left(\frac{\partial w}{\partial y} + \frac{\partial v}{\partial z}\right) \tag{4.9}$$

$$\tau_{zx} = \tau_{xz} = \mu\left(\frac{\partial u}{\partial z} + \frac{\partial w}{\partial x}\right) \tag{4.10}$$

$$\tau_{xx} = \lambda(\nabla \cdot \boldsymbol{u}) + 2\mu\frac{\partial u}{\partial x} \tag{4.11}$$

$$\tau_{yy} = \lambda(\nabla \cdot \boldsymbol{u}) + 2\mu\frac{\partial v}{\partial y} \tag{4.12}$$

$$\tau_{zz} = \lambda(\nabla \cdot \boldsymbol{u}) + 2\mu\frac{\partial w}{\partial z} \tag{4.13}$$

The Stokes hypothesis gives the bulk viscosity coefficient as

$$\lambda = -\frac{2}{3}\mu \tag{4.14}$$

The governing equations in SPFMax are based on the Lagrangian form of the single fluid, two-temperature equations, with one energy equation for ions and neutral particles and one energy equation for the electrons. This similar to the approach found in [101, 102]. The energy equation for the ions and the neutral particles is given by

$$\frac{de_i}{dt} = \frac{1}{\rho}\Bigg(-p_i \nabla \cdot \boldsymbol{u} + \frac{\partial(u\tau_{xx})}{\partial x} + \frac{\partial(u\tau_{yx})}{\partial y} + \frac{\partial(u\tau_{zx})}{\partial z} + \frac{\partial(v\tau_{xy})}{\partial x} + \frac{\partial(v\tau_{yy})}{\partial y} + \frac{\partial(v\tau_{zy})}{\partial z} + \frac{\partial(w\tau_{xz})}{\partial x} + \frac{\partial(w\tau_{yz})}{\partial y} + \frac{\partial(w\tau_{zz})}{\partial z} + \nabla \cdot (k_i \nabla T_i)\Bigg) + Q_{ei} + Q_i \tag{4.15}$$

The energy equation for the electrons is given by

$$\frac{de_e}{dt} = -\frac{p_e}{\rho}\nabla \cdot \boldsymbol{u} + \frac{1}{\rho}\nabla \cdot (k_e \nabla T_e) - 4\sigma T_e^4 \chi_{Planck} - Q_{ei} + Q_e \tag{4.16}$$

where Q_{ei} is the electron/ion equilibration term and is given by [103]

$$Q_{ei} = \frac{3m_e Z k_B}{m_i^2}\frac{(T_e - T_i)}{\tau_e} \tag{4.17}$$

the electron collision time is given by [103]

$$\tau_e = \frac{3\sqrt{m_e}}{4\sqrt{2\pi}}\frac{(k_B T_e)^{3/2}}{\ln \Lambda \, q^4} \tag{4.18}$$

The calculation of the ion and electron heating from fusion reactions (Q_i and Q_e) are provided in Section 4.4.

The equations of motion are closed with various equations of state. In this dissertation, tabular equations of state were generated using PROPACEOS [104]. The numerical output from PROPACEOS gives tables of pressure, ionization state, temperature, radiation opacities, ion viscosity, and thermal conductivities as a function of density and specific internal energy.

4.3 Stopping Power

The fuel density and burn wave propagation are crucial for achieving ignition in fusion fuel targets. A fusion plasma burns when charged particles deposit their energy into the plasma and initiate further fusion reactions, with the newly formed charged particles providing further heating of the plasma through electron thermal conduction and the plasma's stopping power. Charged particles deposit their energy into the plasma through small angle collisions with plasma background species and large angle collisions through binary particle interactions.

Stopping power models have been developed by Brown et al [105], Li et al [106], Long et al [107], and Harris et al [108]. The stopping power model used in SPFMax was developed by Grabowski et al and has been shown to be accurate over a large parameter space for nonrelativistic molecular dynamics [109]. For completeness, the equations used in this model are given below, but for a discussion see [110, 111].

$$\frac{dE}{dx} = \frac{d\tilde{E}}{dx}\frac{Z^2 q_e^2/\lambda_D^2}{(1+g)^{2/3}} \tag{4.19}$$

$$\frac{d\tilde{E}}{dx} \approx -R(w)\left[G(w)\ln\left(e^{1/2} + \frac{\alpha + w^2}{g_0}\right) + H(w)\right] \tag{4.20}$$

$$R(w) = \frac{[M_1 + bM_2(w)w^2](g)^{2/3}}{w^2(1+bw^2)} \tag{4.21}$$

$$M_1 = \frac{s\ln\left(1 + \alpha e^{1/2}/[g(1+aZ^2 g)]\right)}{\ln(1+\alpha e^{1/2}/g_0)} \tag{4.22}$$

$$M_2(w) = \frac{1}{s^2}\frac{\ln(1+s^3 w^3/g)}{\ln(1+w^3/g_0)} \tag{4.23}$$

$$G(w) = erf\left(\frac{w}{\sqrt{2}}\right) - \sqrt{\frac{2}{\pi}} w e^{-w^2/2} \tag{4.24}$$

$$H(w) = \frac{w^4 \ln w}{12 + w^4} - \frac{w^3}{3\sqrt{2\pi}} e^{-w^2/2} \tag{4.25}$$

$$g = \frac{Ze^2}{\lambda_D k_B T} \tag{4.26}$$

$$\alpha = 4e^{-2\gamma} \tag{4.27}$$

$$s = d(1 + cg)^{1/3} \tag{4.28}$$

$$w = \frac{v}{v_{th} s} \tag{4.29}$$

$$a = 1.04102 \times 10^{-5} \tag{4.30}$$

$$b = 0.183260 \tag{4.31}$$

$$c = 0.116053 \tag{4.32}$$

$$d = 0.824982 \tag{4.33}$$

$$g_0 = 2.03301 \times 10^{-3} \tag{4.34}$$

This model has been successfully implemented in SPFMax and shown to accurately characterize the stopping power for different fusion plasmas across a wide range of densities and temperatures [110, 111].

4.4 Nonlocal Radiation Transport in SPFMax

Ideally, radiation of a fusion fuel target would be modeled in SPFMax with each particle being a source of radiation emitting isotropically across a continuous radiation frequency or fission/fusion product energy and reabsorbed, scattered, refracted and/or

transmitted in accordance with the local radiation matter interaction physics. However, this would be far too computationally intensive to implement in three dimensions. Therefore, the algorithm for modeling nonlocal deposition of energy is a compromise between accuracy and computer memory.

The algorithm specifies a ray geometry that acts as a 4π isotopic source of radiation in which matter and radiation interact, with the radiation intensity decreasing as a function of $1/r^2$ [111]. This is illustrated in Figure 4.1

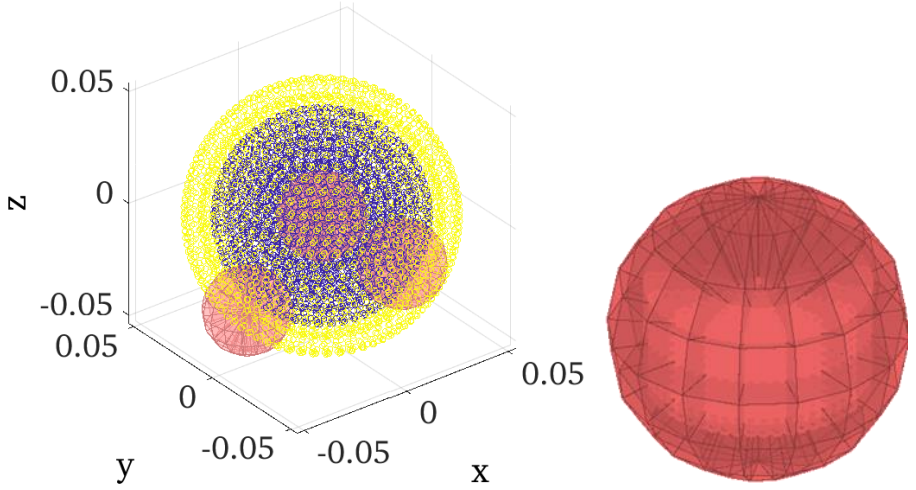

a) b)

Figure 4.1. Rays shown in a computational domain for a) a spherical MIF target and liner with b) 4π ray.

In Figure 4.1 a), the blue and yellow particles represent a typical spherical MIF plasma target and liner, respectively. The smaller red spheres are shown as representative

of the 4π rays, which are evenly distributed throughout the domain to approximate the radiation matter interactions. In Figure 4.1 b), one of the rays is shown for illustrative purposes. The centerline of the ray branches are the assumed trajectories of the radiation, and each branch is subdivided so that spatial variations in attenuation can be modeled. Each radiating SPH particle will contribute its power to the closes ray segment.

The reactivity for a reaction of species i with species j is given by

$$\frac{dN}{dt} = \frac{n_{X_i} n_{X_j}}{1 + \delta_{ij}} < \sigma v >_{ij} V \tag{4.35}$$

in which

$$\delta_{ij} = \begin{cases} 1 & i = j \\ 0 & i \neq j \end{cases} \tag{4.36}$$

The power per unit mass delivered by a particular fusion product species k is given by

$$\left(\frac{de}{dt}\right)_k = \frac{n_{X_i} n_{X_j}}{\rho(1 + \delta_{ij})} <\sigma v>_{ij} E_k \tag{4.37}$$

The total power of the system is

$$P_{fus,k} = \sum_{a=1}^{N} \frac{n_{a,X_i} n_{a,X_j}}{(1 + \delta_{ij})} <\sigma v>_{a,ij} E_k V_a \tag{4.38}$$

The fraction of fusion power deposited in a segment of ray r is given by

$$f_r = \frac{\Omega}{4\pi} \tag{4.39}$$

The work done by a fusion ion moving through segment i of the ray is

$$\delta W_{ir} = \left(\frac{dE}{dr}\right)_{ir} \Delta r_{ir} \tag{4.40}$$

The ion and electron power deposited in a given ray segment is [111]

$$\left(Q_{i,e}\right)_{ir} = \left(\frac{n_{X_i} n_{X_j}}{1+\delta_{ij}} \langle \sigma v \rangle_{ij} V \frac{\Omega}{4\pi} \left(\frac{\partial E}{\partial r}\right)_{ir} \Delta r\right) \tag{4.41}$$

in which $\left(\frac{dE}{dr}\right)_{ir}$ is the function calculating the deceleration force acting on the fast particles, which is a function of ion species, electron density, and temperature.

The local stopping power itself is a function of the kinetic energy of the fast ions moving through the ray segment. It is assumed that the stopping power is constant through a given ray segment. Therefore, the change in kinetic energy of an ion moving through the specific ray segment is given by

$$\frac{1}{2} m_k v_{k,ir}^2 - \frac{1}{2} m_k v_{k,i(r-1)}^2 = -\delta W_{ir} \tag{4.42}$$

The ion velocity is then found from

$$v_{k,ir} = max\left[\left(v_{k,i(r-1)}^2 - \frac{2\delta W_{ir}}{m_k}\right), 0\right] \tag{4.43}$$

The ion power is given by

$$\frac{1}{2} m_k v_{k,ir}^2 - \frac{1}{2} m_k v_{k,i(r-1)}^2 = -\delta W_{ir} \tag{4.44}$$

The ion power is then distributed to the particles in the ray segment based on the compact support size of each particle. The actual power per unit mass deposited in an SPH particle 'a' is then

$$\left(Q_{i,e}\right)_a = \sum_{ir=1}^{number\ of\ rays} \left[\frac{h_a}{m_a}\left(\frac{n_{X_i} n_{X_j}}{1+\delta_{ij}} \langle \sigma v \rangle_{ij} V\right)_{ir} \left(\frac{\Omega_r}{4\pi}\right)_a \left(\frac{dE}{dr}\right)_{ir}\right] \tag{4.45}$$

4.5 Smoothed Particle Hydrodynamics

SPH is a meshless Lagrangian method that simulates fluid flows by dividing a fluid into a set of particles and using a summation interpolant function to calculate the properties and gradients for each of these particles. A kernel function is then used to calculate the properties for each of the particles by adding up the properties of the particles that lie within the kernel. The properties assigned to a specific particle are determined based on the density and proximity of other nearby particles [112-114].

There are three common methods used to compute density from an arbitrary distribution of point mass particles in SPH. One approach is to construct a mesh and divide the mass in each cell by the volume. A limitation of this approach is that a fixed mesh can under sample or over-sample regions with spare or dense mass distributions. This approach must also interpolate both to and from the particles, which can cause a loss of accuracy, speed, and consistency [115].

Another approach is to have no mesh at all, and instead calculate the density based on a local sampling of the mass distribution. This can be accomplished by dividing the total mass by the volume of the sample. Clustered and sparse regions can be dealt with by adjusting the size of the sampling volume according to the local number density of sampling points. A drawback of this approach is that it may lead to a noisy estimate because the estimation of the density will be very sensitive to whether or not a distant particle on the edge of the volume is used when finding the estimate. This requires smoothing distances in the SPH algorithm so that distant particles have smaller influence when calculating local estimates [115].

The third approach is to calculate the density using a weighted summation over nearby particles [115]. These three methods are illustrated in Figure 4.2

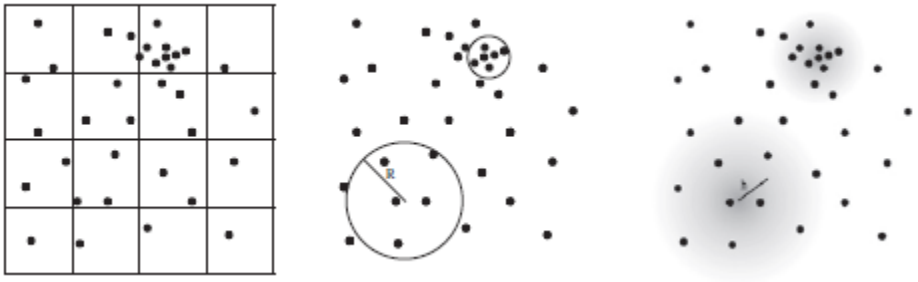

Figure 4.2. The three methods used for calculating density in SPH [43].

SPFMax uses the third technique, with the density computed from

$$\rho_a = \sum_b m_b W_b \tag{4.46}$$

For the kernel approximation, an integral interpolant can be used to obtain the value for any property in a fluid, and is defined as [116]

$$A(\boldsymbol{r}) = \int A(\boldsymbol{r}')\delta(\boldsymbol{r} - r')dr' \tag{4.47}$$

The delta function is given by

$$\delta(\boldsymbol{r} - \boldsymbol{r}') = \begin{cases} 1 & \boldsymbol{r} = \boldsymbol{r}' \\ 0 & \boldsymbol{r} \neq \boldsymbol{r}' \end{cases} \tag{4.48}$$

By replacing the delta function with a smoothing function, the kernel approximation can be expressed as

$$A(\boldsymbol{r}) = \int A(\boldsymbol{r}')W(\boldsymbol{r} - \boldsymbol{r}', h)d\boldsymbol{r}' \tag{4.49}$$

The smoothing function is required to meet several conditions. The first is the normalization condition, which can be expressed as

$$\int W(\boldsymbol{r} - \boldsymbol{r}', h)d\boldsymbol{r}'\,(\boldsymbol{r}) = 1 \tag{4.50}$$

The second condition that must be met is the Delta function property, which is given by

$$\lim_{h\to 0} W(\boldsymbol{r} - \boldsymbol{r}', h) = \delta(\boldsymbol{r} - \boldsymbol{r}') \tag{4.51}$$

The third condition is the compact condition and is given by

$$W(\boldsymbol{r} - \boldsymbol{r}', h) = 0 \;\; when\; |\boldsymbol{r} - \boldsymbol{r}'| > \kappa h \tag{4.52}$$

After the kernel function has been applied, the particle approximation is utilized. In the particle approximation, the system is represented by a finite number of particles characterized by a specific mass and location. The continuous integral representations in the kernel approximation are converted to discretized forms of summation over all of the particles that lie within the support domain. This allows the integral interpolant to be approximated with a summation interpolant given by

$$A(\boldsymbol{r}) = \sum_b m_b \frac{A_b}{\rho_b} W(\boldsymbol{r} - \boldsymbol{r}_b, h) \tag{4.53}$$

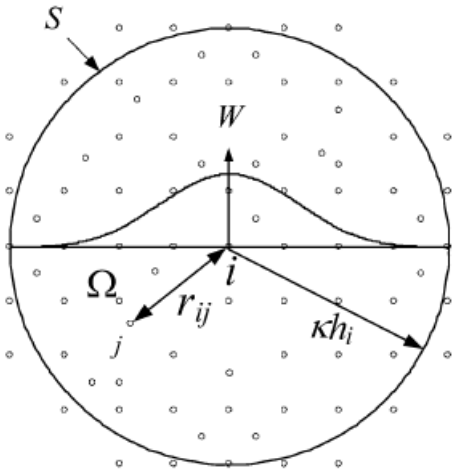

Figure 4.3. SPH particle approximations in a two-dimensional problem domain Ω with a surface S [117].

The spatial gradient for this quantity can be computed using the equation summation

$$\nabla A(\boldsymbol{r}) = \sum_b m_b \frac{A_b}{\rho_b} \nabla W(\boldsymbol{r} - \boldsymbol{r}_b, h) \tag{4.54}$$

Many kernel functions may be used in SPH [118, 119]. A Gaussian kernel was used by Gingold and Monahan to simulate non-spherical stars, and this kernel was found to be sufficiently smooth for high order derivatives and offer both stability and accuracy. However, this kernel function is not very compact and is computationally expensive due to it taking a long distance for the kernel to approach zero, which in turn requires a large support domain with a large number of particles [112, 117]. One of the most frequently used kernels is the cubic spline kernel, which is given by

$$W_{ab} = \begin{cases} \frac{1}{4\pi {h_{ab}}^3}[(2-q)^3 - 4(1-q)^3] & for\ 0 \le q \le 1 \\ \frac{1}{4\pi {h_{ab}}^3}(2-q)^3, & for\ 1 \le q \le 2 \\ 0 & for\ q > 2 \end{cases} \tag{4.55}$$

The cubic spline closely resembles a Gaussian function while requiring a more narrow compact support. Higher order kernels have been studied and offer high accuracy for particles that are equally spaced. However, when the particles are disorganized, higher order kernels require a cancellation of positive and negative contributions, which is not likely when there is disorganization in the particles. The changing of gradient signs for higher order kernels also causes a loss in desirable features of SPH, such as positive definite dissipation terms [114].

The actual degree of accuracy depends strongly on the particle distribution within the kernel radius and the properties of the kernel within a set of neighboring particles. The ratio of smoothing length to particle spacing also has a major influence on accuracy [115]. SPH has been used to model many problems in fluid dynamics, such as star formation, oceonagraphy, and lava flows [120, 121].

4.5.1 First and Second Order Derivatives

Several numerical schemes have been evaluated to calculate first and second derivatives in SPH, each having their own advantages and disadvantages. The scheme developed by Monaghan to calculate first derivatives is given by [122, 123]

$$\nabla A_i = \sum_j \omega_j A_j \nabla W_{ij} \tag{4.56}$$

A second scheme for calculating first derivatives is given by [123]

$$\nabla A_i = \sum_j \omega_j \left(A_j - A_i\right) \nabla W_{ij} \tag{4.57}$$

This scheme is able to obtain a first derivative that is exactly zero for a constant function, a capability that the first scheme lacks.A third scheme is given by [123]

$$\nabla A_i = \sum_j \omega_j \left(A_j + A_i\right) \nabla W_{ij} \tag{4.58}$$

This form does not have zeroth order consistency. However, it can provide local momentum conservation when it is used to discretize forces in Euler and Navier-Stokes equations.

A fourth scheme used by Randles and Libersky, Bonet and Lok, and Vila is given by [123-126]

$$\nabla u_i = \sum_j \omega_j \left(A_j - A_i\right) \boldsymbol{B}_i \cdot \nabla W_{ij} \tag{4.59}$$

In which the renormalization tensor is given by

$$\boldsymbol{B}_i = -\left[\sum_j \omega_j \left(\boldsymbol{r}_i - \boldsymbol{r}_j\right) \nabla W_{ij}\right]^{-1} \tag{4.60}$$

This method is first-order consistent. However, it is not symmetric, and so it is not always able to preserve conservation of momentum and energy.

Second derivatives can be obtained for each of the schemes used to obtain first derivatives. These are given by the following three equations

$$\nabla \cdot \nabla A_i = \sum_j \omega_j \nabla A_j \cdot \nabla W_{ij} \tag{4.61}$$

$$\nabla \cdot \nabla A_i = \sum_j \omega_j \left(\nabla A_j - \nabla A_i\right) \cdot \nabla W_{ij} \tag{4.62}$$

$$\nabla \cdot \nabla A_i = \sum_j \omega_j \left(\nabla A_j + \nabla A_i\right) \cdot \nabla W_{ij} \tag{4.63}$$

Another option is to determine the second derivative for the kernel function. Applying this to each of the first derivative schemes yields the following three equations

$$\nabla \cdot \nabla A_i = \sum_j \omega_j A_j \nabla \cdot \nabla W_{ij} \tag{4.64}$$

$$\nabla \cdot \nabla A_i = \sum_j \left(A_j - A_i\right) \nabla \cdot \nabla W_{ij} \tag{4.65}$$

$$\nabla \cdot \nabla A_i = \sum_j \omega_j \left(A_j + A_i\right) \nabla \cdot \nabla W_{ij} \tag{4.66}$$

A third scheme was developed by Brookshaw, and incorporates a form for the first derivative similar to a finite difference and an SPH summation for the second derivative. This is given by [123, 127]

$$\nabla \cdot \nabla A_i = \sum_j 2\omega_j \frac{A_i - A_j}{r_{ij}} \boldsymbol{e}_{ij} \cdot \nabla W_{ij} \tag{4.67}$$

in which

$$r_{ij} = \left|\boldsymbol{r}_{ij}\right| \tag{4.68}$$

and

$$\boldsymbol{e}_{ij} = \frac{\boldsymbol{r}_{ij}}{r_{ij}} \tag{4.69}$$

This is among the most accurate schemes for calculating second derivatives in SPH [123, 128].

In SPFMax, it was decided to use the method given in Equation 4.56 to calculate first derivatives and the method given in Equation 4.61 to calculate second derivatives. Among the values this calculates in simulations are the scalar temperature in the heat conduction equation and the spatial derivatives of velocity vectors [125, 129, 130]. This approach was found to offer both satisfactory speed and accuracy for simulating physics problems pertinent to PJMIF. The first example of this implementation was with thermal conduction in the study of electrode erosion [95].

4.5.2 Shock Capturing

SPFMax uses artificial viscosity based on work done by Monaghan while also utilizing a Balsara switch to turn off artificial viscosity in regions of excessive shear stress. The artificial viscosity term Π is added to the pressure terms in the momentum equation to give

$$\frac{du}{dt} = \frac{1}{\rho}\left(-\frac{\partial p}{\partial x} + \frac{\partial \tau_{xx}}{\partial x} + \frac{\partial \tau_{yx}}{\partial y} + \frac{\partial \tau_{zx}}{\partial z}\right) + \frac{\partial \Pi}{\partial x} \tag{4.70}$$

$$\frac{dv}{dt} = \frac{1}{\rho}\left(-\frac{\partial p}{\partial y} + \frac{\partial \tau_{xy}}{\partial x} + \frac{\partial \tau_{yy}}{\partial y} + \frac{\partial \tau_{zy}}{\partial z}\right) + \frac{\partial \Pi}{\partial y} \tag{4.71}$$

$$\frac{dw}{dt} = \frac{1}{\rho}\left(-\frac{\partial p}{\partial z} + \frac{\partial \tau_{xz}}{\partial x} + \frac{\partial \tau_{yz}}{\partial y} + \frac{\partial \tau_{zz}}{\partial z}\right) + \frac{\partial \Pi}{\partial z} \tag{4.72}$$

The artificial viscosity is added to the ion energy equation to give

$$\frac{de_i}{dt} = \frac{1}{\rho}\left(-p_i\nabla\cdot\boldsymbol{u} + \frac{\partial(u\tau_{xx})}{\partial x} + \frac{\partial(u\tau_{yx})}{\partial y} + \frac{\partial(u\tau_{zx})}{\partial z} + \frac{\partial(v\tau_{xy})}{\partial x} + \frac{\partial(v\tau_{yy})}{\partial y}\right.$$
$$\left.\frac{\partial(v\tau_{zy})}{\partial z} + \frac{\partial(w\tau_{xz})}{\partial x} + \frac{\partial(w\tau_{yz})}{\partial y} + \frac{\partial(w\tau_{zz})}{\partial z} + \nabla\cdot(k_i\nabla T_i)\right) + \Pi\nabla\cdot\boldsymbol{u} +$$
$$Q_e + Q_i \tag{4.73}$$

Since the artificial viscosity is computed between a particle and its neighbors, the model presented below uses the subscripts 'a' for the particle and 'b' for the set of neighbors to the particle. This scheme is given by [131]

$$\Pi_{ab} = \begin{cases} \dfrac{-\alpha c\tilde{\mu}_{ab} + \beta_{\Pi}\tilde{\mu}_{ab}^2}{\bar{\rho}_{ab}} & \boldsymbol{v}_{ab}\cdot\boldsymbol{r}_{ab} < 0 \\ 0 & \boldsymbol{v}_{ab}\cdot\boldsymbol{x}_{ab} \geq 0 \end{cases} \tag{4.74}$$

In which

$$\tilde{\mu}_{ab} = \frac{h\boldsymbol{v}_{ab}\cdot\boldsymbol{r}_{ab}}{\boldsymbol{r}_{ab}^2 + 0.01h^2} \tag{4.75}$$

And

$$\beta = \min\left(\beta_{max}, 1 + \frac{d_B}{d_a}\right) \tag{4.76}$$

And

$$\beta_{max} \approx 1.5 \tag{4.77}$$

Artificial viscosity is especially useful in saving numerical computational power when calculating flow conditions before and after shock formation occurs [132].

CHAPTER 5

CODE VERIFICATION

5.1 Introduction

A sequence of simulations converges to a value of ξ with order p if it meets the following criteria

$$|A - \xi| < Cn^{-p} \tag{5.1}$$

in which C is a constant and n is the number of grid points. For code verification, ξ is equal to zero, since the error should approach zero as the resolution increases.

The L^2 norm is a popular norm in the fields of science and engineering that can be used to measure a numerical code's accuracy. Using density as an example, the L^2 norm can be calculated using the following equation

$$L_\rho^2 = \sqrt{\frac{(\rho - \rho_{exact})^2}{n}} \tag{5.2}$$

The L^2 norm provides a global average error. This method can be used to measure the error for density, temperature, pressure, and other properties at different resolutions. A higher resolution generates more particles, which in turn should provide a more accurate

solution. To perform an L^2 analysis, it is necessary to perform simulations of problems in SPH that have analytical solutions.

During the development of SPFMax, physical viscosity, oblique shock capturing, radiative cooling, and heat conduction were incorporated into the code. This was followed by performing verification tests against problems relevant to plasma liner formation for the PJMIF concept. Each of the test cases required an analytical solution in order to assess the accuracy of code in simulating these different physics. Descriptions for these problems and an analysis of the code's numerical accuracy are provided in the following six sections. The simulated problems consisted of optically thin radiation cooling, thermal conduction, Couette flow, the Gresho vortex, oblique shock, and the Taylor-Green vortex. The descriptions and results for each of these studied are provided in the following sections. The results of these test cases were recently published in the Journal of Nuclear Engineering and Radiation Science [93]. For the sake of completeness, the results and discussion are duplicated here.

5.2 Optically Thin Radiation Cooling

The cooling rate for single group radiation in the optically thin limit is given by (see Planck's law in Ref. [133] for example, on pp 318-319)

$$\frac{de}{dt} = 4\sigma T_e^4 \chi_{Planck} \tag{5.3}$$

If it is assumed that the electron and ion temperatures are equal ($T_e = T_i \equiv T$), then the specific internal energy for the system is $e = C_v T$. The value for C_v is then given by

$$C_v = \frac{\bar{R}(1+Z)}{AW(\gamma-1)} \tag{5.4}$$

Thus, in terms of temperature for a calorically perfect gas, the rate of change in temperature becomes

$$\left(\frac{dT}{dt}\right)_{rad} = 4\sigma T^4 \chi_{Planck} \frac{AW(\gamma-1)}{\bar{R}(1+Z)} \tag{5.5}$$

The problem examined consists of a region of argon plasma with a constant ion number density of 10^{22} m^{-3} and an initial temperature of 2 eV. Two simulations were run, with one using Equation 5.3 in which the opacity, specific heat ratio, and charge state were fixed to be consistent with the specified temperature and ion density. The other simulation used Equation 5.5, with the parameters of the plasma being interpolated from an equation of state table during the numerical integration as a function of e and ρ.

Temperature is plotted versus time in Figure 5.1 for both the ideal case of constant opacity and calorically perfect gas and the tabular case in which all properties are a function of ρ and e. In both simulations, cooling occurs rapidly in the first 2 microseconds, followed by a more gradual cooling in the remaining 18 microseconds. The solutions were determined by integration using ODE45, a Matlab algorithm that utilizes a Runge-Kutta numerical integration scheme [134]. The results from the SPH plot are shown for the same two cases as points that fall on top of the exact results, indicating that the radiation model is implemented properly and that the table lookup in the SPH model is performing consistently with the exact solution.

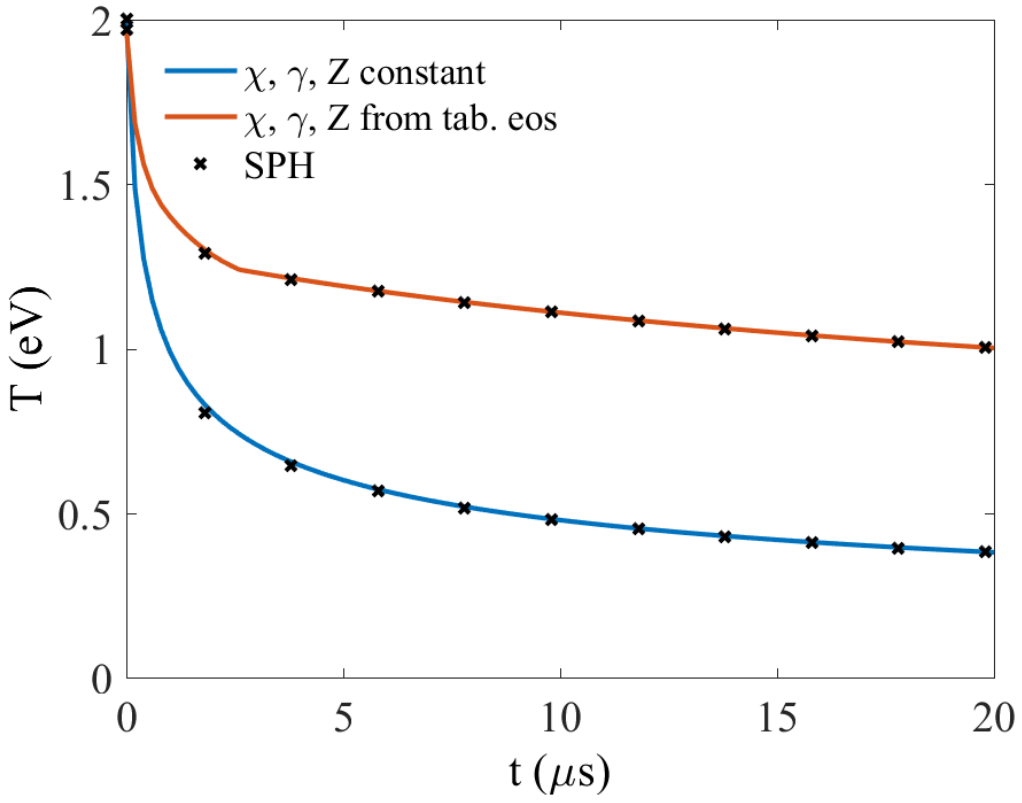

Figure 5.1. Plasma temperature as a function of time. Solid lines indicate exact numerical solution and data points are SPFMax results.

5.3 Thermal Conduction

As the plasma jets merge, shock heating and compressional work heat the exterior of the jets and then thermal transport will contribute to heating the interior of the jets. To verify that SPFMax can capture heat transfer, the heat conduction problem is solved using cylindrical symmetry, where the outer radial boundary is set to a constant temperature that is higher than the interior temperature.

A model for this problem can be derived from the form of the heat equation as given by

$$\rho C_v \frac{\partial T}{\partial t} = \nabla \cdot (k \nabla T) \tag{5.6}$$

This partial differential equation can be solved exactly under the assumption of constant coefficients for various boundary conditions in planar, cylindrical, and spherical geometries in one, two, or three dimensions. This is accomplished by using separation of variables on a non-dimensionalized form of the equation assuming periodic boundary conditions, and infinite boundary condition solutions can be found as well. While solutions can be found in numerous textbooks, the authors found the report by Vansant particularly useful [135]. For constant, uniform temperature T_0 at r_0 and initially uniform temperature T_i, the solution gives

$$T(r,t) = T_0 + 2(T_i - T_0) \sum_{n=1}^{\infty} \frac{1}{\lambda_n} e^{-\lambda_n F_o(t)} \frac{J_0(\lambda_n R)}{J_1(\lambda_n)} \tag{5.7}$$

The test case is illustrated in Figure 5.2

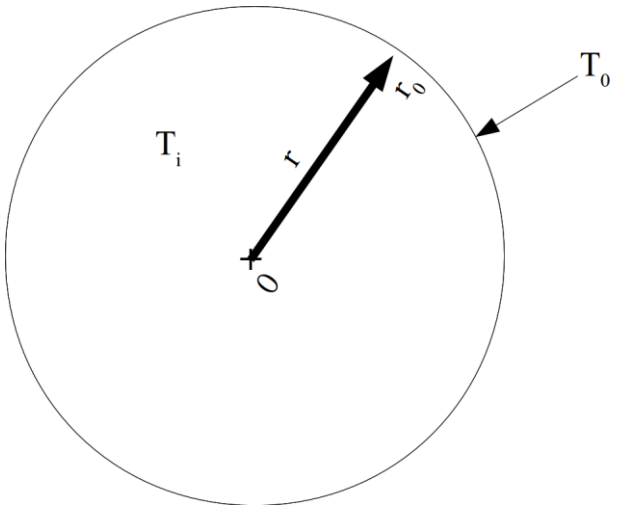

Figure 5.2. Initial conditions for heat conduction problem with cylindrical symmetry.

The problem investigated consists of a cylinder of argon plasma with constant ion density of 10^{22} m^{-3} and an initial temperature of 1 eV. The boundary is set to 10 eV with an initial radius of 2.5 cm. The equation of state and transport properties are found using the PROPACEOS [136] tabular equation of state at an intermediate temperature of 3 eV, with $k = 8.6609$ W/m-K, $AW = 39.948$ kg/kmol, $Z = 2.5587$, and $\gamma = 1.1166$. The series solution is truncated with the first 100,000 terms, evaluated at each point in the spatial direction from r = 0 to 2.5 cm and at times ranging from t = 0 to 100 μs.

Figure 5.3 shows a plot of the temperature versus the radius of the cylinder at fixed times for the exact and numerical solutions. The SPH results were obtained using a line slice through the cylinder located at z = 5, y = 0, and x = -2.5:2.5 cm.

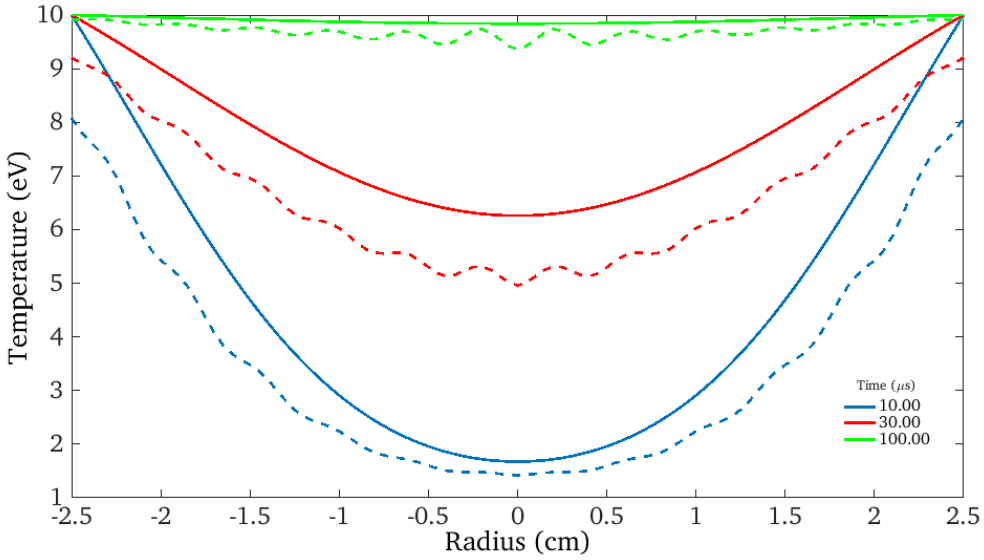

Figure 5.3. Temperature profile at different times for heat conduction problem with cylindrical symmetry. Solid lines indicate exact numerical solution and dotted lines are SPFMax results.

Temperature increases with radius, with a minimum value located at r=0 cm, and a maximum value of 10 eV at the boundary. The temperature profiles change as time progresses to the Fourier time as given by [135]

$$t = F_0 \frac{\rho C_v r_0^2}{k} \tag{5.8}$$

For this problem, the Fourier time is on the order of ~64 microseconds. After this time, the temperature curve becomes constant at 10 eV, as seen by the exact numerical solution in Figure 5.3.

The SPH results can be seen to be in general agreement with the analytical solution, with the difference between the SPH results approaching the analytical solution as time

progresses. This can be further seen in Figure 5.4, which provides an L^2 norm for the temperature versus the number of particles at three fixed times during the simulation run.

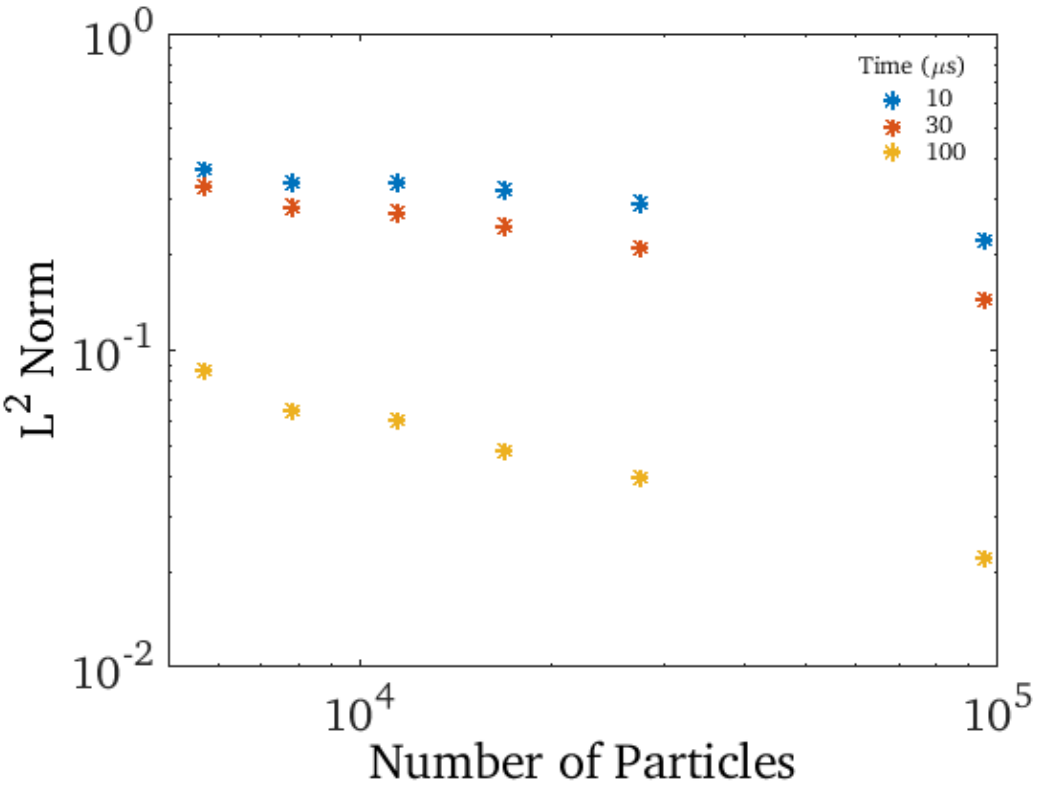

Figure 5.4. Temperature L^2 norm for heat conduction problem in cylindrical symmetry.

The convergence rates can also be seen to improve as the simulation time progresses. The convergence rate for the results at 10, 30, and 100 microseconds are $N^{-0.17}$, $N^{-0.28}$, and $N^{-0.47}$, respectively. This is somewhat lower than convergence rates reported by other SPH studies [137]. The relatively high inaccuracies (20% to 30%) are found at early times when the temperature gradients are most severe. However, for sufficiently high

particle resolution and equilibration times, the numerical accuracy improves to well within 10%.

As the spherical liner converges and stagnates, a hot spot is formed in which heat conduction transfers energy radially outward. Because of this, it was desired to conduct an additional thermal conduction test case for a spherical geometry.

For a sphere with a steady surface temperature of T_0 and uniform initial temperature of T_i, the transient solution for temperature in the sphere as a function of time and radius is given by [135]

$$T(t,r) = (T_i - T_0) * \left\{1 - \frac{1}{(r/r_0)} \sum_{n=1}^{\infty} \left[erfc\left(\frac{2n-1-(r/r_0)}{2\sqrt{F_o(t)}}\right) - erfc\left(\frac{2n-1+(r/r_0)}{2\sqrt{F_o(t)}}\right)\right]\right\} + T_0 \quad (5.9)$$

where the Fourier number is given by

$$F_o(t) = \frac{\alpha t}{r_0^2} \quad (5.10)$$

The diffusivity is given by

$$\alpha = \frac{k}{\rho C_v} \quad (5.11)$$

Figure 5.5 shows a cutaway of the initial thermal condition for the SPH simulation using spherical geometry. This figure illustrates the lower uniform temperature along the surface of the sphere and the higher initial temperature throughout the entire inner volume of the sphere.

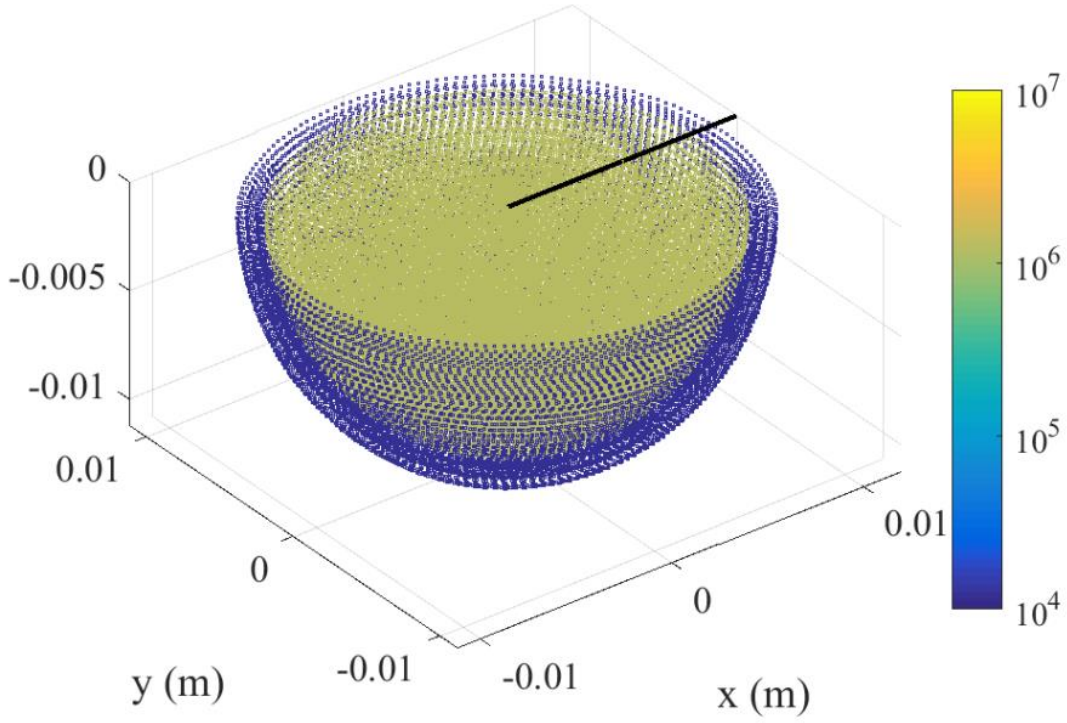

Figure 5.5. Initial condition for heat conduction problem in spherical geometry.

A comparison of the SPH solution with the exact solution for the spherical geometry as a function of time is shown in Figure 5.6. The figure shows the temperature profile at five different points in time. The solid lines are the values for the analytical solution and the dotted lines are the values obtained in SPFMax. In general, the code provides more accurate results closer to the center of the geometry. The accuracy of the SPFMax results is also seen to improve as the simulation progresses in time.

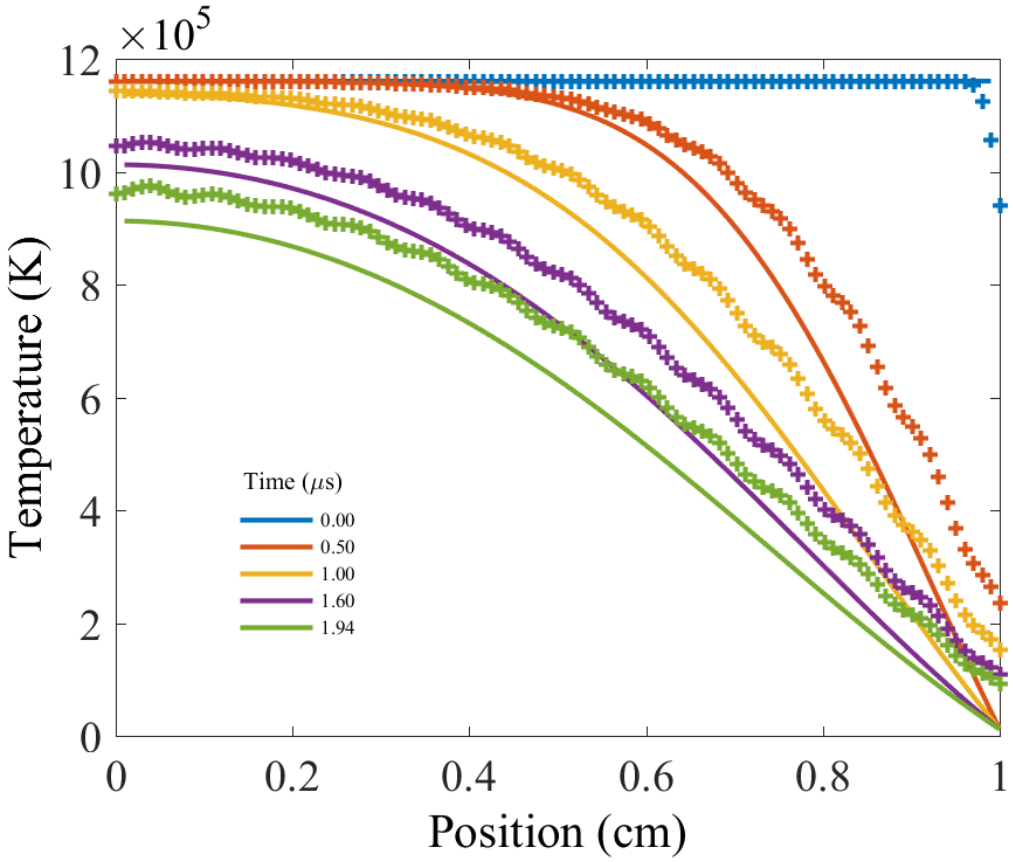

Figure 5.6. Temperature slice comparison of SPH solution with exact numerical solution for heat conduction problem with spherical symmetry. Solid lines indicate exact numerical solution and dotted lines are SPFMax results.

An L^2 analysis for the temperature is given in Figure 5.7. This shows the L^2 norm for temperature converging at a nearly constant linear slope as time progresses. The error is ~6% for most of the simulation.

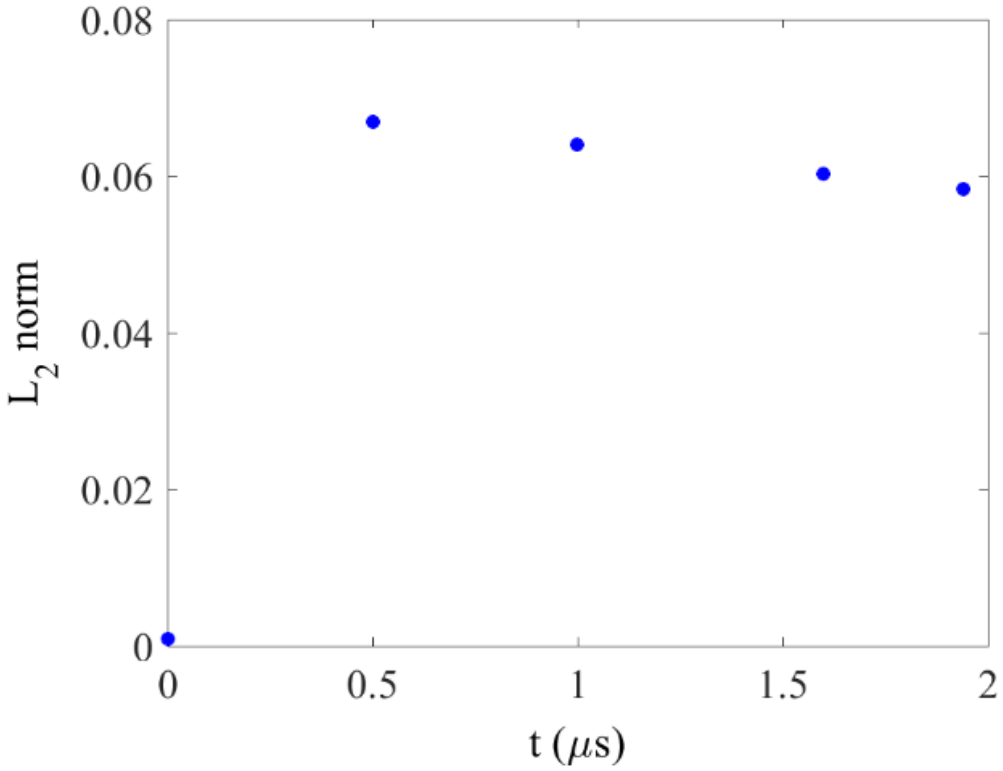

Figure 5.7. L^2 norm at different times for heat conduction problem with spherical symmetry.

The decrease in the L^2 norm can be attributed to the temperature profile becoming more uniform during the simulation.

5.4 Couette Flow

Couette flow consists of a viscous fluid that is contained between two infinite parallel plates. The plates are separated by a constant distance, and the upper plate moves at constant velocity relative to the bottom plate. The flow is incompressible, and the

thermal conduction and dynamic viscosity of the fluid are assumed to be constant. When the no-slip condition is applied to this problem, there is no relative motion between the fluid and the plate [138]. The exact solution for the fluid flow velocity between the plates can then be written as

$$u(y) = u_e \frac{y}{D} \tag{5.12}$$

Figure 5.8 illustrates the velocity profile for Couette flow

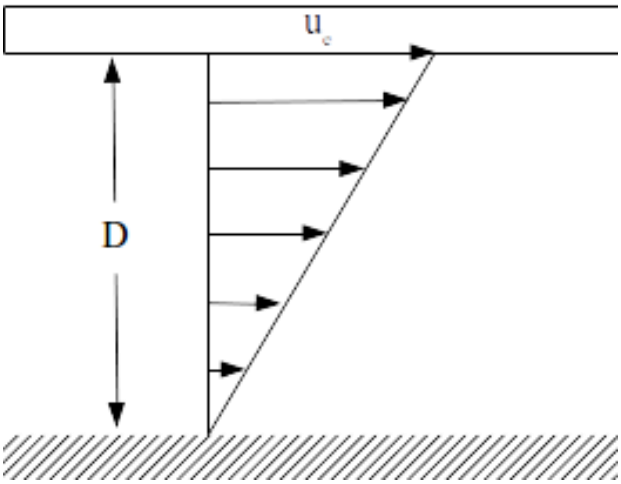

Figure 5.8. Incompressible Couette flow velocity profile.

The SPFMax simulation was two-dimensional and used geometry that was one particle thick in the y direction. The Couette flow problem assumes an infinitely long geometry, making it difficult to simulate in SPH. To address this, periodic boundary conditions were implemented by using an algorithm that transfers particles that move beyond the maximum geometry position in the x direction to the minimum position in the

x direction, and vice versa. This enables a finite geometry to be used in the simulation of Couette flow.

Numerous simulations with different particle numbers were run in order to conduct an L^2 norm analysis. The results for this analysis are presented in Figure 5.9. The convergence rate is on the order of $N^{-0.38}$. This shows that SPFMax is able to incorporate viscous effects in the Navier-Stokes equations with a reasonable level of accuracy and is consistent with the order of accuracy reported in other SPH studies [97]. More importantly, with only 10^4 particles, 10% accuracy is achieved.

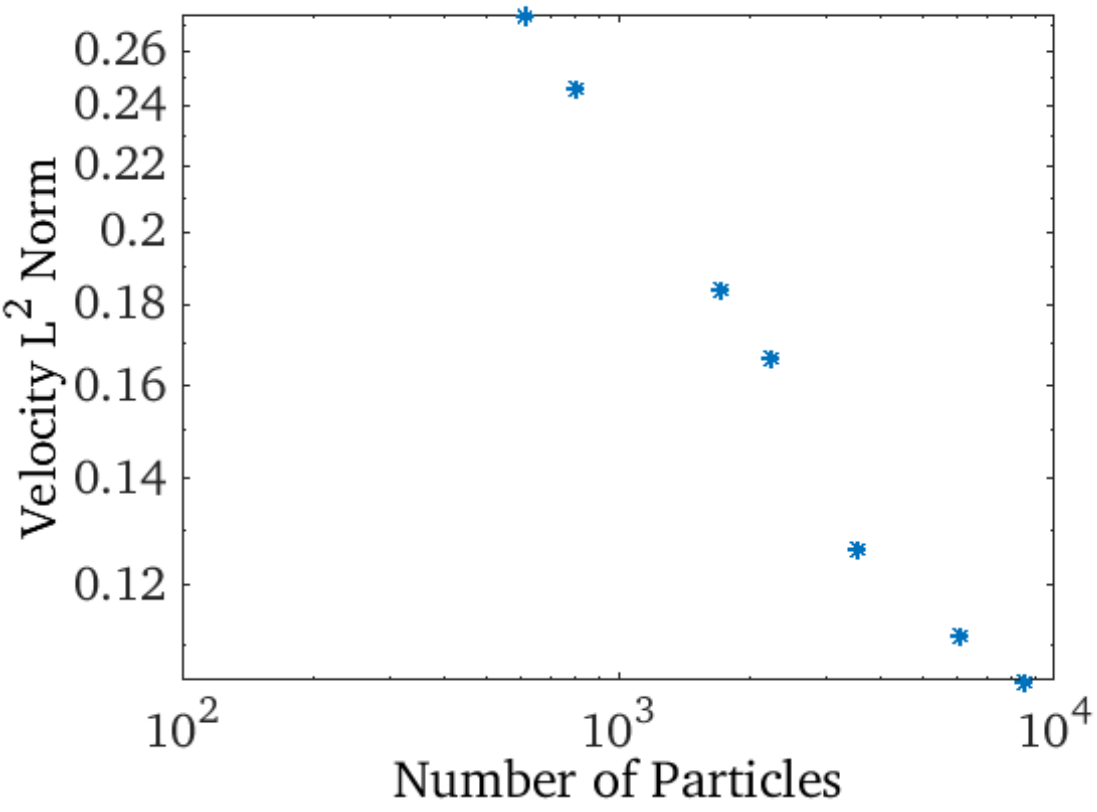

Figure 5.9. L^2 norm for Couette flow velocity.

5.5 Gresho Vortex

The Gresho vortex is an inviscid, time-independent, incompressible problem that consists of a rotating vortex. The azimuthal velocity is dependent only on the radius, and the centrifugal force is balanced by the pressure gradient [139]. The Gresho vortex allows for the testing of a numerical code's preservation of symmetry and conservation of angular momentum as a function of time.

The azimuthal velocity of the vortex is given by

$$u_\phi(r) = \begin{cases} 5r, & 0 \le r \le 0.2 \\ 2 - 5r, & 0.2 \le r \le 0.4 \\ 0, & 0.4 \le r \end{cases} \tag{5.13}$$

The pressure is given by Equation 5.14 and is illustrated as a contour plot in Figure 5.10. As shown, the pressure is lowest in the center of the vortex where the azimuthal momentum is relatively high, which is balanced by the higher pressure surrounding the vortex.

$$p(r) = \begin{cases} 5 + \frac{25}{2} r^2, & 0 \le r \le 0.2 \\ 9 - 4\ln 0.2 + \frac{25}{2} r^2 - 20r + 4\ln r\,, & 0.2 \le r \le 0.4 \\ 3 + 4\ln 2\,, & 0.4 \le r \end{cases} \tag{5.14}$$

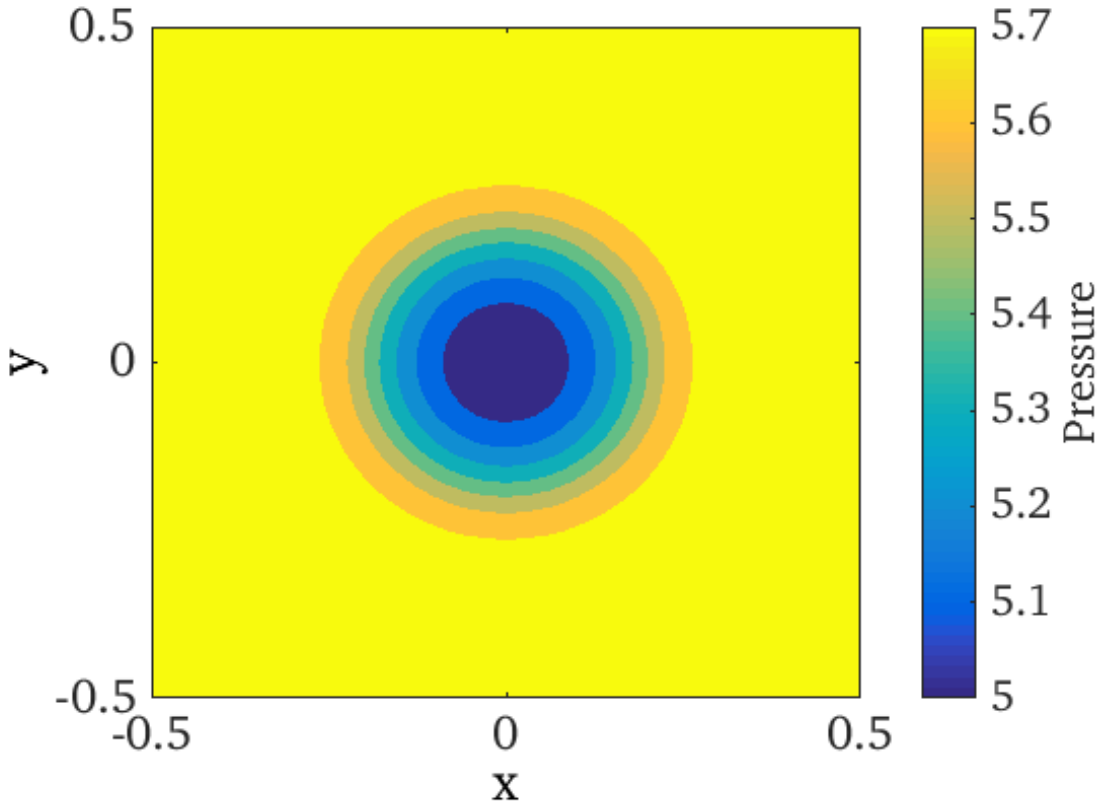

Figure 5.10. Gresho vortex pressure contour.

Figure 5.11 shows contours for the azimuthal velocity of this specific Gresho vortex. This figure shows that the azimuthal velocity is 0 at the center of the vortex, and increases linearly until it reaches a maximum value at r = 0.2. The azimuthal velocity then decreases linearly to 0 once r = 0.4.

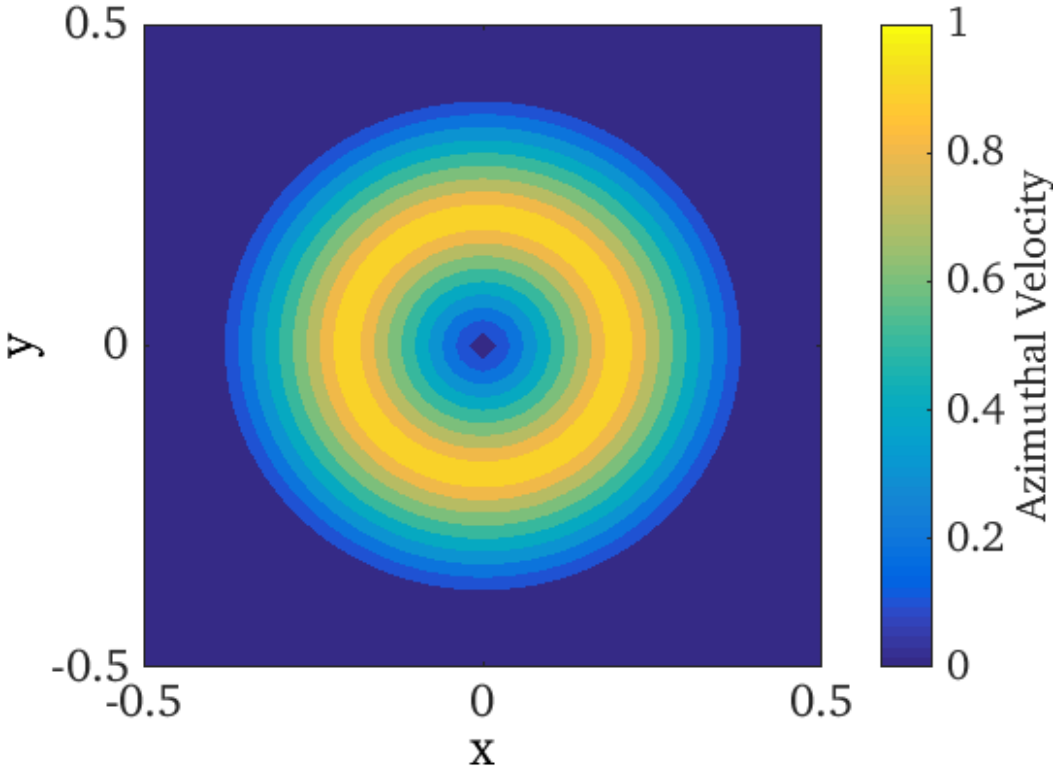

Figure 5.11. Gresho vortex azimuthal velocity contour.

Numerous simulations of this vortex were conducted with SPFMax, each one with a different number of particles. While the Gresho vortex is a time-independent solution, simulations of the vortex inevitably degrade from the analytical solution as time progresses due to factors such as numerical diffusion [97]. Ways to mitigate this include using a Balsara switch [140] to suppress artificial viscosity in the presence of shear to permit inviscid rotational structures in the fluid.

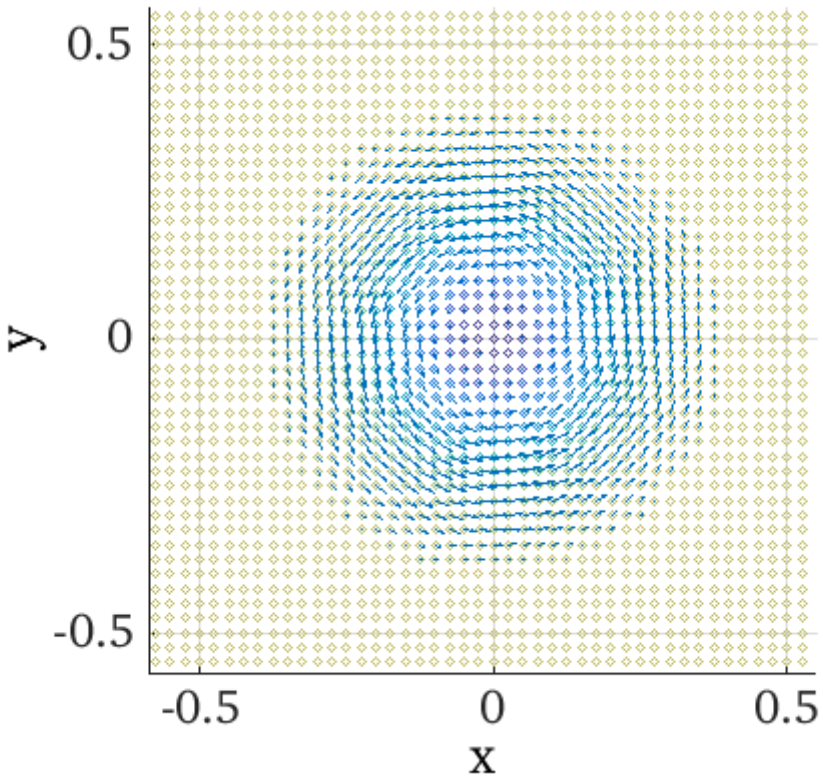

Figure 5.12. SPFMax Gresho vortex simulation, with vectors indicating direction of flow.

A total simulation time of 1.25664 seconds was used for these test cases. This time was selected to allow the fastest rotating fluid in the vortex to undergo one complete rotation. The pressure and angular velocity for each of these simulations were then compared to the profiles given by Equations 5.13 and 5.14, allowing for an L^2 norm to be obtained for both of these parameters. The results for the L^2 norm are presented in the following two figures.

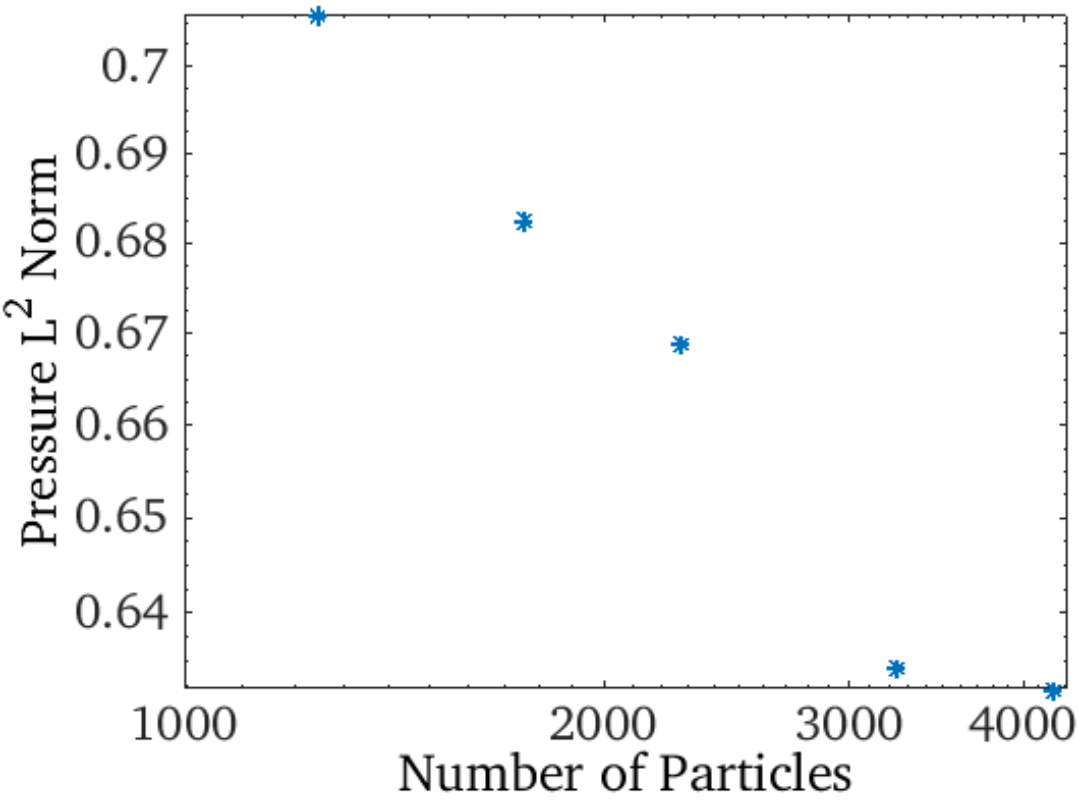

Figure 5.13. L^2 norm for Gresho vortex pressure.

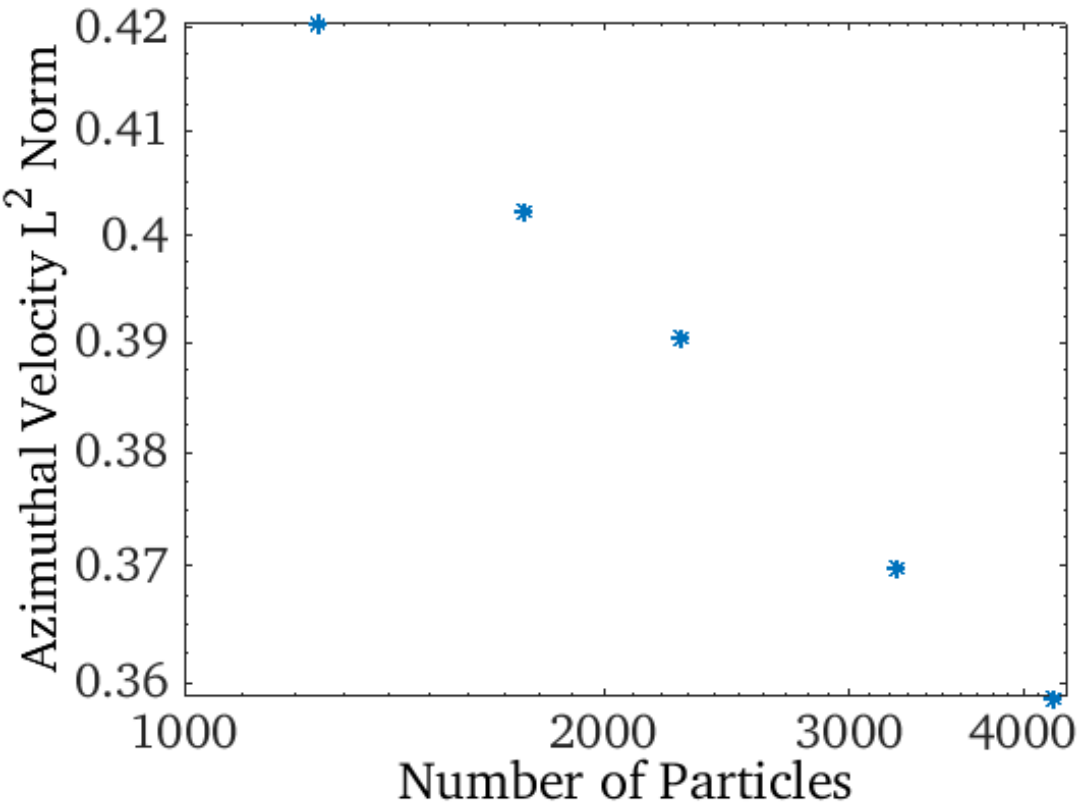

Figure 5.14. L^2 norm for Gresho vortex azimuthal velocity.

The convergence rate of the Gresho vortex pressure is on the order of $N^{-0.13}$ and the convergence rate for the azimuthal velocity is on the order of $N^{-0.1}$. This is somewhat lower than convergence rates that has been reported in other SPH studies [137]. However, it should be noted that most SPH simulations of the Gresho vortex have only evolved the vortex to a time of t=1 s, which is less than one complete rotation of the fastest moving gas particles in the vortex [137]. In comparison, this study simulated one complete rotation of the fastest moving gas particles, which causes further degradation from the analytical solution.

It should also be noted that many SPH codes have been reported to have extreme difficulty in accurately simulating the Gresho vortex. This is due to particle shear motion requiring constant recalculation of the effective particle volume. The changing of the particle volume leads to noise in the volumetric and velocity fields. Artificial viscosity can be used to dampen the velocity noise at the expense of diffusing the vortex [97]. The viscous dissipation resulting from particle motion can also be misinterpreted by the code as the presence of shocks. Better shock capturing methods may improve the accuracy of simulating problems like the Gresho vortex and will be the subject of future work. For this particular problem, MIF flows involving strong mixing, such as late time beyond the onset of Rayleigh-Taylor or Richtmyer-Meshkov instabilities.

5.6 Oblique Shock

In the plasma liner experiment, supersonic plasma jets will merge with half angles between jets of 10 to 20 degrees, and it is anticipated that this will produce oblique shocks since the jets will be deflected in the direction of the jet to jet interfacial plane. Experiments on oblique merging of two supersonic jets were conducted by Merritt et al. for PLX at Los Alamos National Laboratory. These experiments measured the stagnation layer formed by the two obliquely merging supersonic jets and characterized the time evolution of the oblique shock merging [90, 91].

The solution to the so-called jump conditions across a shock can be found in numerous compressible flow textbooks [141]. In the ideal case of a stationary ramp, the

shock angle β, merging half angle θ, and the incoming jet Mach number are related by the so-called θ-β-M relation

$$\tan\theta = 2\cot\beta\left[\frac{M_1^2\sin^2\beta - 1}{M_1^2(\gamma + \cos 2\beta) + 2}\right] \tag{5.15}$$

The jump conditions across the oblique shock are identical in form to those of a normal shock, with the Mach number replaced with the normal component of the Mach number orthogonal to the shock. The normal component of the Mach number is

$$M_{n1} = M_1\sin\beta \tag{5.16}$$

The shock relations for density and pressure are

$$\frac{\rho_2}{\rho_1} = \frac{(\gamma+1)M_{n1}^2}{(\gamma-1)M_{n1}^2 + 2} \tag{5.17}$$

$$\frac{p_2}{p_1} = 1 + \frac{2\gamma}{\gamma+1}(M_{n1}^2 - 1) \tag{5.18}$$

The normal component of the Mach number downstream from the shock is

$$M_{n2}^2 = \frac{M_{n1}^2 + \left[\frac{2}{\gamma-1}\right]}{\left[\frac{2\gamma}{\gamma-1}\right]M_{n1}^2 - 1} \tag{5.19}$$

The actual Mach number downstream of the shock is determined with

$$M_{n2} = M_2\sin(\beta - \theta) \tag{5.20}$$

Using the ideal gas law, the temperature is calculated with

$$\frac{T_2}{T_1} = \frac{p_2}{p_1}\frac{\rho_1}{\rho_2} \tag{5.21}$$

A test case is chosen with initial conditions of two argon jets with conditions comparable to anticipated PLX jet parameters, with a velocity of 40 km/s, a 10 degree

merging half angle, γ = 1.3, an initial mass density of 1.33×10^{-3} kg/m^3, and an initial temperature of 16,247 K (1.4 eV), which corresponds to an initial Mach number of 19.1. Using the oblique shock relations, the exact solution for a stationary ramp gives a shock angle of 12.28 degrees. This implies that the merge layer between the jets should grow at the jet interface with a 2 degree shape (~12 degree shock angle minus 10 degree half angle), a post-shock density of 7.24×10^{-3} kg/m^3, a post shock Mach number of 10.13, and a post-shock temperature of 55,054 K (4.74 eV). It should be noted that the exact solution is not a perfect representation of the merging of two discrete jets, as the leading and trailing edges of the jets provide a two-dimensional relieving effect, which is difficult to quantify. A scatter plot is presented in Figure 5.15 showing the jets at 0, 5, and 10 μs with the particle color scaled to temperature in Kelvin. The shock is shown to form at 5 μs at the interface between the jets and is well defined at 10 μs. Thermal expansion at the edges of the jets are visible at 10 μs. The simulation is performed in the x-z plane with motion in the y-direction prohibited to allow comparison with the exact solution to the oblique shock, which is a two-dimensional solution.

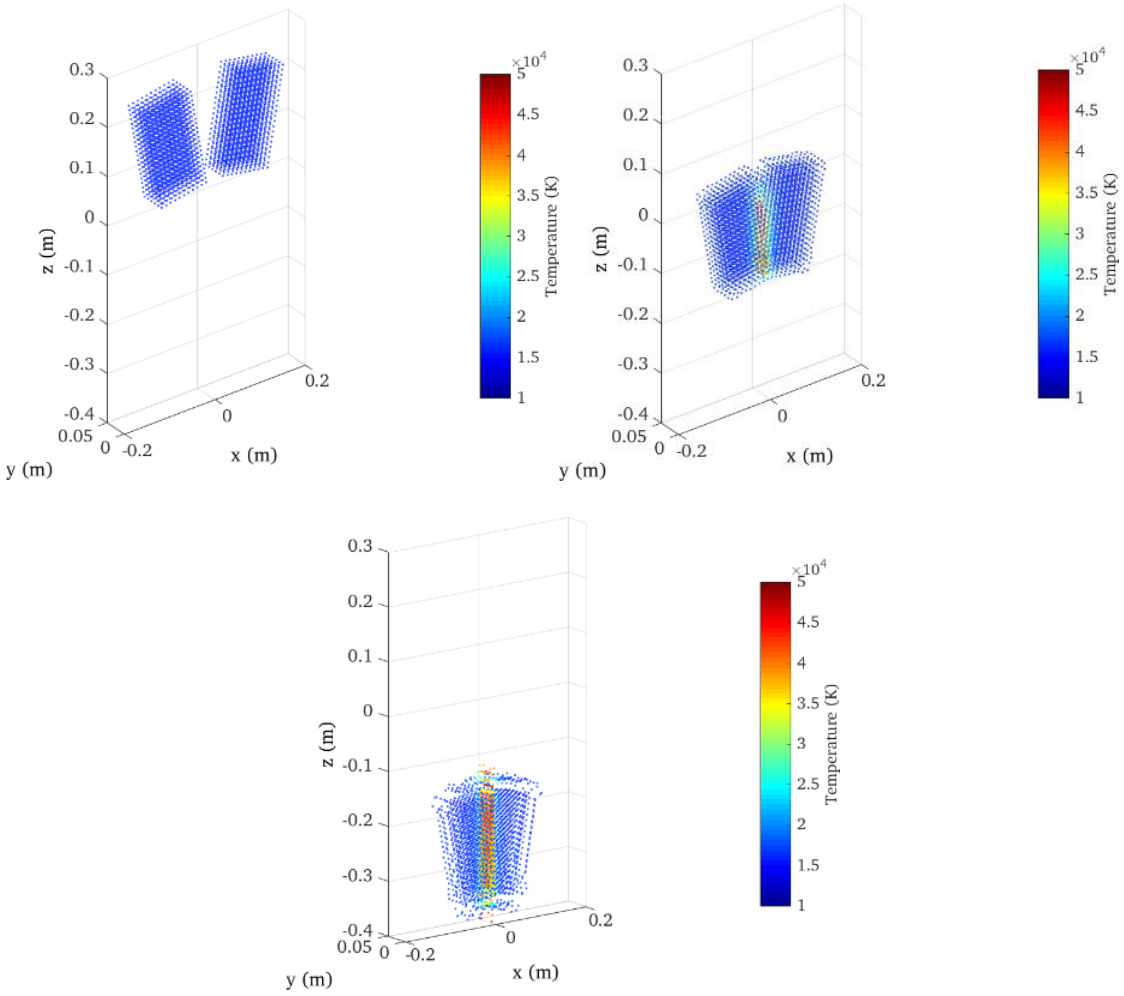

Figure 5.15. Scatter plot of jet temperature for the oblique shock test at 0, 5, and 10 μs. The jets intersect with a merging half angle of 10 degrees, with the shock visible at the jet-jet interface.

In Table 5.1, results are given for the post-shock density, temperature, shock angle, and Mach number for three different particle resolutions. To obtain numerical results, line slices were taken through the numerical output. The shock angle was obtained by generating line slices through the output at three different x_s and z_s locations in the post-

shock region. The z_s positions were examined at a simulation time of 7.5 μs, with the z_s values set to -0.15, -0.185, and -0.22 m.

Table 5.1. Summary of oblique shock test cases with particle numbers varying from 1,386 to 33,728 particles per jet. The exact solution for a stationary ramp gives 12.23 degrees shock angle, and post shock density, temperature, and Mach number of 7.24×10^{-3} kg/m^3, 55,054 K, and 10.13, respectively.

Case	**Number of particles per jet**	**z_s (m)**	**ρ_s (kg/m^3)**	**x_s (m)**	**T_s (K)**	**β (degrees)**	**M_s**
1	1386	-0.15	0.005259	0.0924	41,070	--	11.82
1	1386	-0.185	0.0069323	0.0933	40,100	8.53	11.97
1	1386	-0.22	0.008321	0.093	39,620	10.49	12.02
2	9471	-0.15	0.007807	0.0961	46,720	--	11.04
2	9471	-0.185	0.01049	0.0959	45,960	10.33	11.11
2	9471	-0.22	0.01165	0.0949	45,880	11.64	11.09
3	33728	-0.15	0.01052	0.0959	47,040	--	10.92
3	33728	-0.185	0.01114	0.0957	49,740	10.30	10.77
3	33728	-0.22	0.008237	0.0940	50,880	12.67	10.56

An L^2 norm analysis was done for these results in order to find the convergence of the post-shock solutions. The convergence rates for the post-shock density, temperature, and shock angle are $N^{-0.46}$, $N^{-0.9}$, and $N^{-0.98}$, respectively. At low resolution, the shock temperature is ~27% less than the exact solution, while in the shock layer, the density spread is from -27% to +15% of the exact solution. The shock angle is as much as 30% lower than the exact solution. Improvement for the temperature is seen as the particle

number increases to 33,728, in which all of the temperature measurements were within 10% of the exact solution. Density was found to be consistently higher in all cases, ranging from as high as 53% to as low as 14% of the exact solution. The Mach number was within 10% at all measurements. The variation in density is consistent with variation in line integrated interferometry comparisons with experimental data in early six jet conical simulations [94], whereas Mach number from simulations has been found to fall within the scatter of the data [92]. The discrepancy in density and slight underprediction in temperature for the high-resolution case suggests that the artificial viscosity is not decelerating the particles sufficiently and needs to be explored further. As with the Gresho vortex test case, a Balsara switch or other means of screening shear while properly decelerating particles to prevent interpenetration beyond the interparticle spacing h is a challenge to be explored in future work.

5.7 Taylor-Green Vortex

The Taylor-Green vortex is an incompressible, viscous, time-dependent decaying vortex that has an exact closed-form solution. The problem consists of a cubical volume of fluid with an initially smooth vorticity distribution. As time progresses, the vortices interact until they break down into turbulence, which dissipates the energy in the fluid and eventually brings it to rest. This problem has been used to study energy dissipation, vortex dynamics, and turbulent decay [142, 143]. The problem has been used in the development of other SPH codes that have incorporated viscosity to assess the accuracy of simulating viscous effects [144, 145].

The velocity field of the Taylor-Green vortex is given by

$$v_x = \sin x \cos y \, F(t) \tag{5.22}$$

$$v_y = -\cos x \sin y \, F(t) \tag{5.23}$$

in

which

$$F(t) = e^{-2\nu t} \tag{5.24}$$

The pressure is given by

$$p = \frac{\rho}{4}(\cos(2x) + \cos(2y))F^2(t) \tag{5.25}$$

An example problem that was investigated for this study had a dynamic viscosity of 2 Pa-s, a density of 50 kg/m^3, and was simulated for a total of five seconds. Figure 5.16 shows the velocity vectors of this vortex at 0 s and 5 s. The pressure contour at both 0 s and 5 s are shown in Figure 5.17. In this figure, it can be seen that after five seconds have passed, the velocity of the vortex has decayed dramatically and lead to a significant decrease in the vortex pressure.

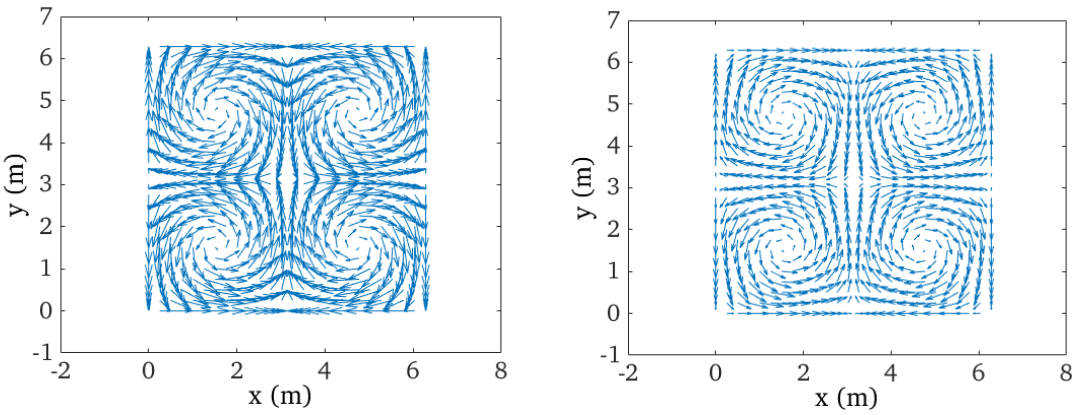

a) b)

Figure 5.16. Taylor-Green Vortex velocity vectors at a) 0 s and b) 5 s.

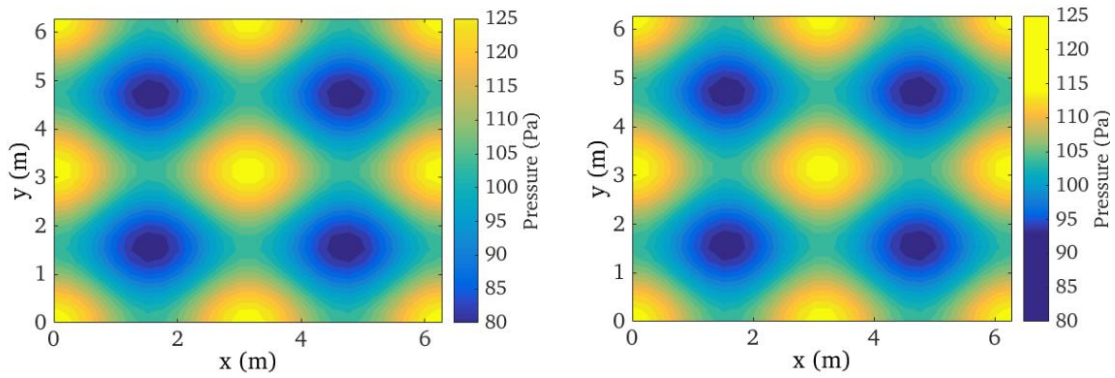

a) b)

Figure 5.17. Taylor-Green Vortex pressure contour at a) 0 s and b) 5 s.

After a sufficient number of simulations were conducted, an L^2 norm analysis of the temperature and x/y velocity components was performed, with the results shown in Figure 5.18a and b. The convergence rates for the Taylor-Green temperature, v_x, and v_y are $N^{-0.1}$, $N^{-0.15}$, and $N^{-0.11}$, respectively. This again is consistent with the order of consistency reported by other SPH codes in the literature [97], and as can be seen the results

are well within 10% accuracy for temperature and v_x, while v_y are within 12% of the exact solution.

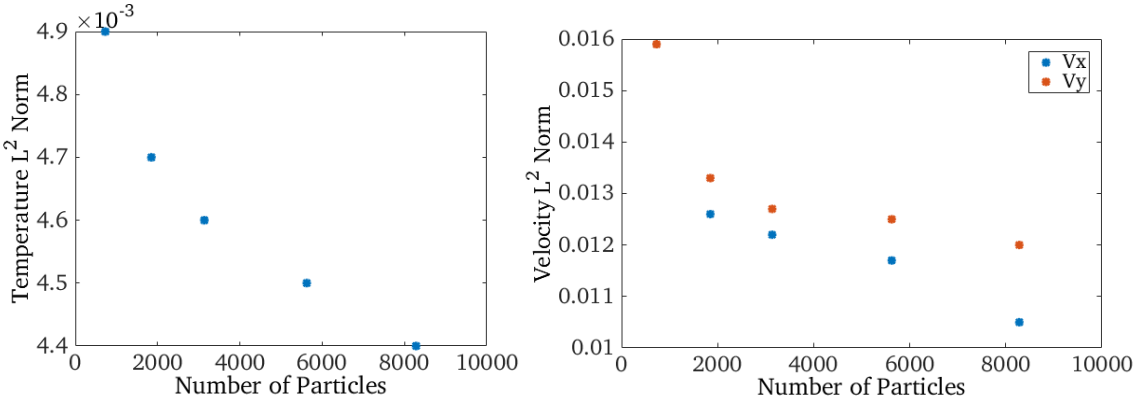

a) b)

Figure 5.18. L^2 norm for Taylor-Green a) temperature and b) velocity.

5.8 Fusion Yield

The final test case simulated a static spherical target of deuterium-tritium with a constant temperature. The spherical geometry was created using an algorithm that regularly places points such that their distance in two orthogonal directions is always the same locally. This regular distribution is achieved by using circles of latitude at constant intervals and setting points at these intervals such that the product of the interval and the point distance is equal to the average area per point [146]. The spherical geometry generated in SPFMax is shown in Figure 5.19

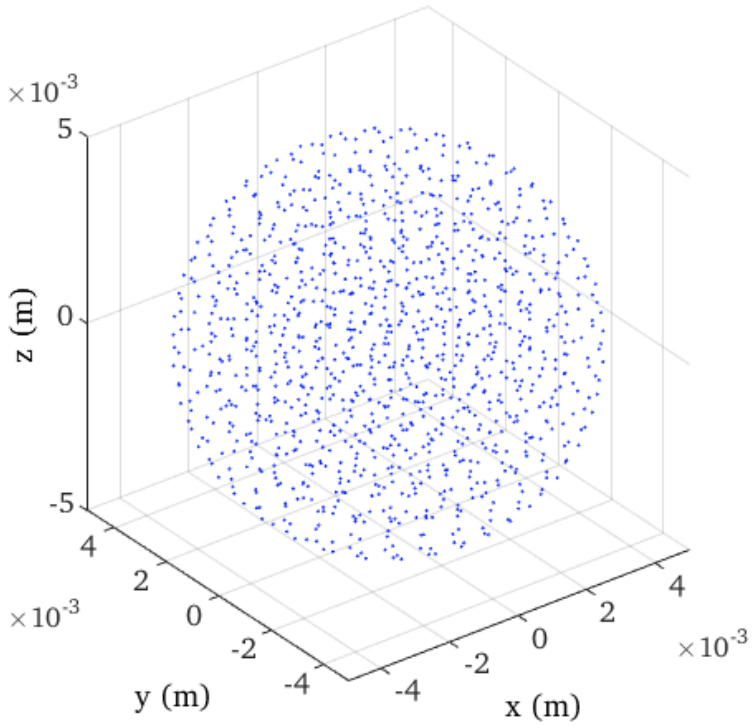

Figure 5.19. Initial fusion target configuration.

The sphere is simulated to be a 50/50 mixture of deuterium-tritium with a density of 1 g/cm^3 and a temperature of 14 keV, conditions necessary for fusion ignition. The SPFMax results were compared to differential equations for fusion yield, given by Equations 5.26 and 5.27.

The fusion reaction rate is given by

$$\frac{dN_{fus}}{dt} = \langle \sigma v \rangle_{DT} n_D n_T V \tag{5.26}$$

The change in the number of deuterium and tritium atoms is given by

$$\frac{dn_D}{dt} = \frac{dn_T}{dt} = -\langle \sigma v \rangle_{DT} n_D n_T \tag{5.27}$$

These equations are solved using the MATLAB ode45 function. A comparison between the fusion energy and neutron yield provided by SPFMax and the ode45 solver are shown in Figure 5.20 and Figure 5.21, respectively

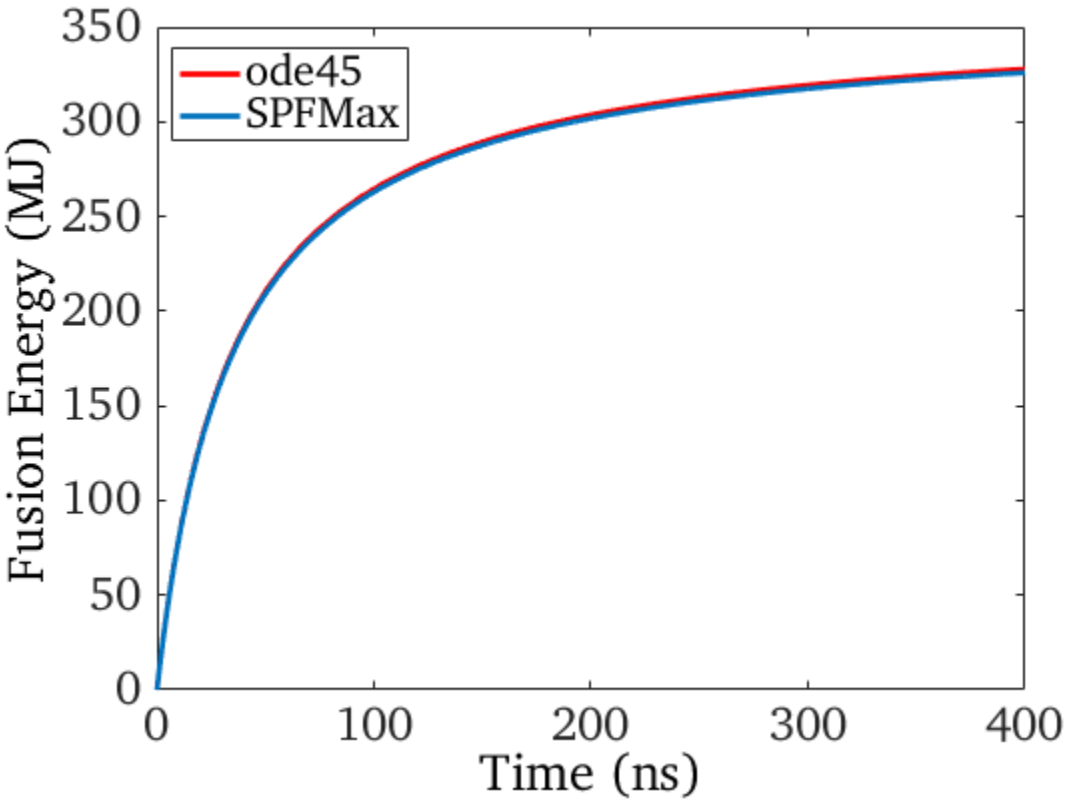

Figure 5.20. Fusion energy yield of SPFMax and ode45.

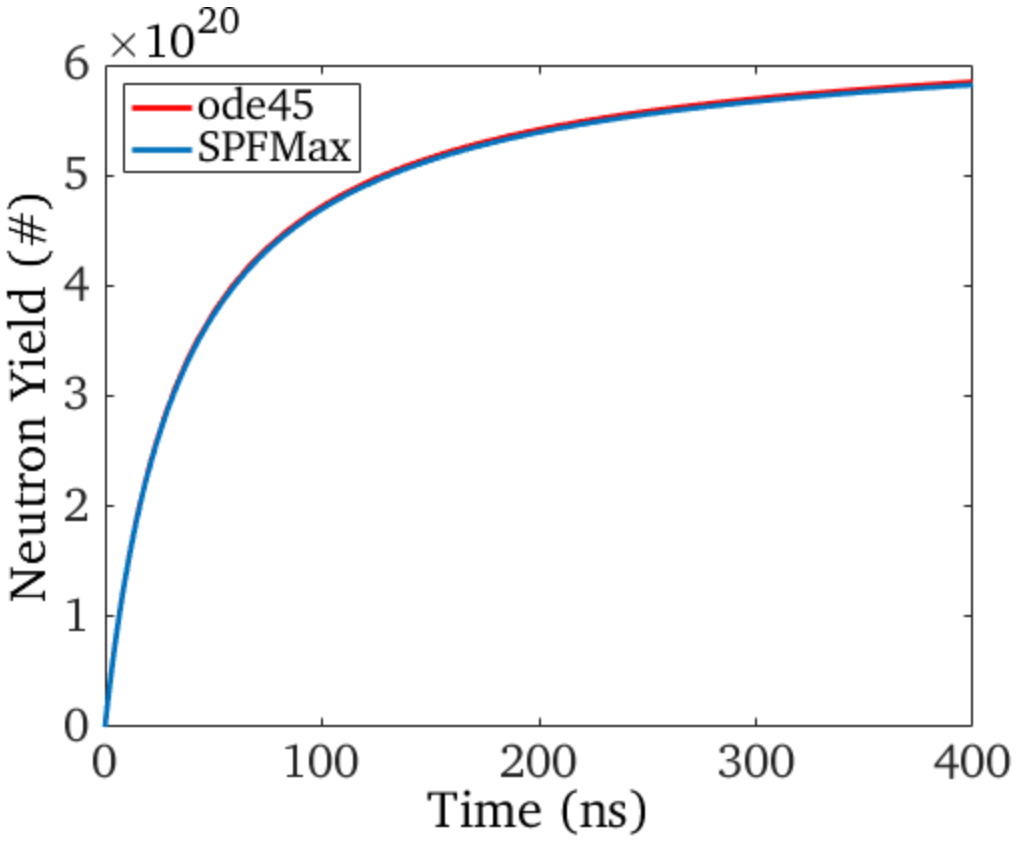

Figure 5.21. Neutron yield of SPFMax and ode45.

The results are in very close agreement and verify the code's accuracy in simulating fusion yield and burnup. This capability enables one to use SPFMax for problems in which fusion yield and fractional burnup are significant.

It was necessary to conduct a self-convergence test in order to verify that SPFMax can provide sufficient resolution to simulate problems pertinent to PJMIF. Increasing the number of particles in the simulation results in different yield values, which converge to the correct solution as resolution increases. The relative norm in the resulting fusion yield can be defined as

$$y_n = \frac{|y_i - y_f|}{y_f} \tag{5.28}$$

with y_f being the fusion yield for the case that has the highest particle resolution.

Simulations were run with particle numbers ranging from 1,000 to 36,000. The corresponding relative norm is shown in Figure 5.22

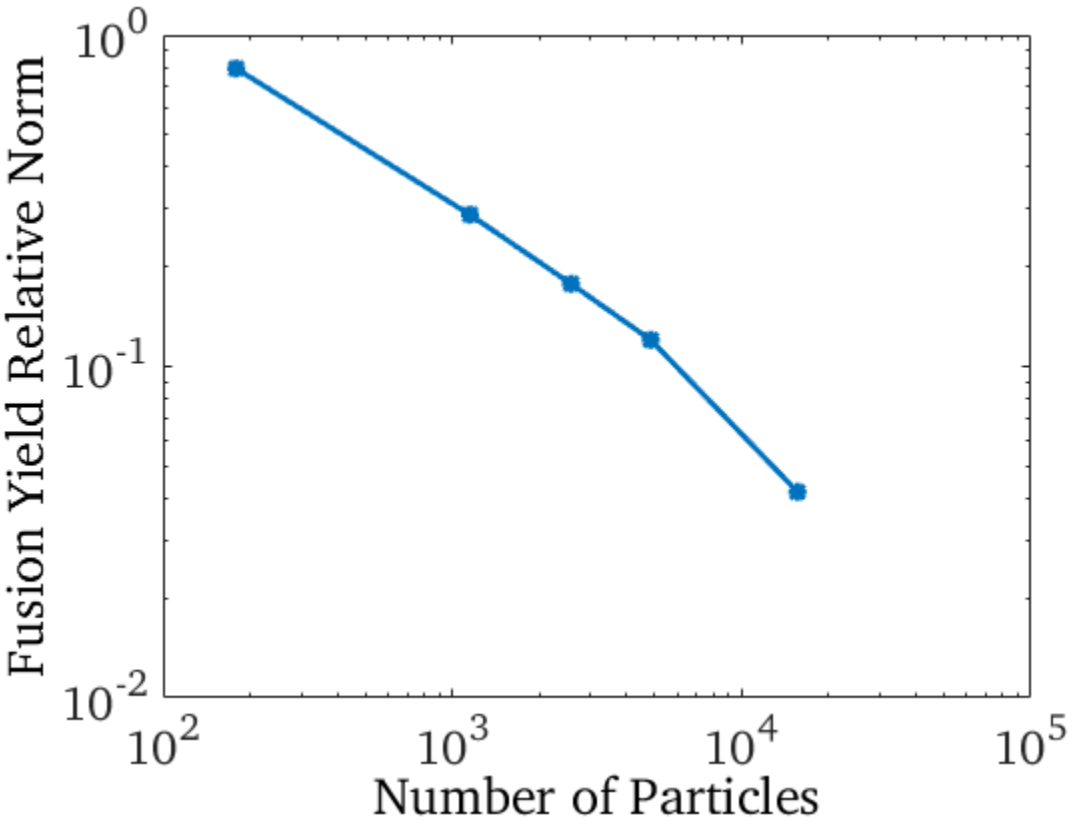

Figure 5.22. Loglog plot of fusion yield self-convergence.

This figure shows the relative norm decreasing by about an order of magnitude with a corresponding increase in particle number. The simulation that uses 4,000 particles

provides a fusion yield that is only 10% different from a simulation that uses 36,000 particles.

The first step in conducting additional simulations was to determine what parameter space offers ignition conditions for PJMIF through constructing Lindl-Widner diagrams. This procedure is detailed in the following chapter.

CHAPTER 6

FUSION POWER BALANCE

6.1 Introduction

Lindl-Widner diagrams are simplified implosion and yield models that were developed to study the parameter space for plasma density and temperature over which fuel capsules may ignite in inertial confinement fusion [147]. This was later modified to examine the parameter space for areal density and temperature [20, 148].

Much of the research with Lindl-Widner diagrams has been conducted for inertial confinement fusion. However, studies have been conducted to construct Lindl-Widner diagrams that incorporate magnetic fields, making it possible to explore the parameter space of PJMIF [149].

The power balance used to produce these diagrams is given by

$$\frac{dE}{dt} = P\frac{dV}{dt} + P_F - P_B - P_C - A\kappa\nabla T \tag{6.1}$$

The fusion power is given by

$$P_F = \frac{dN_{fus}}{dt}(E_\alpha f_\alpha + E_n f_n) \tag{6.2}$$

6.2 Alpha Particle Energy Deposition

The model used to construct the Lindl-Widner diagrams utilizes approximate expressions to characterize the slowing of alpha particles and neutrons in a fusion fuel plasma. The slowing of alpha particles is caused primarily by small-angle collisions with electrons. The decrease in the velocity of the alpha particles is given by

$$\frac{dv_\alpha}{dt} = -\frac{v_\alpha}{2t_{\alpha e}} \tag{6.3}$$

The characteristic time in picoseconds for the alpha particle energy deposition is given by

$$t_{\alpha e} \simeq \frac{42T_e^{3/2}}{\rho \ln \Lambda_{\alpha e}} \tag{6.4}$$

The collision time between ions and electrons is given by

$$\tau_e = \frac{3\sqrt{m_e}(k_B T_e)^{3/2}}{4\sqrt{2\pi} n_i Z_i^2 q^4 \ln \Lambda_e} \tag{6.5}$$

The collision time between ions is given by

$$\tau_i = \frac{3\sqrt{m_i}(k_B T_i)^{3/2}}{4\sqrt{2\pi} n_i Z_i^2 q^4 \ln \Lambda_i} \tag{6.6}$$

The timescale needed for energy exchange to occur between the ions and electrons takes longer than the timescales needed for the electrons and ions to approach thermal equilibrium within their subsystems. On average, an electron must collide with ions $m_i/(2m_e)$ times before the electron's energy is transferred a single time [4]. The equilibration time is then given by

$$\tau_{ei} = \frac{m_i}{2m_e}\tau_e = 9.9 \times 10^{-9}\frac{AT_e^{3/2}}{n_i Z_i^2 \ln \Lambda_e} \tag{6.7}$$

The alpha particle energy deposition time and the equilibration time are very similar to each other and are smaller than the time needed for ignition to occur in fusion targets [4]. Therefore, to construct the Lindl-Widner diagrams, it is assumed that the ions and electrons have the same temperature and that the alpha particles transfer their energy instantaneously to the electrons.

The range of a 3.5 MeV alpha particle produced in a D-T reaction can be obtained as [4]

$$l_\alpha = \int_0^\infty v_\alpha dt = 2v_{\alpha 0}t_{\alpha e} \tag{6.8}$$

The fraction of the alpha particle energy that is deposited in the hot spot is given by [4]

$$f_\alpha = \begin{cases} \frac{3}{2}\tau_\alpha - \frac{4}{5}\tau_\alpha^2, & \tau_\alpha \le 1/2 \\ 1 - \frac{1}{4\tau_\alpha} + \frac{1}{160\tau_\alpha^3}, & \tau_\alpha \ge 1/2 \end{cases} \tag{6.9}$$

in which

$$\tau_\alpha = \frac{r}{l_\alpha}\left(1 + \frac{r}{r_L}\right) \tag{6.10}$$

If the hot spot is surrounded by a layer of colder fusion fuel, alpha particles created within the hot spot can be slowed dramatically, heating the colder fuel and drive the propagation of a fusion burn wave. A strong magnetic field embedded within the target significantly increases the alpha particle energy deposition fraction, as will be shown in the following sections.

6.3 Neutron Energy Deposition

Neutrons generated in fusion reactions deposit their energy to the plasma primarily through elastic collisions with nuclei. The average fraction of the neutron's energy lost from collision with a nucleus that has a mass number of A is given by [4]

$$f_{en} = \frac{2A}{(A+1)^2} \tag{6.11}$$

The average mean free path of the neutron is

$$l_n = \frac{1}{\sigma n} \tag{6.12}$$

The value of ρl_n is significantly greater than the areal density of the plasma's hot spot field. In addition, neutrons are unaffected by a magnetic field that may be embedded within the target. For these reasons, neutrons deposit very little of their energy into the hot spot. However, ρl_n is comparable to the areal density of the entire plasma. Consequently, the neutrons do deposit a fraction of their energy into the plasma, which is given by

$$f_n = \frac{\rho R}{\rho R + H_n} \tag{6.13}$$

in which H_n=20 g/cm^2.

The neutron fractional power deposition is much smaller than the alpha particle fractional deposition. Consequently, the alpha particles are primarily responsible for the heating of the fusion fuel and burn wave propagation.

6.4 Lindl-Widner Diagrams

The primary objective of creating Lindl-Widner diagrams was to provide a guideline for fusion target conditions to use in SPFMax simulations. In the first set of cases examined, the fusion fuel target has a radius ranging from 10 cm to 1 mm, a number density ranging from 10^{23} to 10^{36} m^{-3}, no magnetic field, and no implosion velocity. The Lindl-Widner diagram for these cases is presented in Figure 6.1. The implosion velocity was excluded because during the compression phase of PJMIF, the compressional work dominates the power balance given in Equation 6.1. Furthermore, the objective of conducting simulations with SPFMax is to study fusion yield once ignition conditions have been reached in the target. This would occur at peak compression when no kinetic energy remains in the target or the liner.

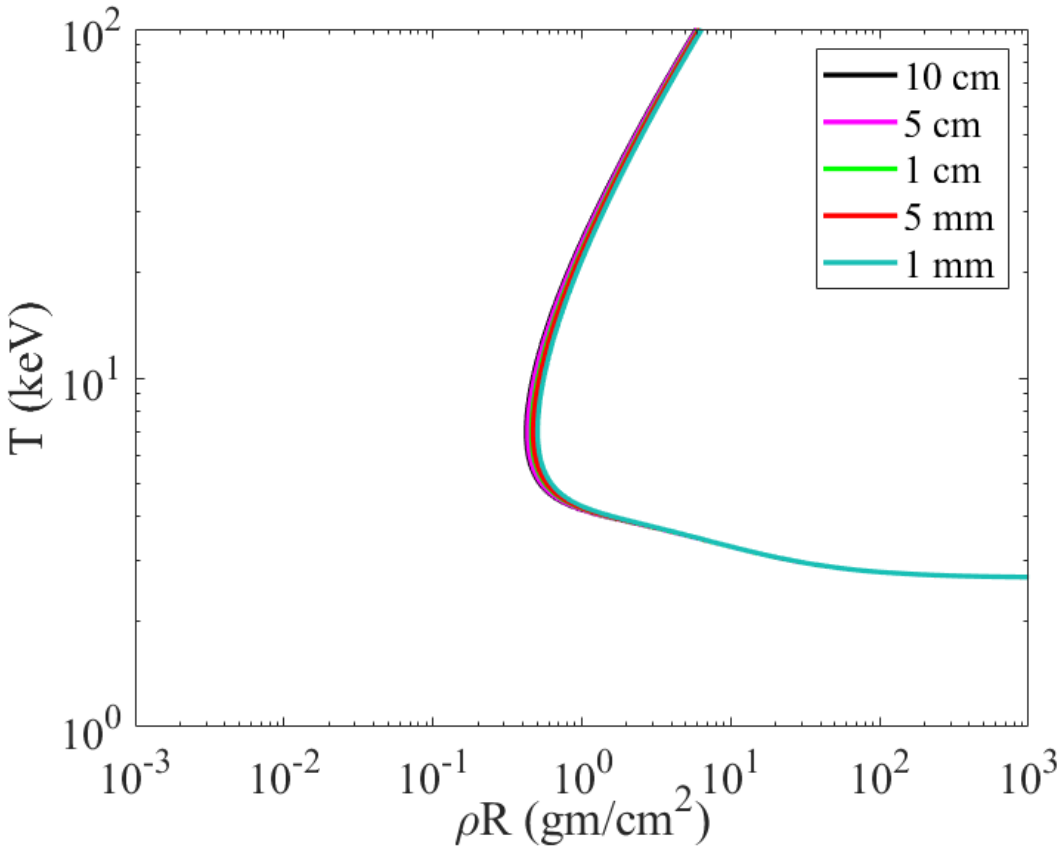

Figure 6.1. Lindl-Widner diagram for varying radii and no magnetic field.

In this diagram, the region to the right of the curves represents the paramater space for the areal density and temperature in which fusion power exceeds power losses, while the region to the left of the curve represents the parameter space in which power losses exceed fusion power and the target quenches. Increasing the target radius corresponds to a small increase in the area for fusion ignition due to an increase in the mass of the fusion fuel. But in order to dramatically increase the region for fusion ignition, a magnetic field must be embedded in the target, as is shown in Figure 6.2. This figure presents a Lindl-Widner diagram for a target with a 1 mm radius and varying magnetic field intensities.

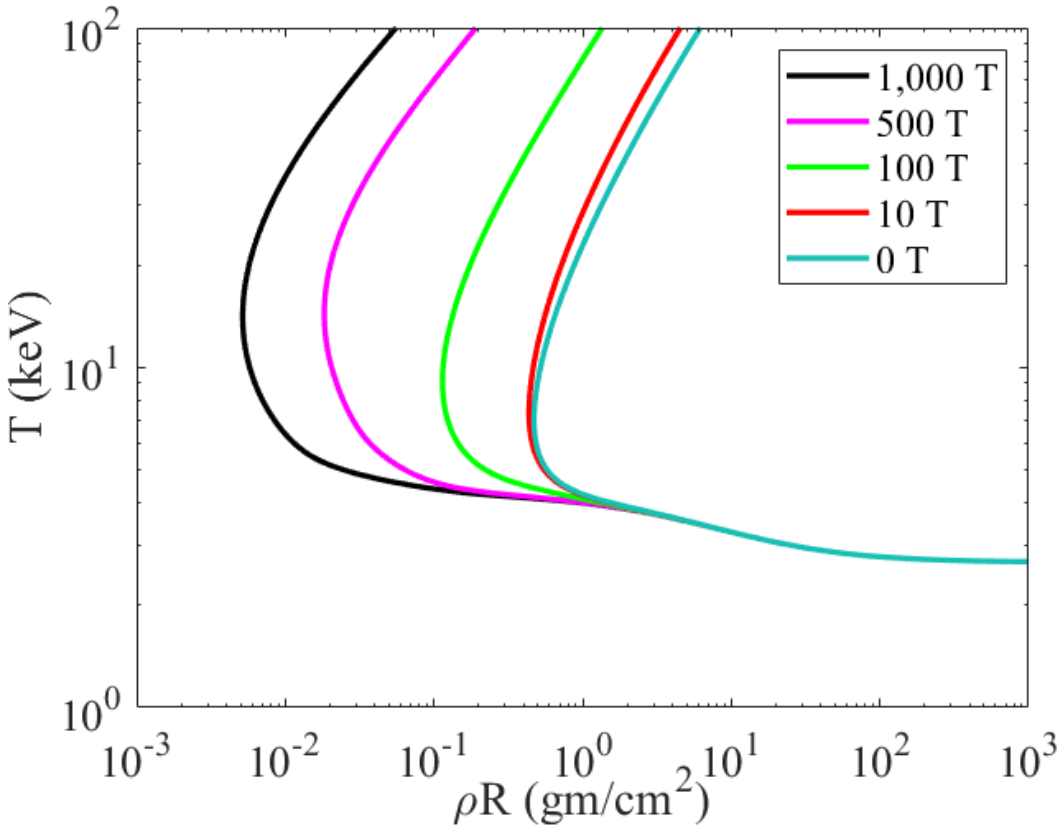

Figure 6.2. Lindl-Widner diagram for 1 mm radius target and varying magnetic fields.

Larger magnetic fields are seen to dramatically increase the ignition region for this target by enhancing the alpha particle energy deposition fraction. However, a magnetic field also leads to cyclotron radiation, and this radiation becomes the dominant energy loss mechanism at low densities and temperatures. This is due to the fact that alpha particle energy deposition is limited for cold, low density plasmas. In addition, cyclotron radiation scales linearly with density and temperature while also scaling as a function of the square of the magnetic field.

A stronger magnetic field reduces the gyroradius of the alpha particle, which increases the dwell time of the alpha particle inside of the target. The ratio of the target radius to the ion gyroradius must be much greater than 1 in order to significantly enhance the dwell time. The ion gyroradius and the ratio of the target radius to the ion gyroradius are shown in Figure 6.3 and Figure 6.4, respectively.

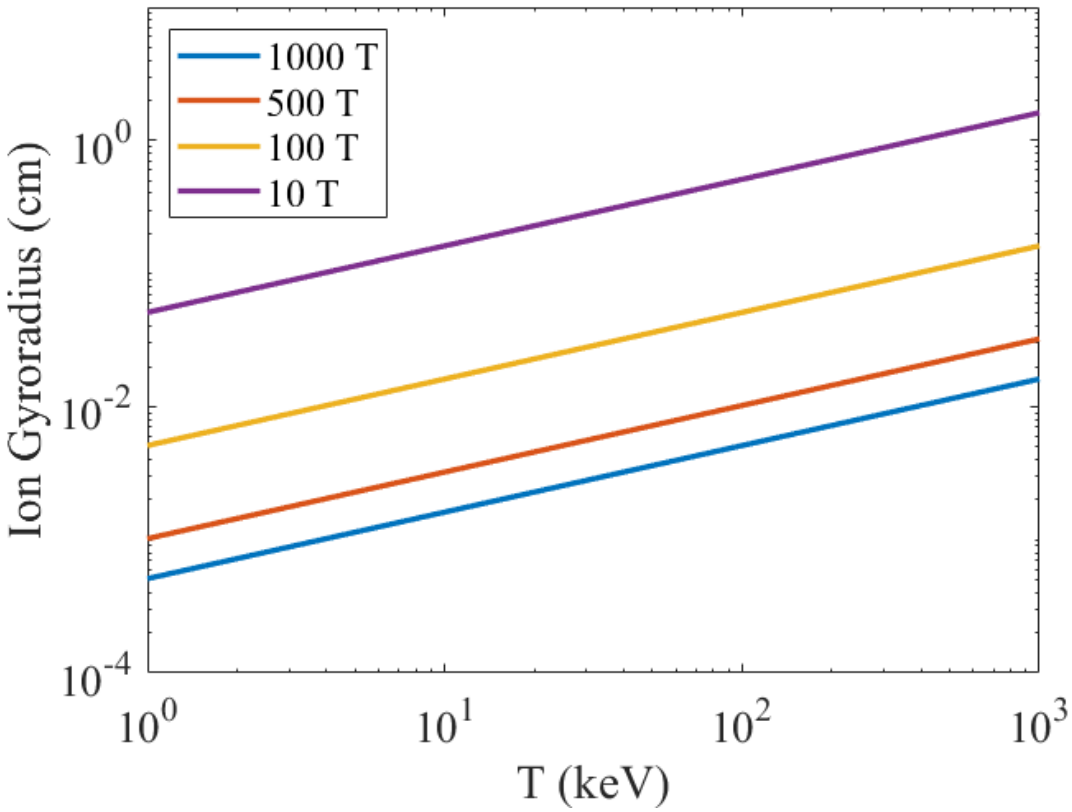

Figure 6.3. Ion gyroradius for 1 mm target for different magnetic field intensities and plasma temperatures.

In Figure 6.4, it can be seen that the ratio of the target radius to the ion gyroradius is greatest when a 1,000 T magnetic field is present. A Lindl-Widner diagram was then

constructed for each of the previously examined target radii with a 1,000 T magnetic field embedded in the targets. The results of this are shown in Figure 6.5.

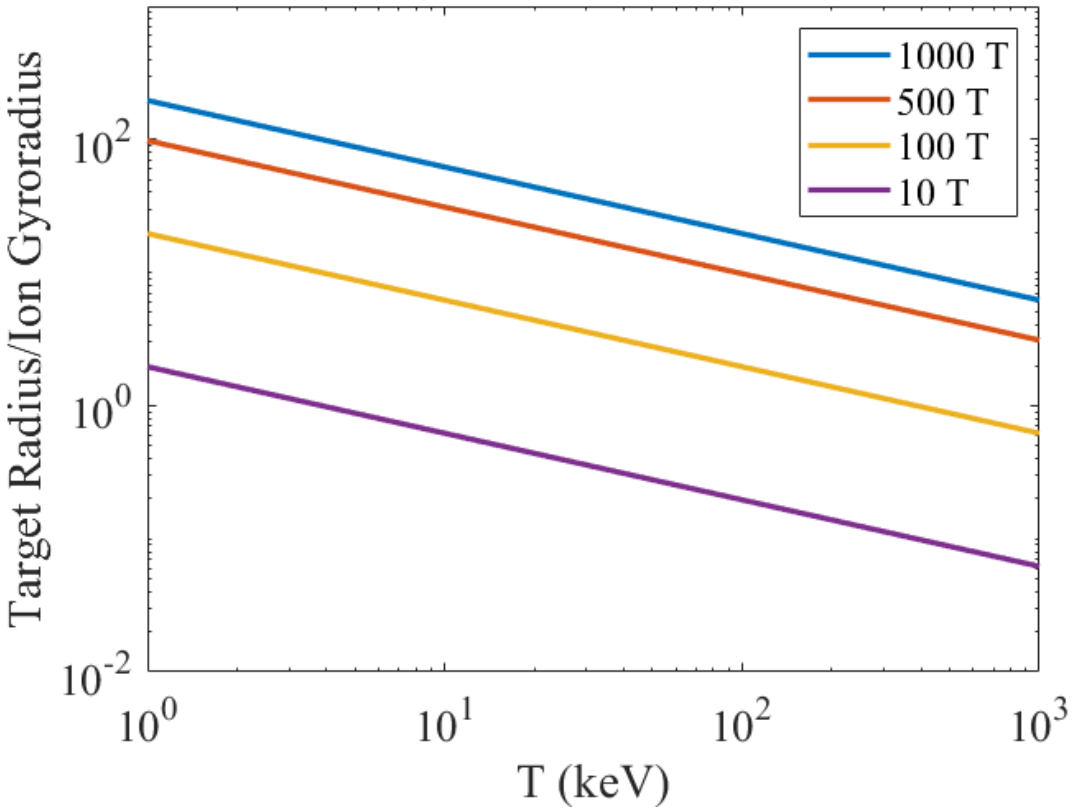

Figure 6.4. Ratio of target radius to ion gyroradius for 1 mm target for different magnetic field intensities and plasma temperatures.

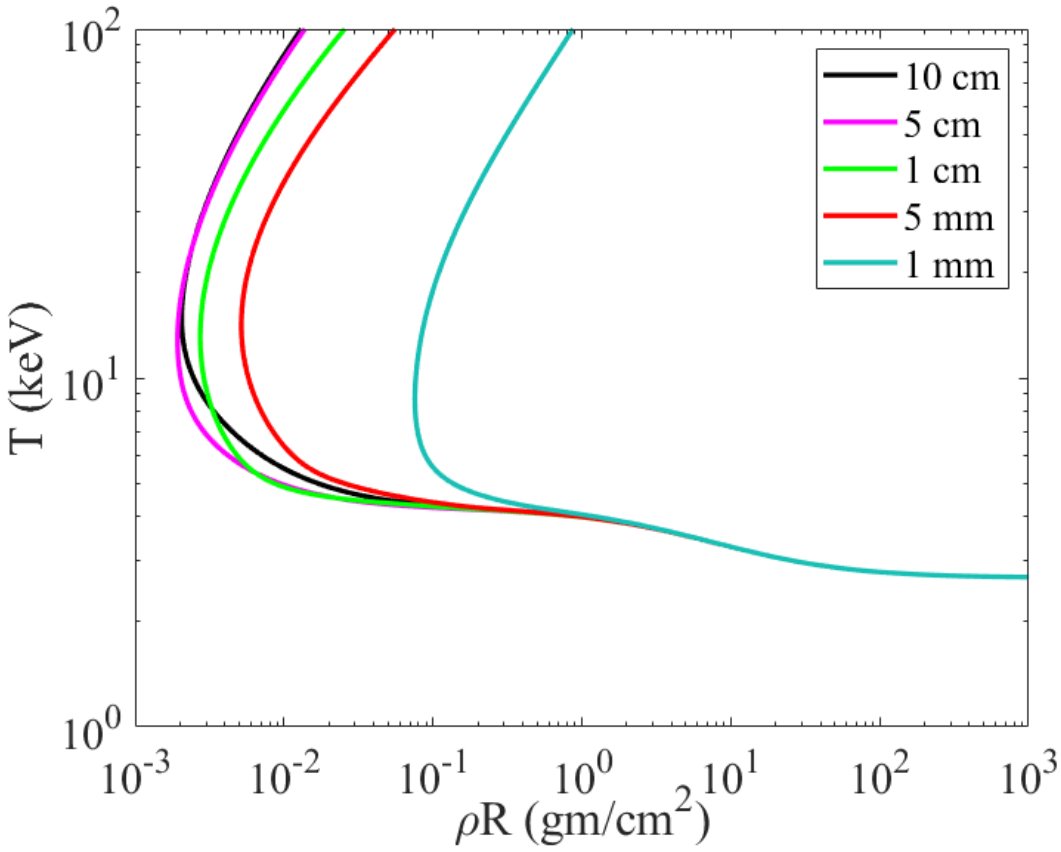

Figure 6.5. Lindl-Widner diagram for varying radii and 1,000 T magnetic field.

At high areal densities, the lower bounds of the contours for the different targets are nearly identical. At lower areal densities, differences are seen in the contours' lower bounds. This is due to Bremsstrahlung radiation scaling with the square of the plasma density while cyclotron radiation scales linearly with density, causing cyclotron radiation to dominate at low areal densities and Bremsstrahlung radiation dominating at high areal densities. Cyclotron radiation also scales linearly with temperature while Bremsstrahlung radiation scales with the square root of temperature.

With these results as a baseline, it was then possible to conduct simulations of fusion fuel targets in SPFMax, which is the subject of the next chapter.

CHAPTER 7

THREE-DIMENSIONAL FUSION SIMULATIONS

7.1 Introduction

The SPFMax simulations begin with a fully compressed and static target of deuterium-tritium. Several simulations were conducted with the target by itself and additional simulations were conducted with the target surrounded by an afterburner, which consists of a layer of colder fusion fuel that surrounds the hot fusion target. Three-dimensional simulations allow for the examination of the effect that non-uniformities on the surface of the target have on the fusion yield. Several simulations were conducted with different non-uniformities and are presented later in this chapter. Demonstrating the capability to simulate these effects is crucial for the investigation of PJMIF in order to determine the viability of this fusion concept. Future studies may investigate non-uniformities and instabilities that arise during the implosion process rather than predefined non-uniformities.

The initial conditions of the target and afterburner for each of the cases are presented in Table 7.1. The baseline case consists of an unmagnetized target of deuterium-tritium. This case is further described in Section 7.2, with subsequent sections grouped according to the parameter that was varied. A magnetized target was then simulated to determine what effect an embedded magnetic field has on the fusion yield. Following this, a case was run with a cold afterburner surrounding the target. The afterburner was simulated with and without a magnetic field in order to assess how the fusion yield is affected by a magnetized afterburner. A high-density afterburner was also simulated. Finally, a number of simulations were conducted with non-uniform targets in which spherical harmonics were used to impose predefined degrees, orders, and amplitudes on the surface of the target. The corresponding change in the fusion yield presented for these non-uniform cases is presented in Section 7.4. The trends observed are compared with related results in the open literature.

Table 7.1. Initial conditions of fusion simulations.

	Target							Afterburner			
Case	r_t (mm)	ρ_t (kg/m^3)	T_t (keV)	B_t (T)	l	m	a	th_a (mm)	ρ_a (kg/m^3)	T_a (keV)	B_a (T)
1	1	1,000	14	0	N/A	N/A	N/A	N/A	N/A	N/A	N/A
2	1	1,000	14	1	N/A	N/A	N/A	N/A	N/A	N/A	N/A
3	1	1,000	14	0	N/A	N/A	N/A	0.4	3,000	0.5	0
4	1	1,000	14	0	N/A	N/A	N/A	0.4	2,000	0.5	0
5	1	1,000	14	1,000	N/A	N/A	N/A	0.4	2,000	0.5	1,000
6	1	1,000	14	1,000	2	1	0.5	N/	N/A	N/A	N/A
7	1	1,000	14	1,000	14	8	0.5	N/A	N/A	N/A	N/A
8	1	1,000	14	1,000	12	7	0.5	N/A	N/A	N/A	N/A
9	1	1,000	14	1,000	2	2	0.5	N/A	N/A	N/A	N/A

10	1	1,000	14	1,000	8	5	0.5	N/A	N/A	N/A	N/A
11	1	1,000	14	1,000	10	6	0.5	N/A	N/A	N/A	N/A
12	1	1,000	14	1,000	0	0	0	0.4	2,000	0.5	1,000
13	1.33	1,000	14	1,000	2	1	0.5	0.545	2,000	0.5	1,000
14	1.3	1,000	14	1,000	10	6	0.5	0.565	2,000	0.5	1,000
15	1.3	1,000	14	1,000	12	7	0.5	0.385	2,000	0.5	1,000
16	1.33	1,000	14	1,000	14	8	0.5	0.565	2,000	0.5	1,000

7.2 Baseline Target Case

The baseline case consists of a target of deuterium-tritium with a radius of 1 mm, an initial temperature of 14 keV, and a density of 1 g/cm^3. The 14 keV temperature was selected because, as shown in Chapter 1, this is the temperature that results in the lowest triple product for the D-T fusion reaction. The radius and density values were obtained from peak compression conditions that were reported in a recent study from Knapp and Kirkpatrick that was discussed in Chapter 3. This study investigated one-dimensional simulations of a xenon liner compression a D-T afterburner and target, and reported significant energy gain [78].

A sequence of 3D scatter plots are shown at times 0, 0.5, 1, and 2 ns are shown in Figure 7.1. The plots are colored with RGB values scaled against mass density and temperature.

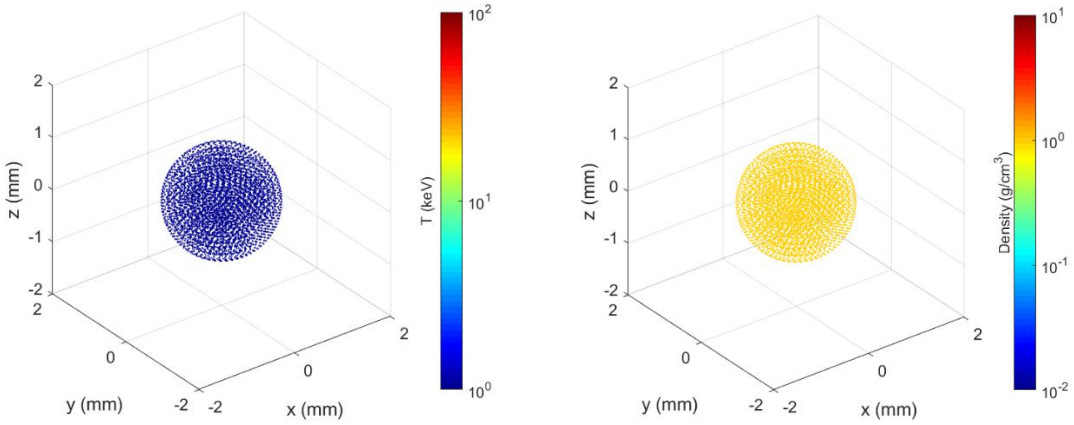
z (mm)
y (mm)
x (mm)
T (keV)
Density (g/cm^3)

a)

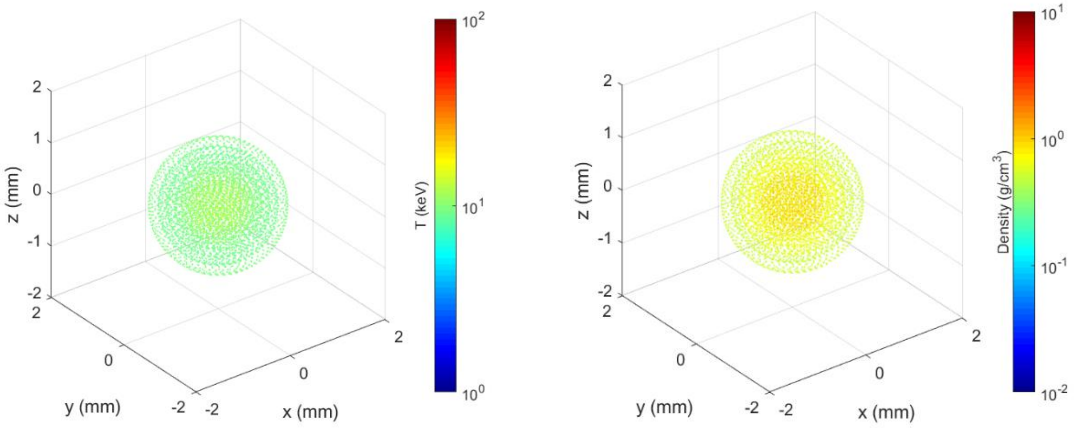
z (mm)
y (mm)
x (mm)
T (keV)
Density (g/cm^3)

b)

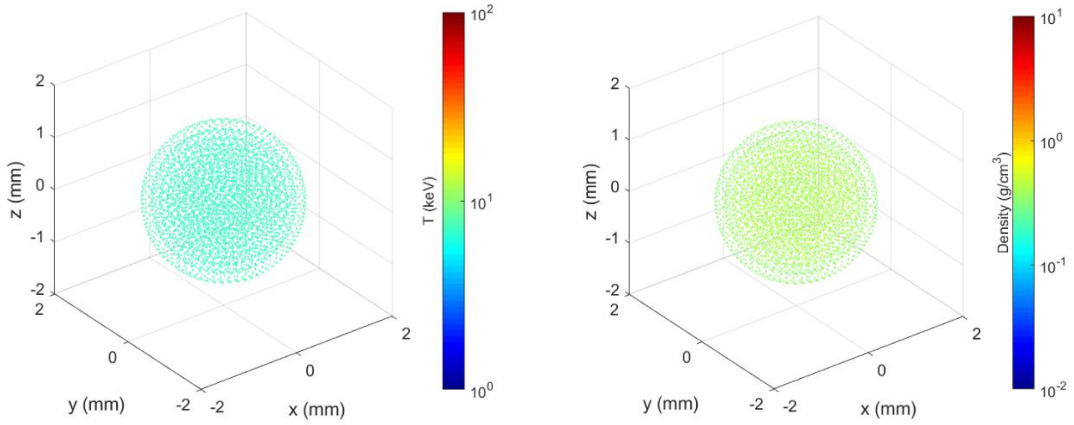
z (mm)
y (mm)
x (mm)
T (keV)
Density (g/cm^3)

c)

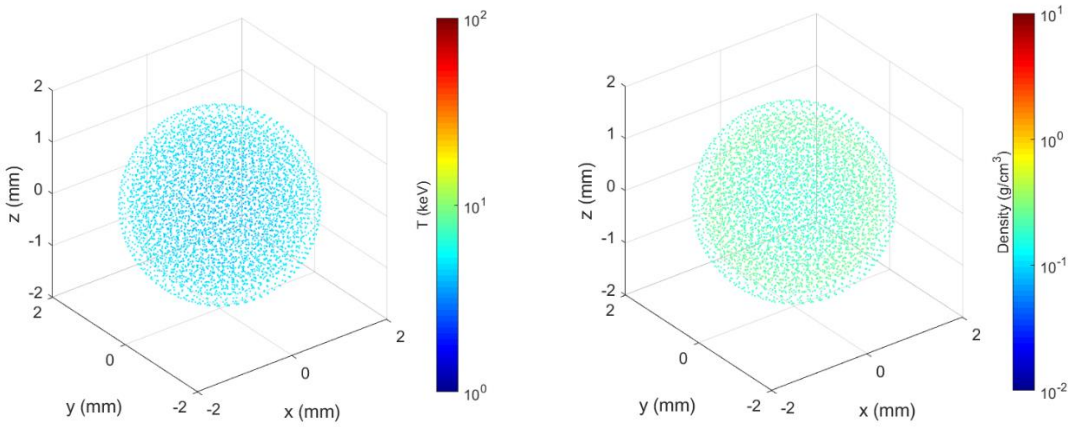

d)

Figure 7.1. Baseline target case temperature (left) and mass density (right) at a) t=0 ns, b) t=0.5 ns, c) t=1 ns, and d) t=2 ns.

By 0.5 ns, the target has expanded to a radius of 1.16 mm with an expansion speed of 350 km/s, which is consistent for a D-T plasma with an initial sound speed of 1,371 km/s. Plots taken at 1 ns and 2 ns show the continued thermal expansion of the target at a rate of 350 km/s, with the temperature and the mass density seen to steadily decrease during the expansion process.

Plots of the fusion power production and power losses resulting from gas expansion and Bremsstrahlung radiation are shown in Figure 7.2. The majority of the power losses are due to the expansion of the target.

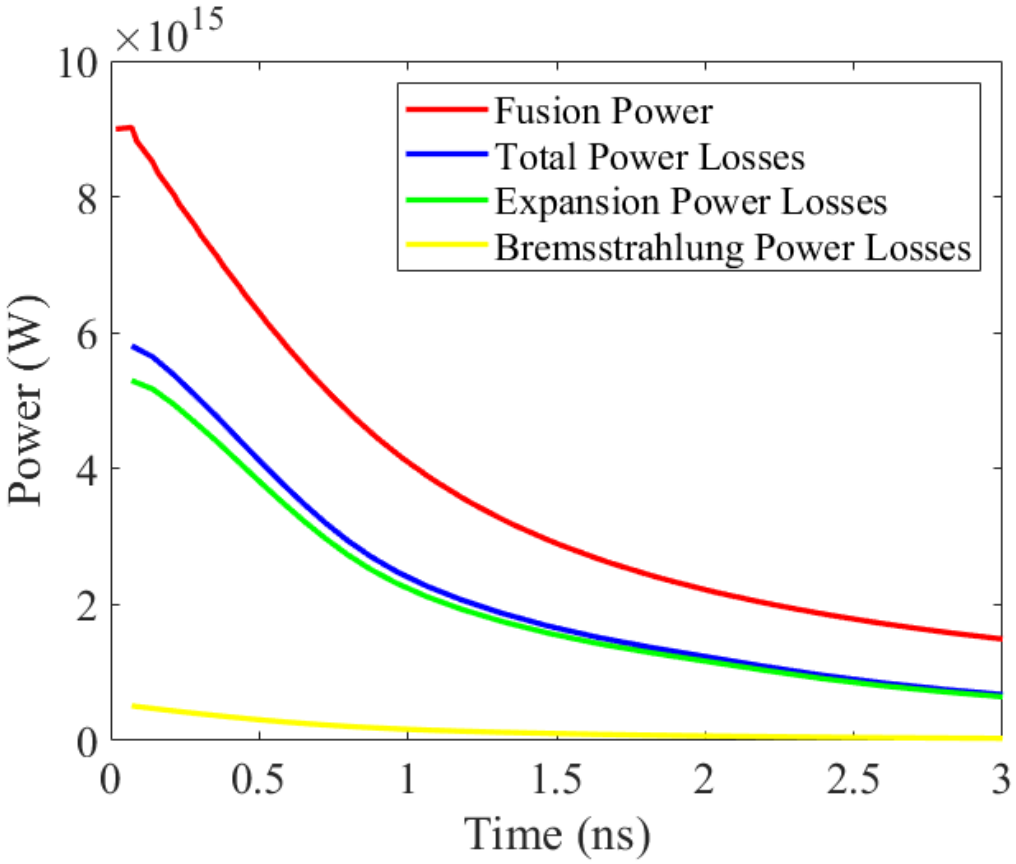

Figure 7.2. Fusion power production and power losses from expansion and Bremsstrahlung radiation.

Plots of the total fusion energy and neutron yield versus time are provided in Figure 7.3. By 2 nanoseconds, the yield has peaked. The fusion energy yield peaks at 4.48 MJ and the neutron yield peaks at 8×10^{18} neutrons, resulting in an energy gain of 0.53.

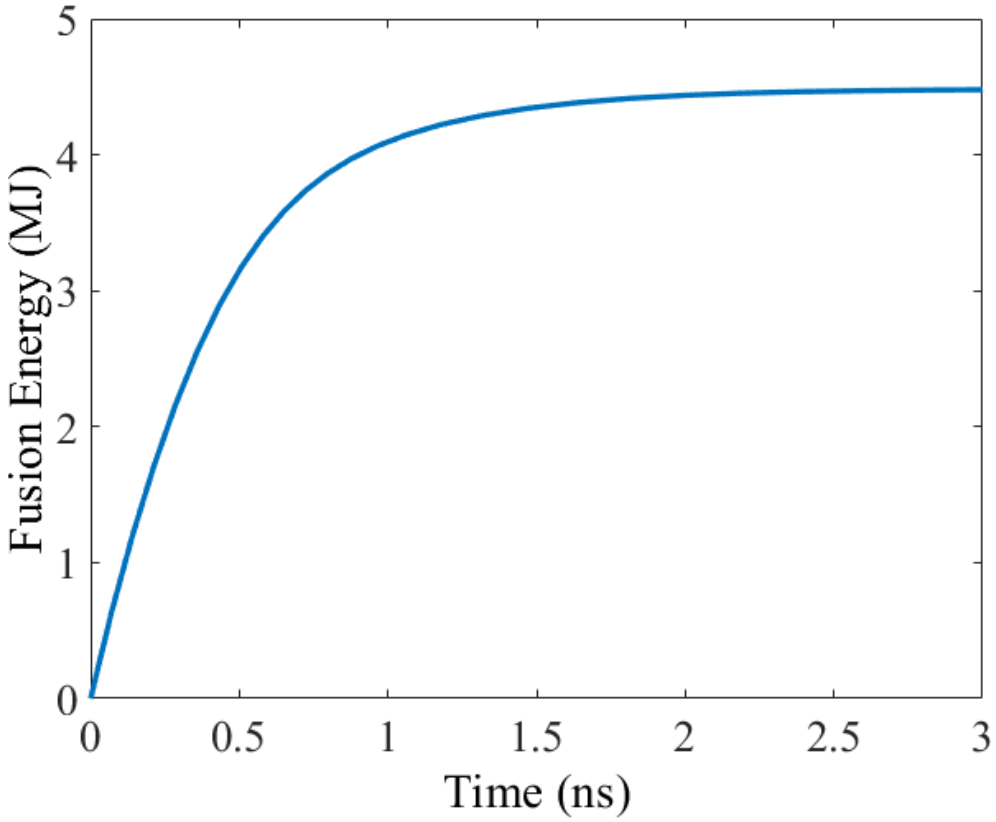

a)

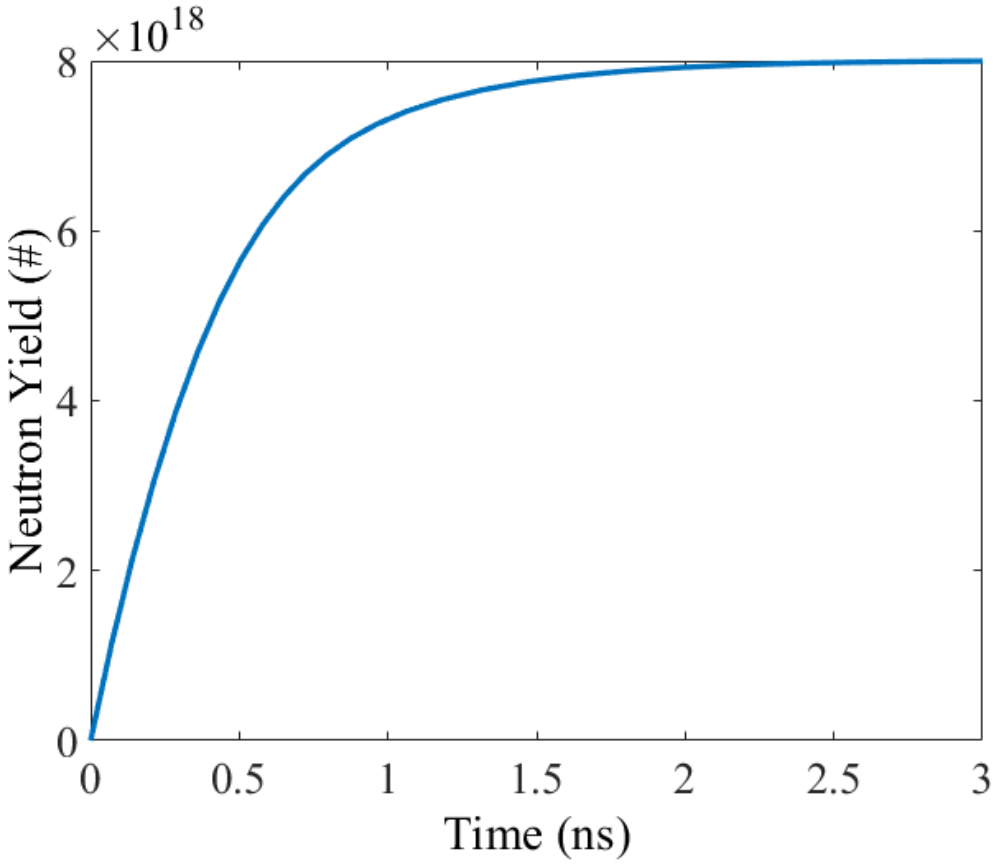

b)

Figure 7.3. a) Total fusion energy yield and b) total neutron yield for baseline target case.

Figure 7.4 shows 2D slices of temperature and mass density at 0.5 ns, 1 ns, and 2 ns. At 0.5 ns, the temperature and density of the target have begun to decrease as the target expands, corresponding to a drop in the yield rate.

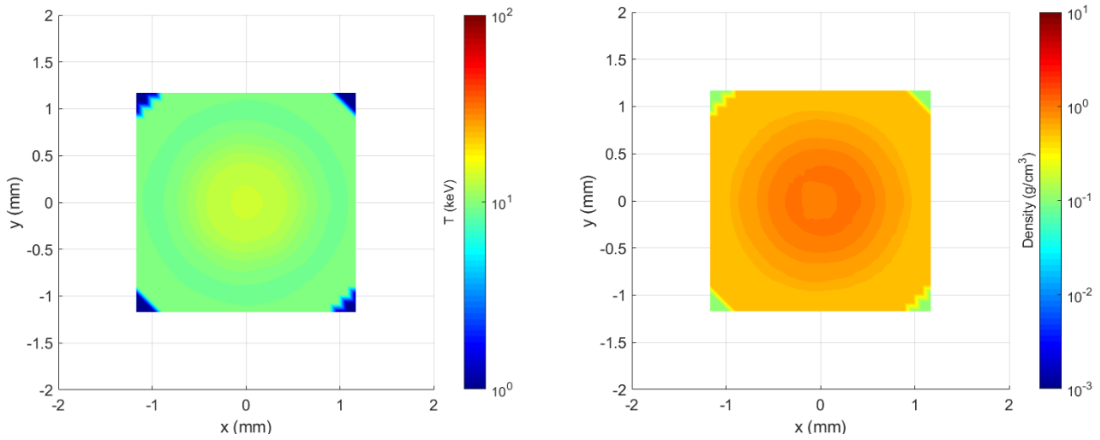

a)

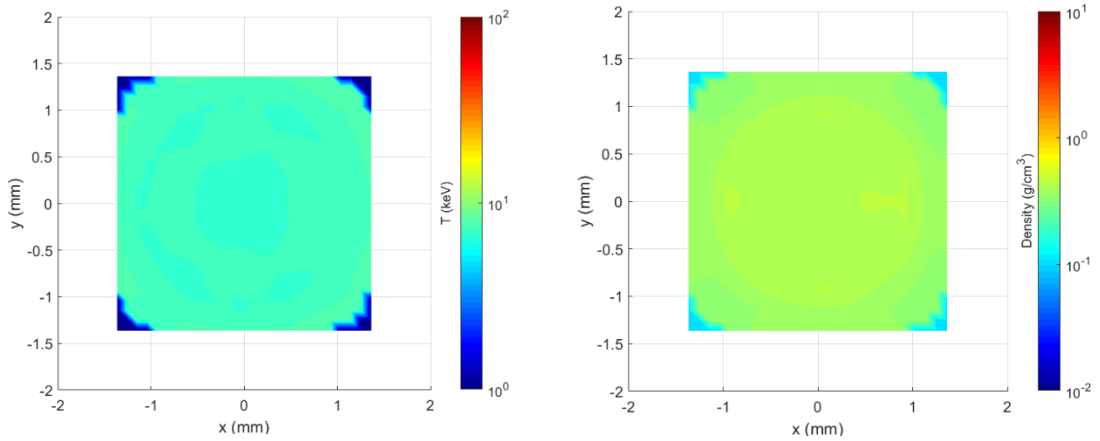

b)

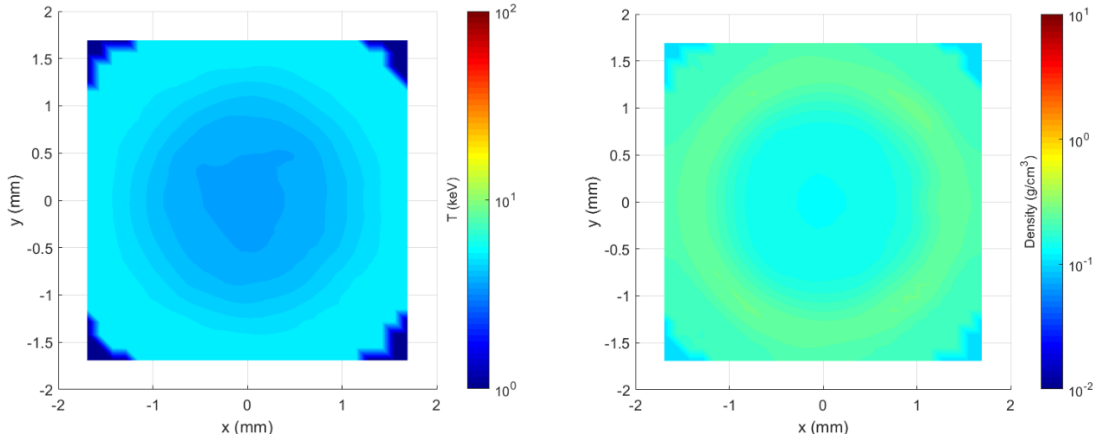

c)

Figure 7.4. 2D slice of temperature (left) and mass density (right) at a) t=0 ns, b) t=0.5 ns, c) t=1 ns, and d) t=2 ns.

At 1 ns and 2 ns, there is a continued decrease in both the temperature and density throughout the target as a result of the expansion process, with a corresponding decrease in the fusion yield. At 2 ns, the target has expanded to nearly twice its original radius, with both the temperature and density having fallen dramatically and effectively ending fusion reactions.

Line slices of both the temperature and density taken throughout the target at 0, 0.5, 1, and 2 ns are shown in Figure 7.5 and Figure 7.6, respectively. These show a drop in both temperature and density at the outer edges of the target and a reduction in the average temperature and density as the target expands.

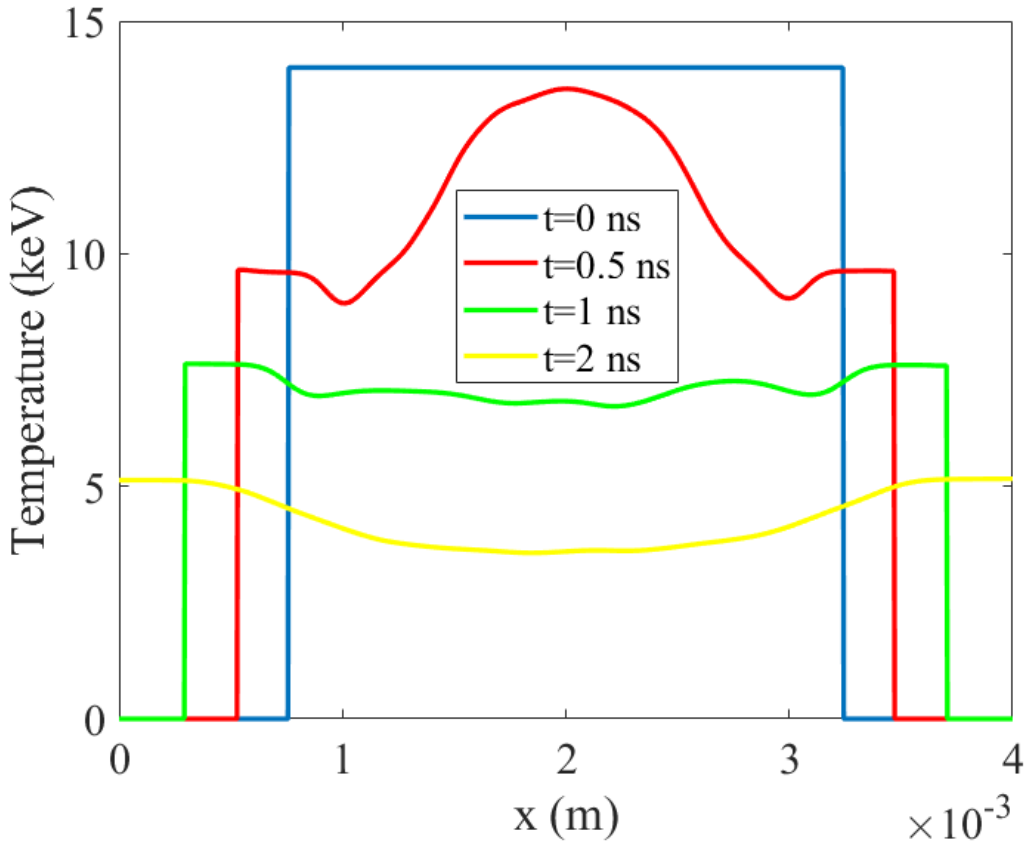

Figure 7.5. Temperature line slices through target taken at 0, 0.5, 1, and 2 ns.

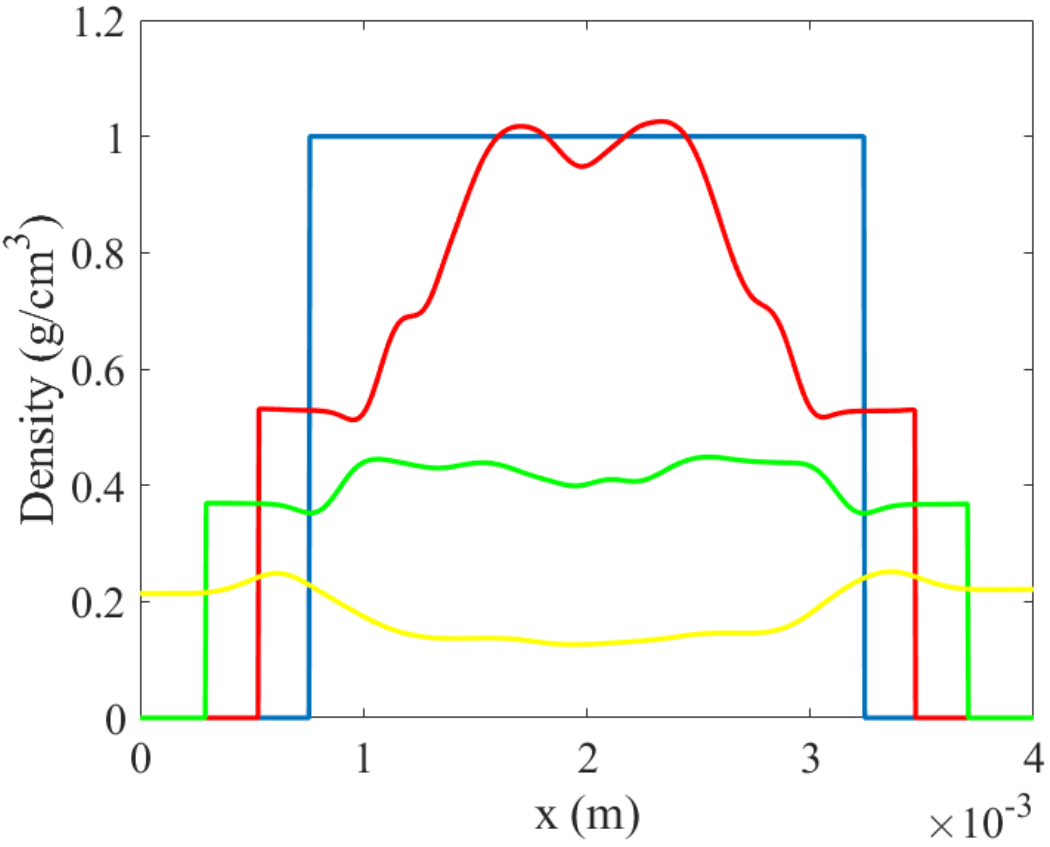

Figure 7.6. Density line slices through target taken at 0, 0.5, 1, and 2 ns.

The initial conditions and fusion yield for this case are summarized in Table 7.2. As shown in Chapter 6, an unmagnetized target with a radius of 1 mm and a temperature of 14 keV must have an areal-density of at least 0.7 g/cm^2 for net power generation. Since the ρ-R for this case is only 0.1 g/cm^2, the thermal conduction and Bremsstrahlung radiation quench the target, allowing only for batch burn to occur with a gain less than unity.

Table 7.2. Initial conditions and fusion yield for baseline case.

r (mm)	ρ (kg/m^3)	T (keV)	B (T)	E_{th} (MJ)	Neutron Yield (#)	Fusion Energy Yield (MJ)	Gain
1	1,000	14	0	8.52	8.01×10^{18}	4.5	0.526

7.2.1 Magnetized Target

As discussed in Chapter 6, greater stopping power of the alpha particles can be achieved if a magnetic field is embedded in the target. To investigate this with SPFMax, the baseline target was simulated again, this time with an embedded 1,000 T magnetic field. This corresponds to a Hall parameter of 0.21 and increases the stopping power by a factor of 27. The model conserves magnetic flux. This study also did not examine different magnetic field topologies, which may cause end losses or non-uniform fusion particle transport.

The fusion and neutron yield for this case are shown in Figure 7.7 and Figure 7.8, respectively. The embedded magnetic field is seen to provide only a small increase in the yield, with the energy peaking at 4.65 MJ and the neutron yield peaking at 8.3×10^{18} neutrons. This minor improvement in yield prompted the investigation of cases that incorporate a cold afterburner layer of fusion fuel that surrounds the target. These cases are presented in the following subsections.

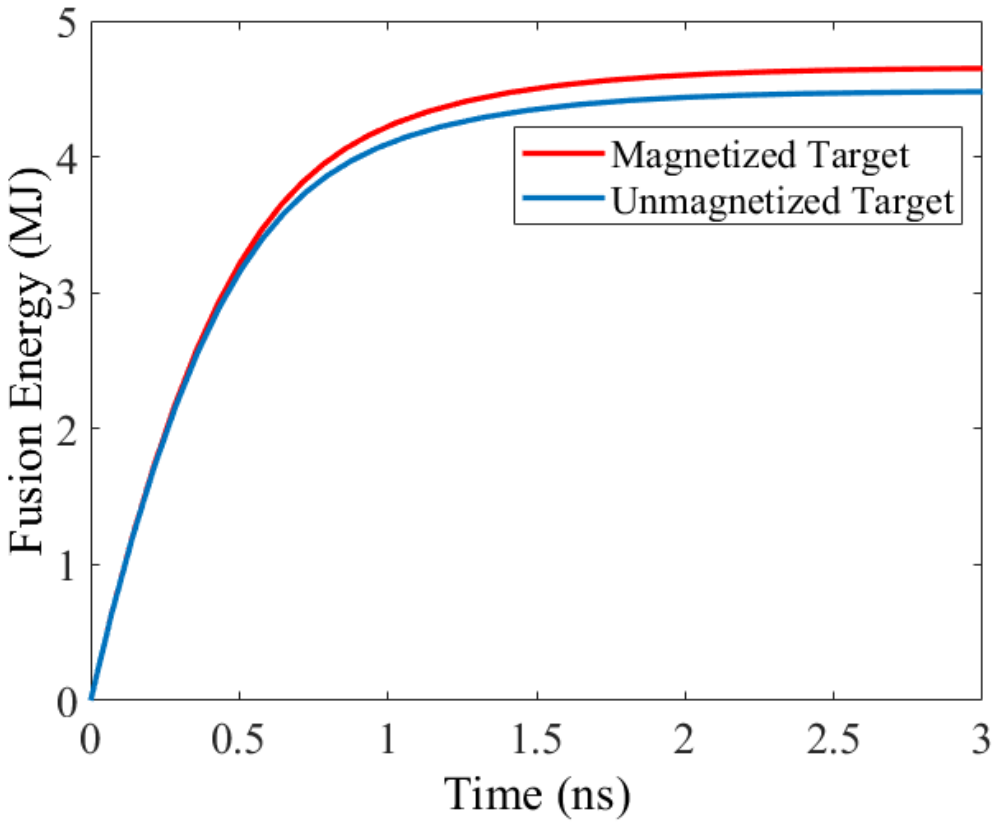

Figure 7.7. Total fusion energy yield for magnetized and unmagnetized target cases.

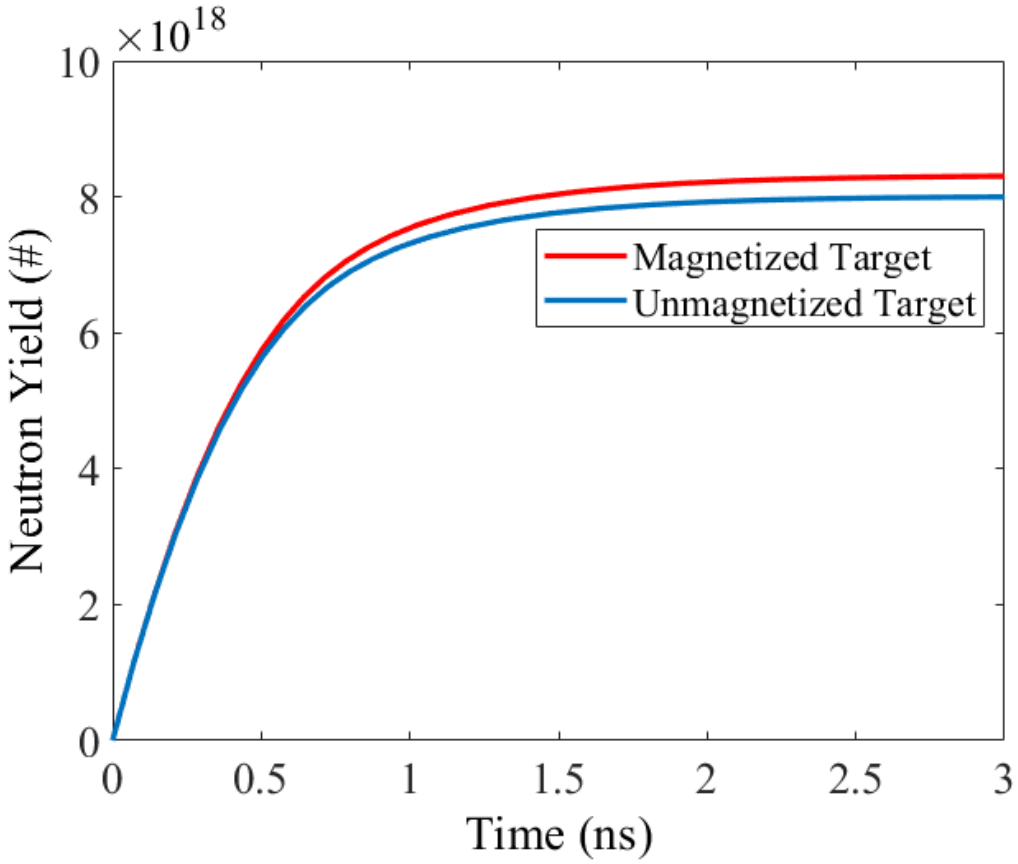

Figure 7.8. Total neutron yield for magnetized and unmagnetized target cases.

7.3 Target and Afterburner Cases

When the hot target is surrounded by a cold afterburner, the target raises the temperature of the afterburner to induce further fusion in the afterburner, causing a dramatic increase in the fusion yield and offer gains greater than unity. It is anticipated that confinement time will be improved with the afterburner because the target will not lose a large amount of thermal energy due to radiation. Rather, the target's thermal energy will

heat the colder fusion fuel in the afterburner and enhance yield if the afterburner is able to ignite.

7.3.1 Magnetized Target and Afterburner

The initial conditions for this case are provided in Table 7.1. Figure 7.9 is a 3D scatter plot of the initial temperature and mass density of this case. A sequence of 3D scatter plots at times 5 ns and 13 ns are shown in Figure 7.13 and Figure 7.15, respectively.

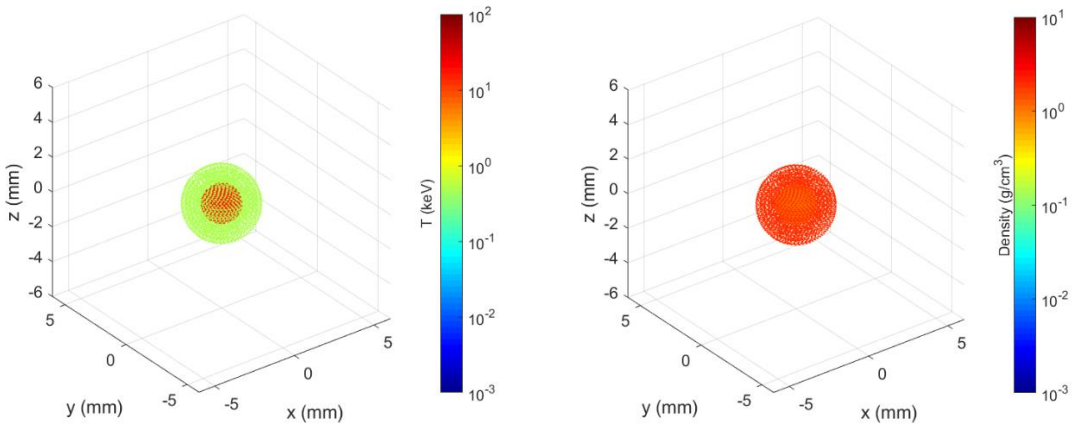

a) b)

Figure 7.9. Magnetized target and afterburner case initial a) temperature and b) mass density.

Figure 7.10 shows a 2D slice of the initial temperature and density of the target and afterburner. The contrast between the temperature and density for the two domains can clearly be seen in this figure.

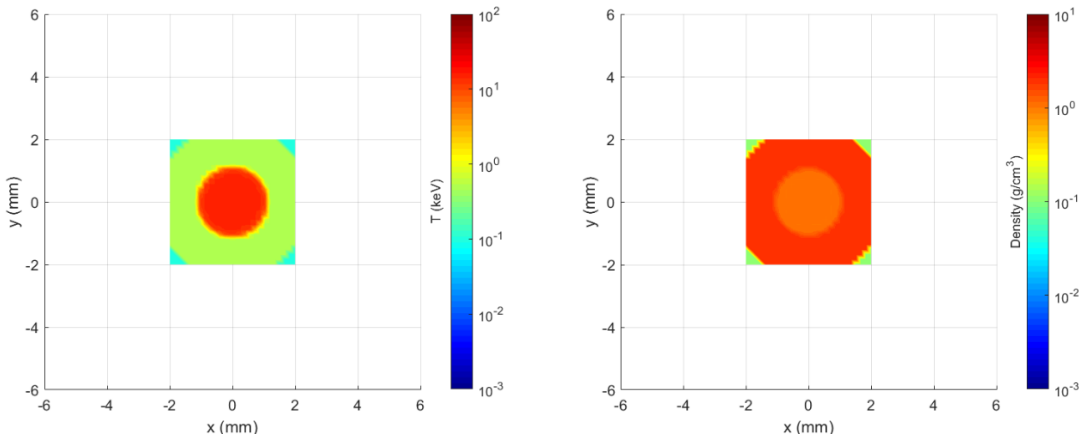

a) b)

Figure 7.10. 2D slice for magnetized target and afterburner case initial a) temperature and b) mass density.

Figure 7.11 shows the continued expansion of the target and the afterburner at 2 ns, at which point the outer radius has expanded to 2.2 mm with an expansion speed of 350 km/s. At this point, the target has heated much of the afterburner to the point that fusion reactions have begun in this additional layer of deuterium-tritium fuel.

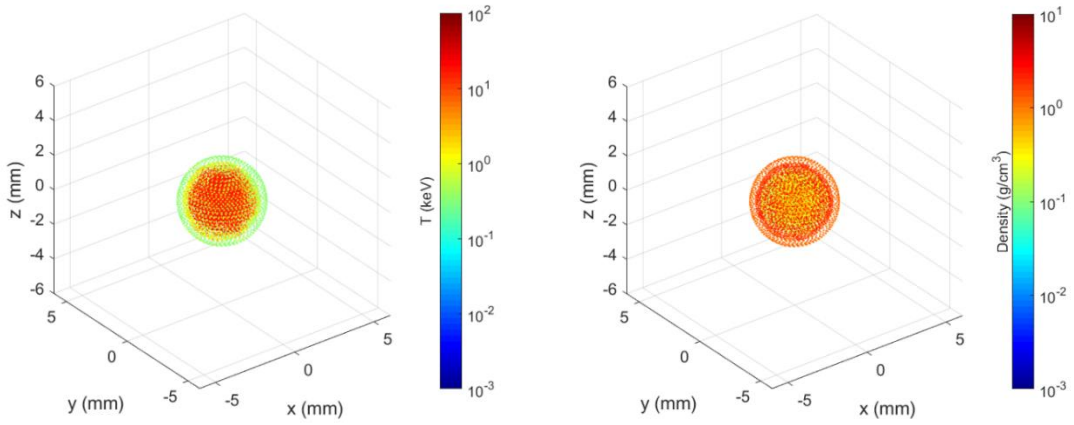

a) b)

Figure 7.11. Magnetized target and afterburner case a) temperature s and b) mass density at t=2 ns.

A 2D slice at 2 ns in Figure 7.12 shows that at this time in the simulation, much of the afterburner has been heated by the target, inducing fusion reactions in the afterburner and enhancing the fusion yield. Subsequent slices at 5 ns and 13 ns in Figure 7.14 and Figure 7.16 show a decrease in the temperature and density of the target and the afterburner as the plasma expands, ultimately limiting the fusion yield.

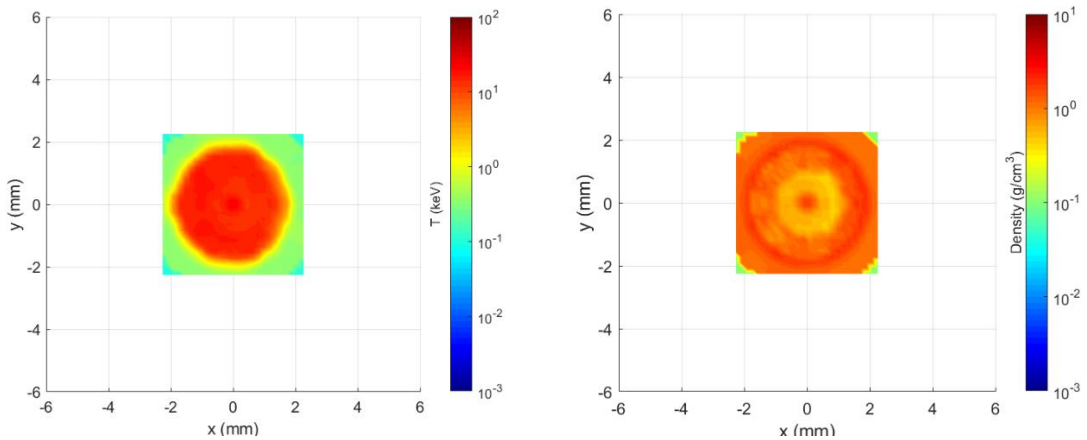

a) b)

Figure 7.12. 2D slice for magnetized target and afterburner case a) temperature and b) mass density at t=2 ns.

Figure 7.13 shows the expansion of the target and afterburner at t=5 ns. As was shown in section 7.2, the fusion yield for the baseline case peaks at about 2 ns, whereas for this case, the fusion reactions continue for a longer amount of time, as will be shown later in this subsection.

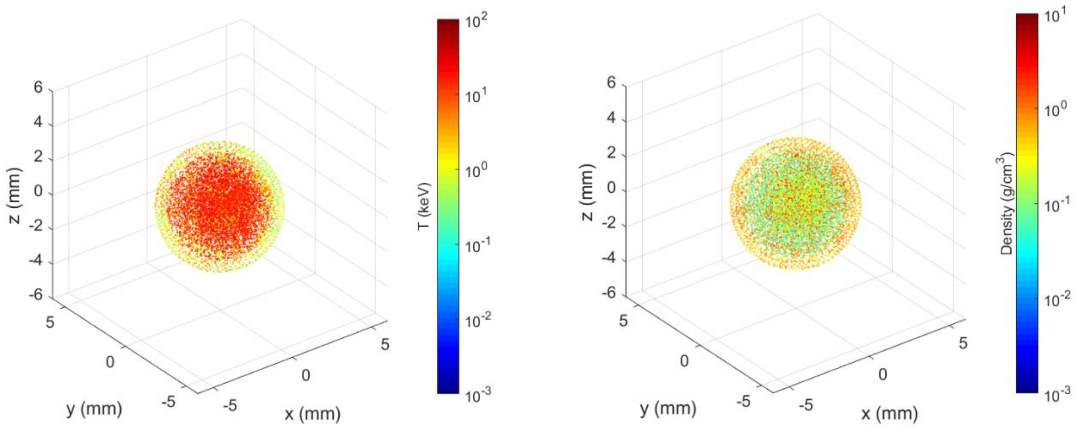

a) b)

Figure 7.13. Magnetized target and afterburner case a) temperature s and b) mass density at t=5 ns.

A 2D slice of temperature and density at this time shows that the outer layers of the afterburner have begun to cool as the fusion fuel continues to expand. The density has also begun to decrease, and this will be shown to negatively affect the fusion yield.

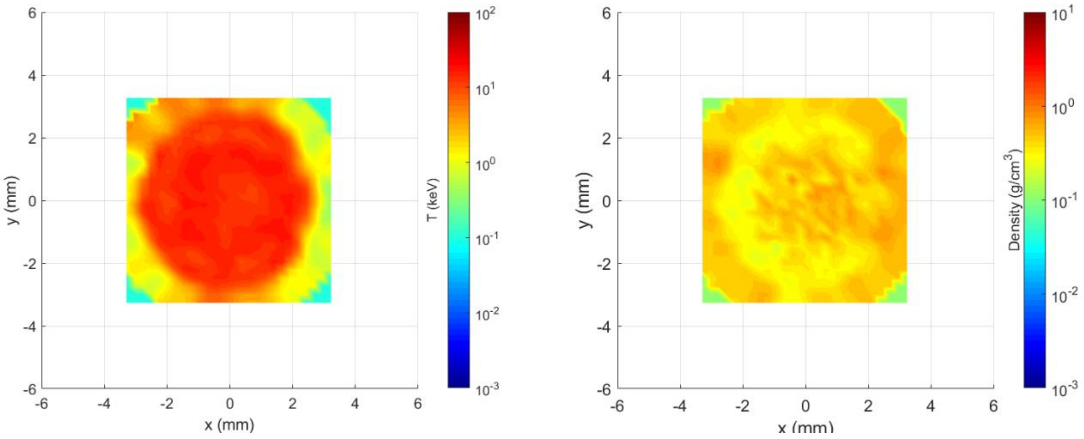

a) b)

Figure 7.14. 2D slice for magnetized target and afterburner case a) temperature and b) mass density at t=5 ns.

Figure 7.15 shows a scatter plot of the target and afterburner at 13 ns. At this point, the outer radius has expanded to 6 mm, with both the temperature and density having fallen dramatically.

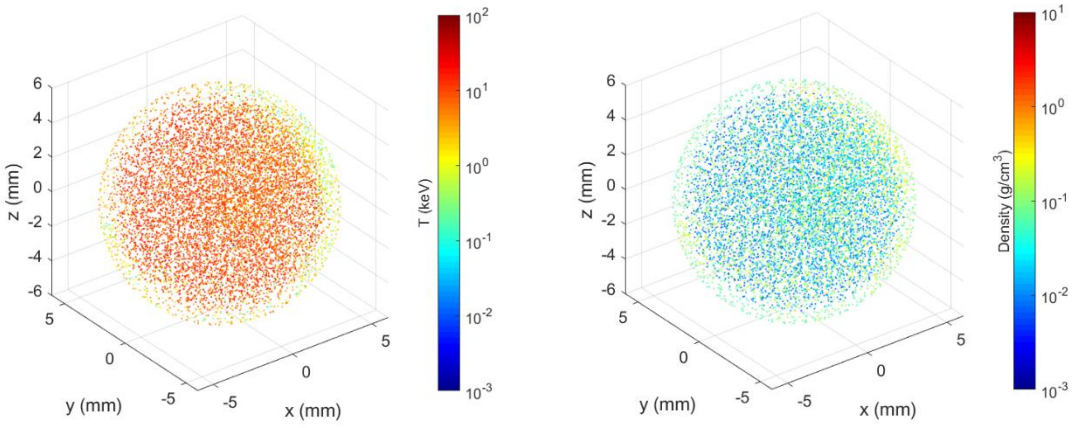

a) b)

Figure 7.15. Magnetized target and afterburner case a) temperature s and b) mass density at t=13 ns.

A 2D slice of temperature and density is shown in Figure 7.16. At this point, both the temperature and density having fallen dramatically due to the expansion process, and effectively brought an end to the fusion reactions.

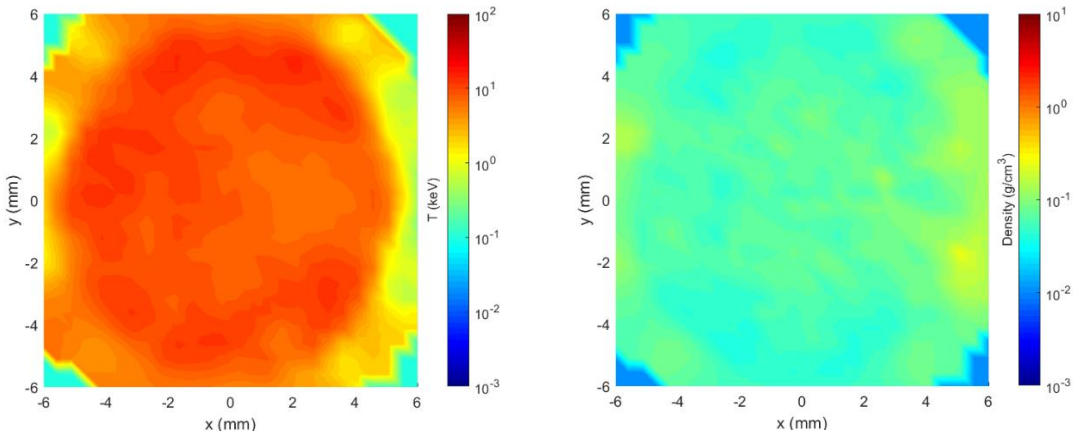

a) b)

Figure 7.16. 2D slice for magnetized target and afterburner case a) temperature and b) mass density at t=13 ns.

Line slices of both the temperature and density taken throughout the target at 0, 2, 5, and 13 ns are shown in Figure 7.17 and Figure 7.18, respectively. Initially, there is an increase in temperature at the center of the target, and the temperature at the outer edges of the slices are seen to increase as the target heats the afterburner and fusion reactions begin to occur in this outer layer of D-T. During this time, the density in both the target and the afterburner decrease due to expansion.

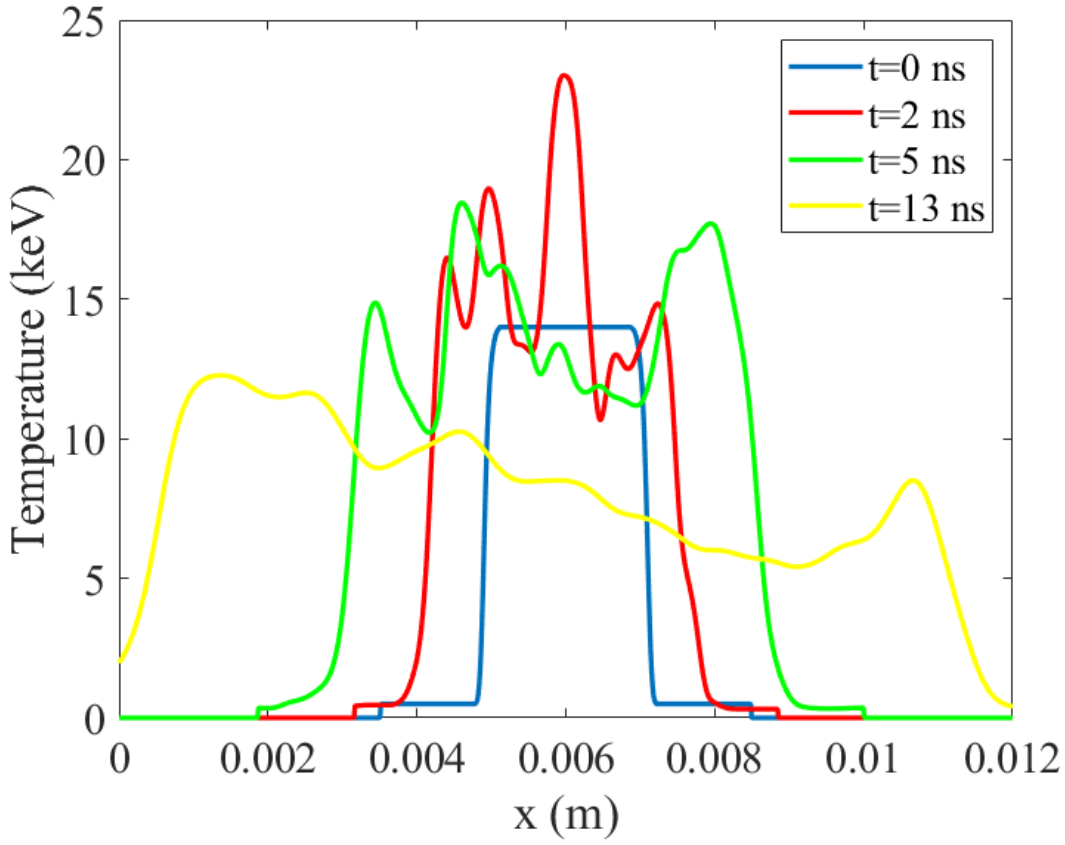

Figure 7.17. Temperature line slices through magnetized target and afterburner taken at 0, 2, 5, and 13 ns.

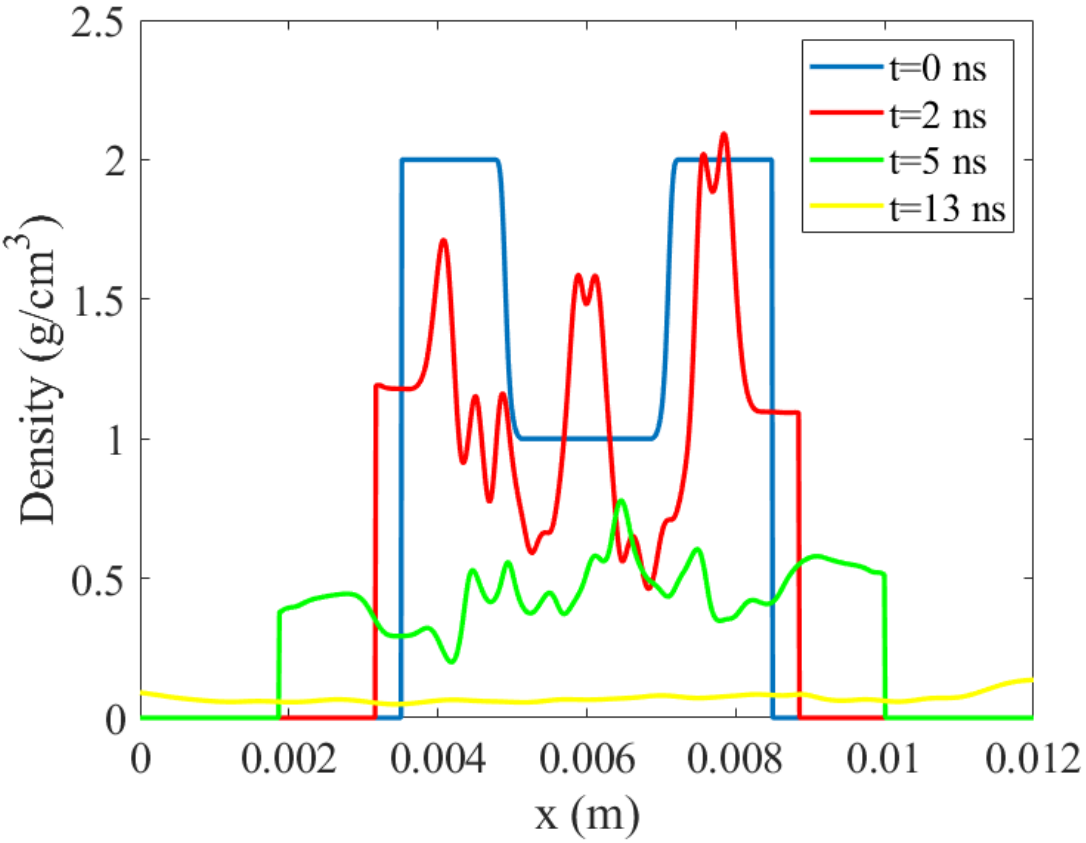

Figure 7.18. Density line slices through magnetized target and afterburner taken at 0, 2, 5, and 13 ns.

Plots of the fusion power production and power losses are shown in Figure 7.19. Due to the presence of the 1,000 T magnetic field, power losses from cyclotron radiation occur in this simulation. But as with the baseline case, the majority of the power losses are due to the expansion of the target. The power losses from Bremsstrahlung are seen to be nearly an order of magnitude lower than losses from expansion, while the cyclotron radiation losses are nearly three orders of magnitude lower.

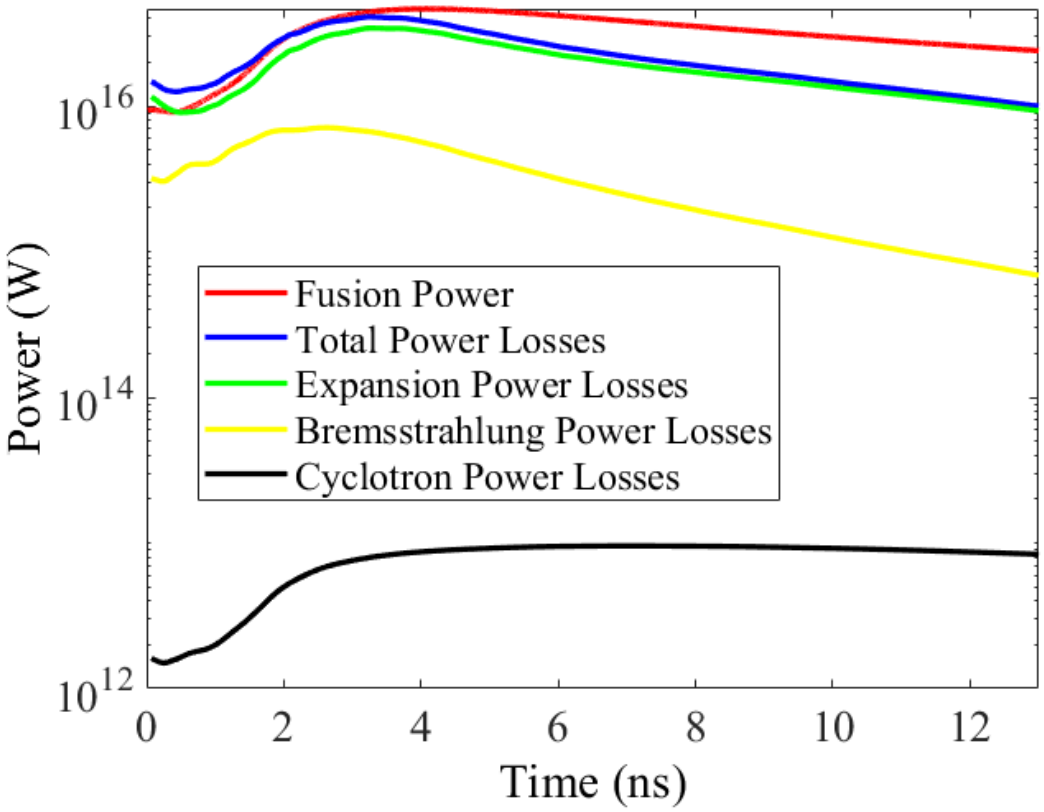

Figure 7.19. Fusion power production and power losses from expansion, Bremsstrahlung, and cyclotron radiation.

Plots of the total fusion energy and neutron yield versus time for both the baseline case and the magnetized target and afterburner case are provided in Figure 7.20 and Figure 7.21, respectively. Comparing these results shows that the fusion burn time is significantly greater when both an afterburner and an embedded magnetic are included, with the burn time increasing from three nanoseconds for the baseline case to thirteen nanoseconds when the afterburner and magnetic field are included.

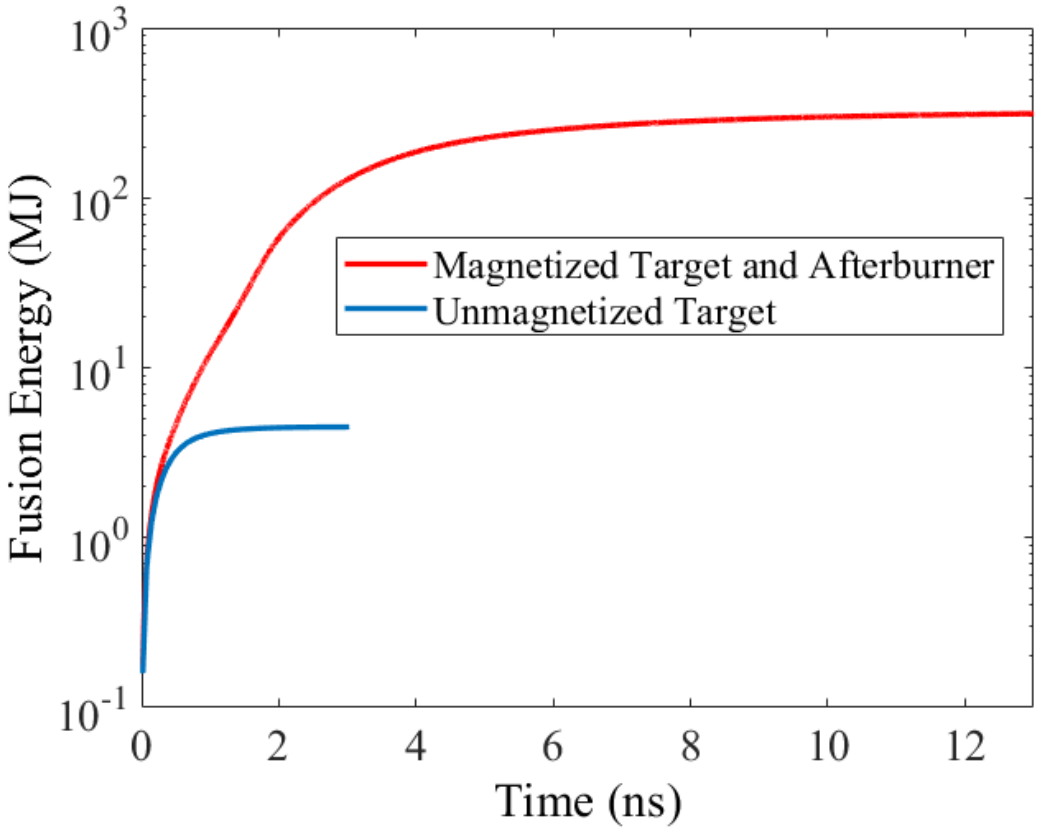

Figure 7.20. Total fusion energy yield for magnetized target/afterburner and unmagnetized target cases.

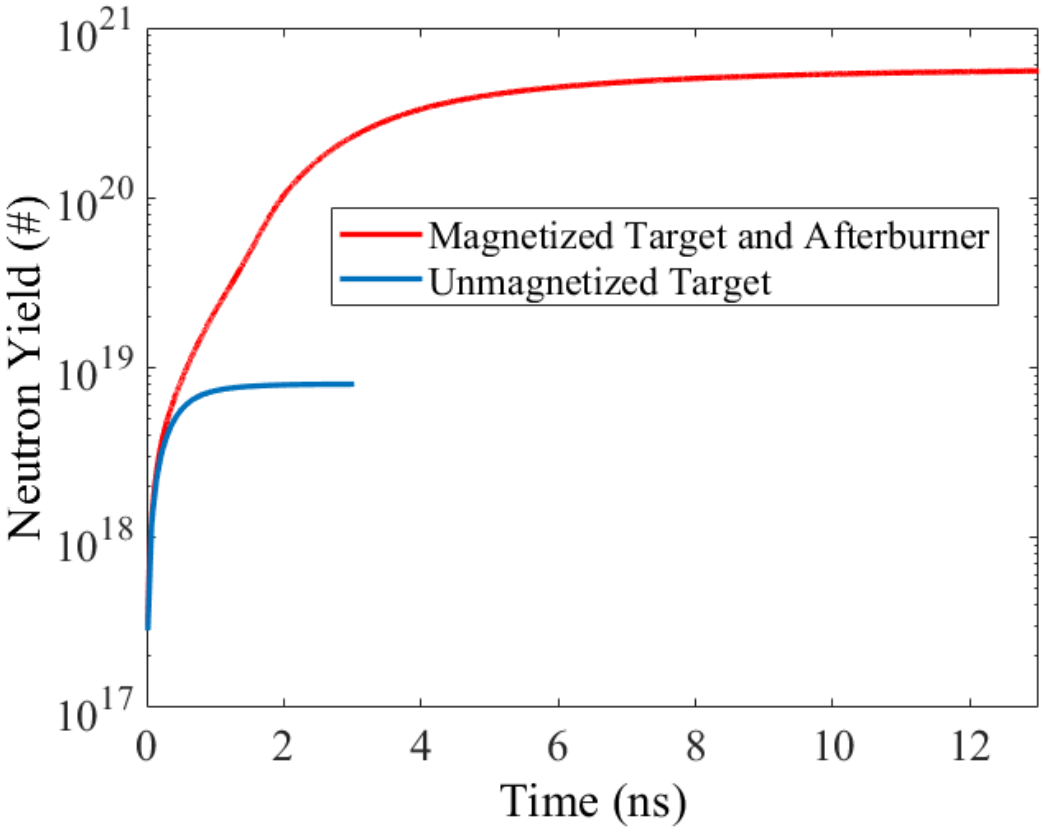

Figure 7.21. Total neutron yield for magnetized target/afterburner and unmagnetized target cases.

Compared to the unmagnetized target, both the fusion energy and neutron yield increase by nearly two orders of magnitude, and provides an energy gain of 25.12, as shown in Table 7.3.

An additional simulation was run with no magnetic field and an afterburner with a density of 3 g/cm^3. This resulted in a fusion energy yield of 611 MJ and an energy gain of 42.17.

Line slices of the temperature and density for the unmagnetized target, magnetized target, unmagnetized target and afterburner, and magnetized target and afterburner cases

are shown in Figure 7.22 and Figure 7.23, respectively. The magnetized target can be seen to have slightly higher temperature and density than the unmangetized target as time progresses, which can be attributed to the enhanced stopping power provided by the embedded magnetic field. When the afterburner is included, the temperature and density at the center of the target can be seen to increase, which can be attributed to the increased mass confinement time provided by the afterburner. Once a magnetic field is included in both the target and afterburner, the enhanced stopping power allows for the center of the target to reach even higher temperatures and densities, the larger number of fusion reactions allows for more of the afterburner to continue burning for a longer amount of time. This allows for the temperature of both the target and afterburner to remain higher for a longer simulation time.

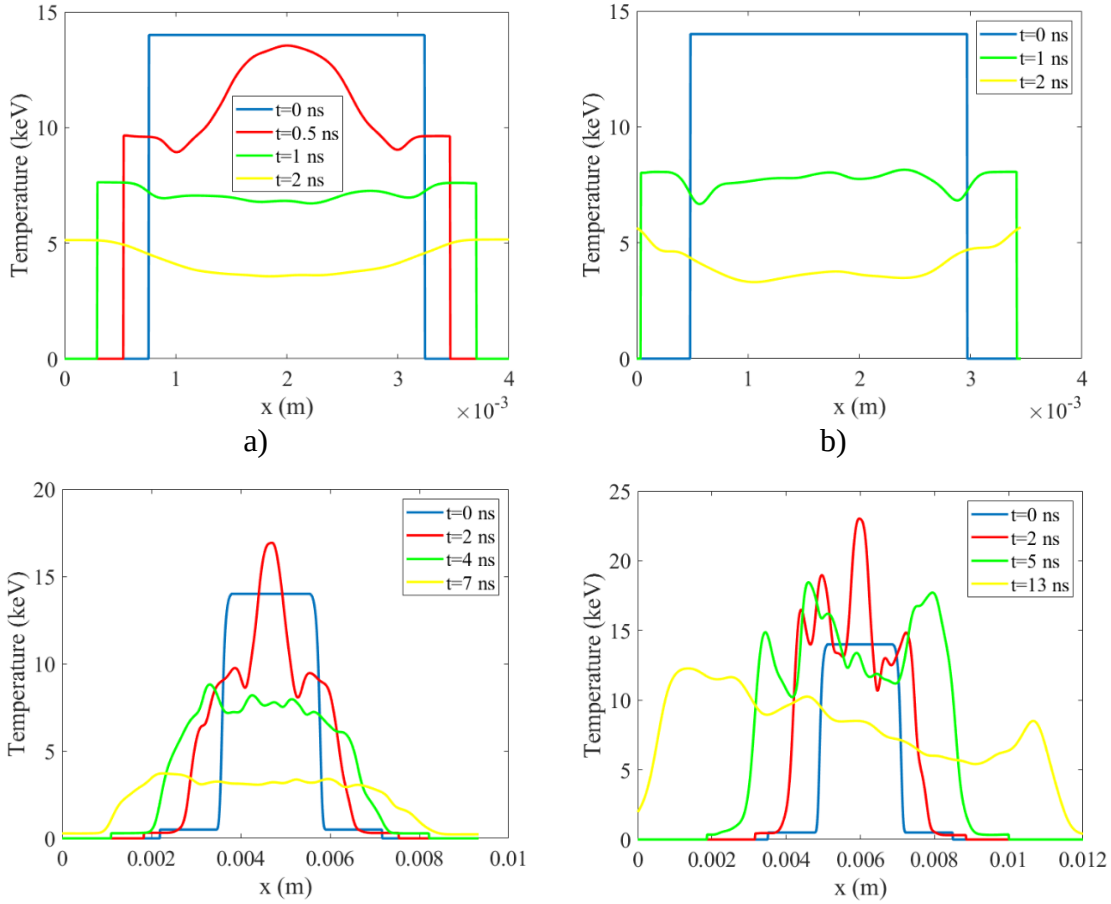

Figure 7.22. Temperature line slices for a) unmagnetized target, b) magnetized target, c) unmagnetized target and afterburner, and d) magnetized target and afterburner.

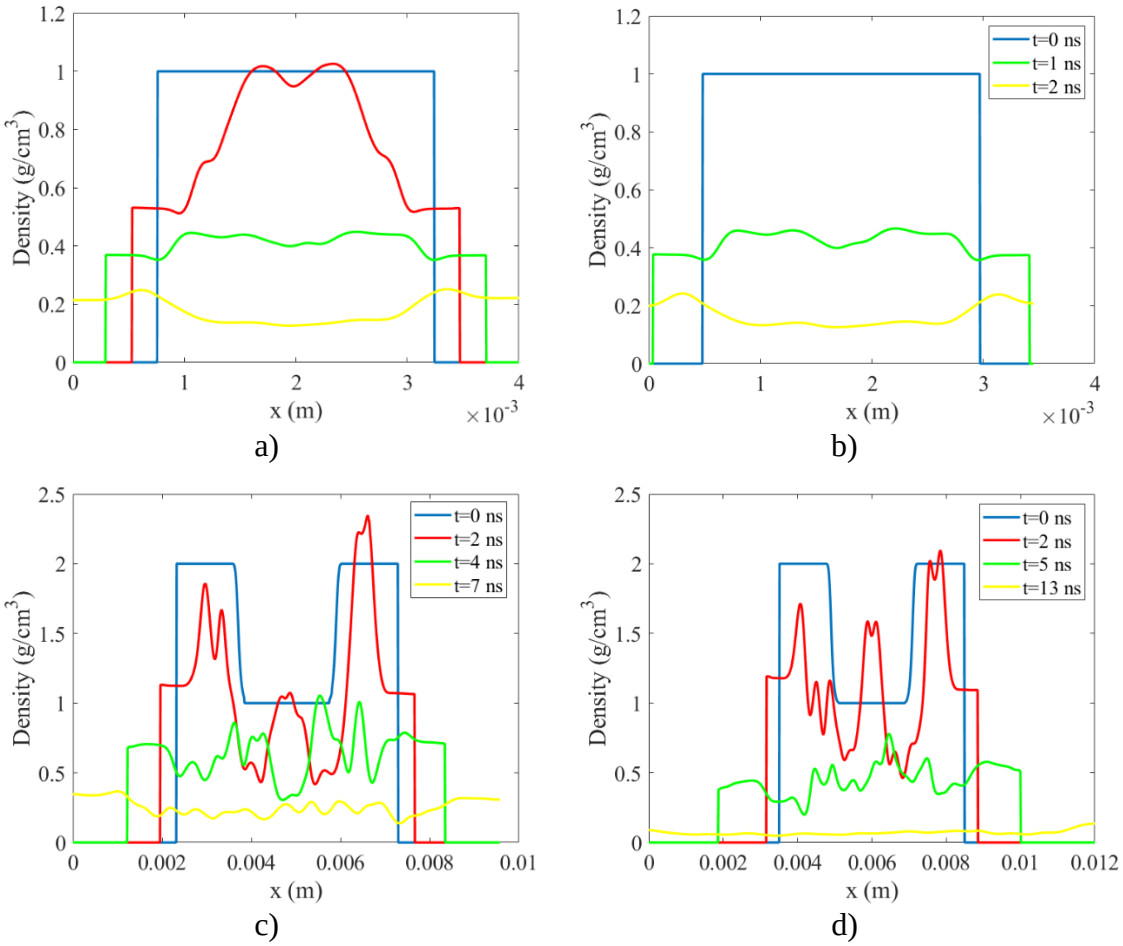

Figure 7.23. Density line slices for a) unmagnetized target, b) magnetized target, c) unmagnetized target and afterburner, and d) magnetized target and afterburner.

Table 7.3. Simulation results for baseline target and afterburner cases.

Case	Neutron Yield (#)	Fusion Energy Yield (MJ)	Gain
1	8.01×10^{18}	4.5	0.53
2	8.32×10^{18}	4.66	0.55
3	1.09×10^{21}	611	42.17
4	8.48×10^{19}	47.47	3.82
5	5.57×10^{20}	312.3	25.12

Cases 1 and 2 show that there is a marginal improvement in yield when an embedded magnetic field is introduced. Introducing a cold afterburner in Case 4 results in a substantial improvement in yield and an energy gain greater than unity. The yield and gain are further enhanced by nearly an order of magnitude once an embedded magnetic field is used in the target and afterburner for Case 5. Even further yield improvement is seen in Case 3 when the density of the afterburner is increased to 3 g/cm^3.

7.4 Non-Uniform Cases

All of the simulations presented thus far have been for a spherically uniform target and afterburner. However, it may be difficult to achieve such conditions in a laboratory. A target and afterburner formed in an actual PJMIF experiment are likely to have non-uniformities. This is a phenomenon that requires three-dimensional simulations in order to be studied. To conduct such simulations, it is first necessary to present the mathematics of spherical harmonics, which is discussed in the following subsection.

7.4.1 Spherical Harmonics

A function F on a spherical surface can be represented by an infinite series of spherical harmonics given by [150, 151]

$$F(\theta,\phi) = \sum_{l=0}^{\infty} \sum_{m=-l}^{l} f_l^m Y_l^m(\theta,\phi) \tag{7.1}$$

The harmonic $Y_l^m(\theta,\phi)$ is an eigenfunction given by

$$Y_l^m(\theta,\phi) = \sqrt{\frac{2l+1}{4\pi}\frac{(l-m)!}{(l+m)!}} P_l^m \cos\theta\, e^{im\phi} \tag{7.2}$$

in which P_l^m is the Legendre polynomial function given by

$$\begin{aligned} P_l^m(x) &= \frac{(-1)^m}{(2^l!)(1-x^2)^{m/2}} \frac{d^{l+m}}{dx^{l+m}}(x^2-1)^l \qquad 0 \le m \le l \\ P_l^{-m}(x) &= (-1)^m \frac{(1-m)!}{(1+m)!} P_l^m(x) \qquad 1 \le m \le l \end{aligned} \tag{7.3}$$

The coefficients are obtained from

$$Yf_l^m = \int_S d^2\hat{s} f(\hat{s}) Y_l^m(\hat{s}) \tag{7.4}$$

in which $\hat{s}$ is a unit vector in the direction towards the surface element

$$d^2(\hat{s}) = \sin\theta\, d\theta d\phi \tag{7.5}$$

over which f is evaluated.

By using the maximum degree, the number of harmonics can be determined as

$$N_h = (l_{max}+1)^2 \tag{7.6}$$

For a matrix of normalized harmonics of size $N_p \times N_h$ and a column vector of coefficient f_h, the function F can be approximated at N_p points on a spherical surface as a function of θ and ϕ by

$$F_p \approx Y_{ph} \times f_h \tag{7.7}$$

Y_{ph} is a set of normalized tesseral spherical with elements given by

$$Y_l^m = \begin{cases} \sqrt{2}\sqrt{\dfrac{(2l+1)(l-|m|)!}{4\pi(l-|m|)!}}P_l^m \cos\theta \sin(|m|\phi) & if\ m < 0 \\ \sqrt{\dfrac{2l+1}{4\pi}}P_l^0 \cos\theta & if\ m = 0 \\ \sqrt{2}\sqrt{\dfrac{(2l+1)(l-|m|)!}{4\pi(l-|m|)!}}P_l^m \cos\theta \cos(m\phi) & if\ m > 0 \end{cases} \quad (7.8)$$

A visual representation of the first several spherical harmonics is shown in Figure 7.24

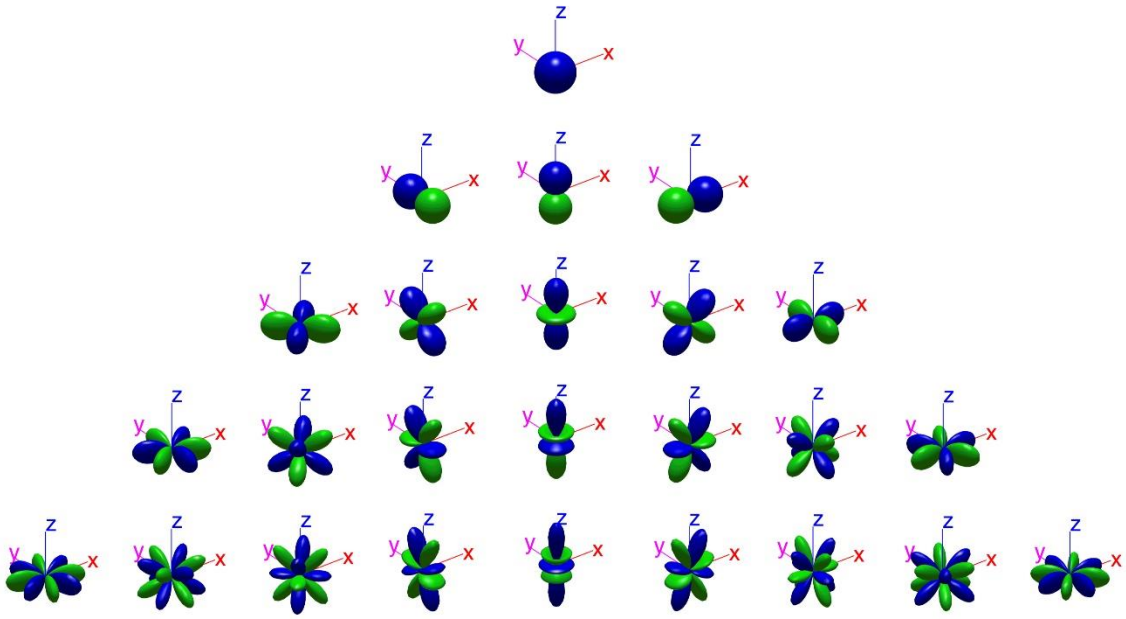

Figure 7.24. Visual representation of spherical harmonics taken from [151].

To determine the coefficients to scale the spherical harmonics, a linear system of N_p equations is solved for the vector of the spherical harmonic coefficients given by

$$\left[Y_{ph}^{T} \times diag(W_p) \times Y_{ph}\right] f_h = \left[Y_{ph}^{T} \times diag(W_p) \times F_p\right] \tag{7.9}$$

in which the weights are the solid angles of each point on the surface, $\Delta\theta\Delta\theta \sin\theta$

The wavelength of the spherical harmonic can be approximated as

$$\lambda = \frac{2\pi}{l + 1/2} \tag{7.10}$$

The wave number is given by

$$k = \frac{\sqrt{l(l+1)}}{2\pi} \tag{7.11}$$

With this mathematical framework, it is possible to simulate fusion targets in SPFMax that have a predefined degree, mode, and amplitude.

7.4.2 Non-uniform Unmagnetized Target

Six different simulations of the unmagnetized baseline target were simulated, each with an amplitude of 0.5 and varying degrees and orders. The initial density, temperature, and mass were set to be the same as the uniform baseline case. The initial temperature and density for a non-uniform target with an amplitude of 0.5, a degree of 2, and an order of 1 is shown in Figure 7.25

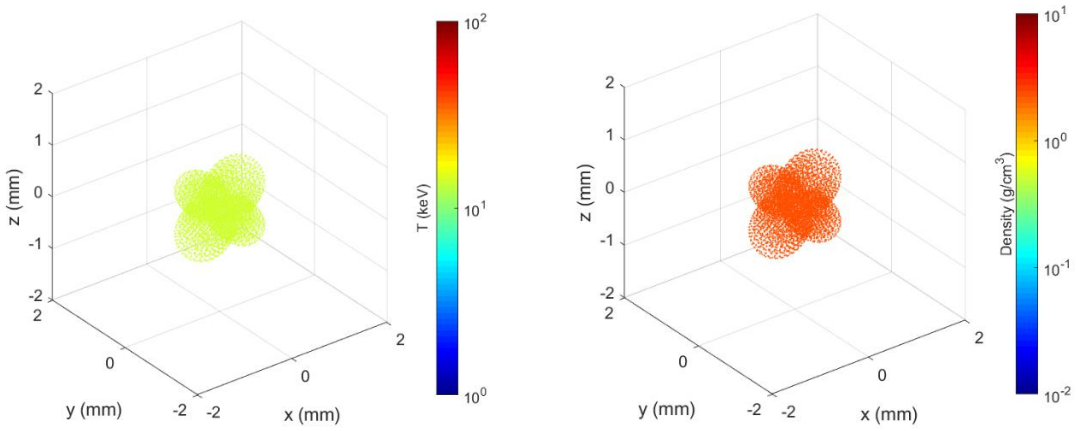

a) b)

Figure 7.25. Non-uniform unmagnetized target with l=2, m=1, and amplitude=0.5 initial a) temperature s and b) mass density.

Figure 7.26 shows a 2D slice of the temperature and density of the non-uniform target. The lower temperature and density values seen at the boundary of the slice are interpolated values obtained from the lumps of the non-uniform target and the vacuum between the lumps.

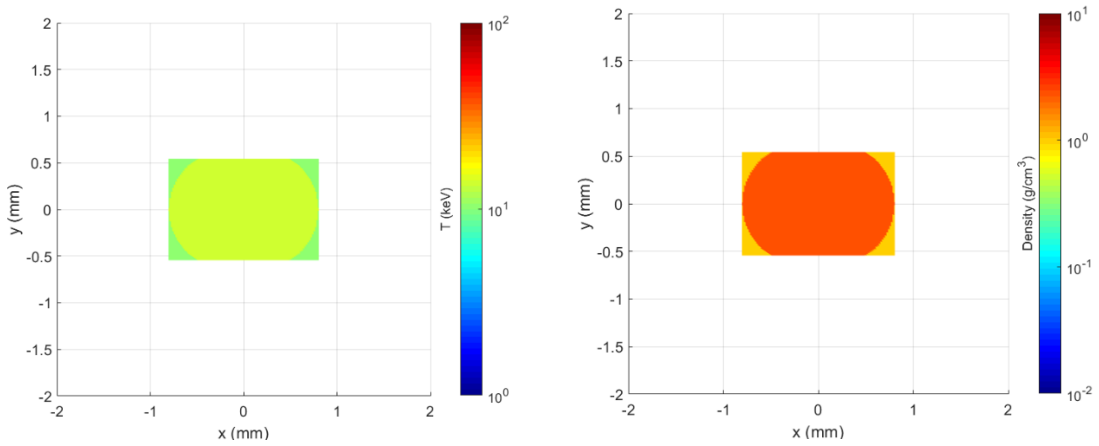

a) b)

Figure 7.26. 2D slice for perturbed unmagnetized target case with l=2, m=1, and amplitude=0.5 initial a) temperature s and b) mass density.

Figure 7.27 shows the continued expansion of the non-uniform target. At 1 ns, the target has expanded to a maximum radius of 1.1 mm. The temperature and density in the target's lumps can be seen to be lower than what is present toward the center of the target.

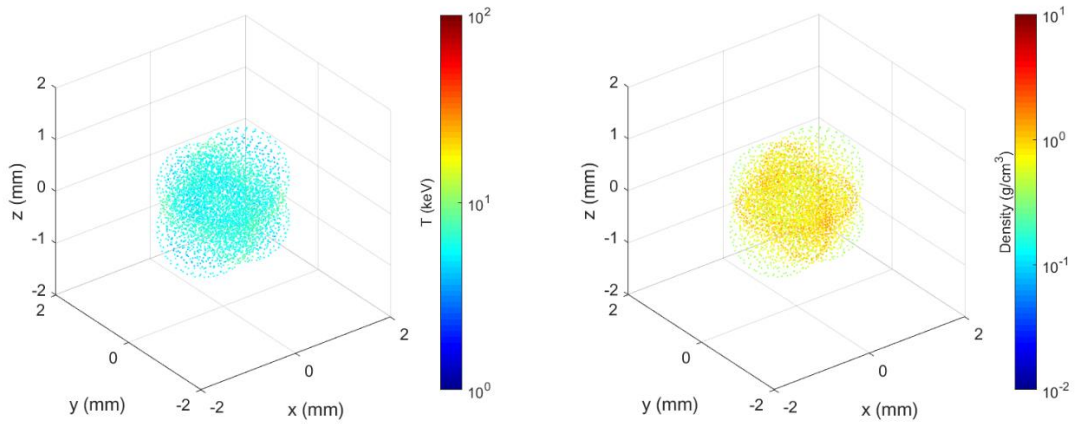

a) b)

Figure 7.27. Non-uniform unmagnetized target with l=2, m=1, and amplitude=0.5 initial a) temperature s and b) mass density at t=1 ns.

This can be seen in a planar slice of the target, shown in Figure 7.28. Here, the non-uniform shape can clearly be seen closer to the center of the target, with the lower temperatures and pressures located along the lumps.

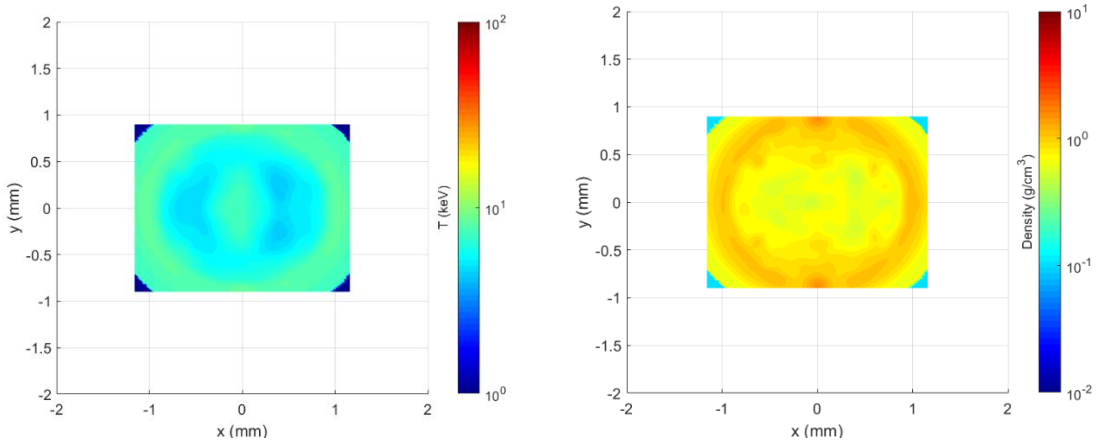

a) b)

Figure 7.28. 2D slice for perturbed unmagnetized target case with l=2, m=1, and amplitude=0.5 initial a) temperature s and b) mass density at t=1 ns.

Similar to the uniform target, the temperature and density continuously decrease as the non-uniform target expands, as can be seen in the temperature and density scatter plots taken at 2 ns and 3 ns. These plots are shown in Figure 7.29 and Figure 7.30, respectively.

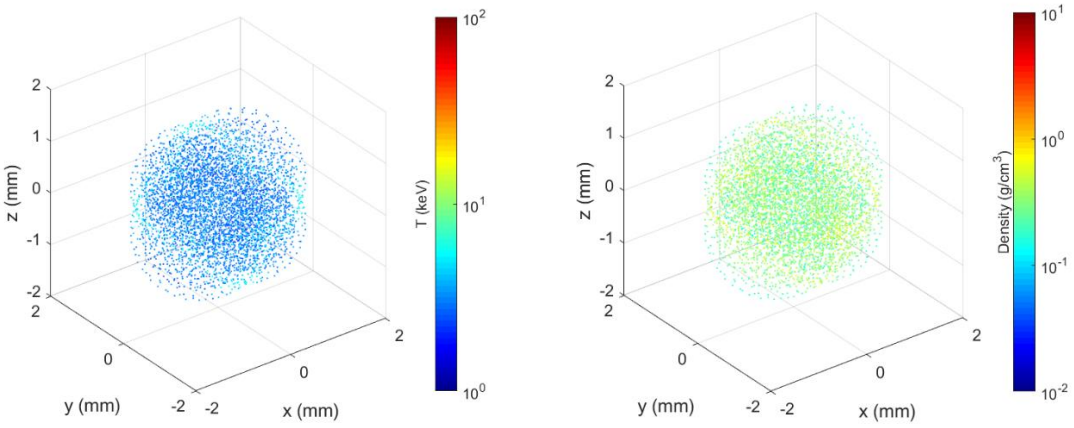

a) b)

Figure 7.29. Non-uniform unmagnetized target with l=2, m=1, and amplitude=0.5 initial a) temperature s and b) mass density at t=2 ns.

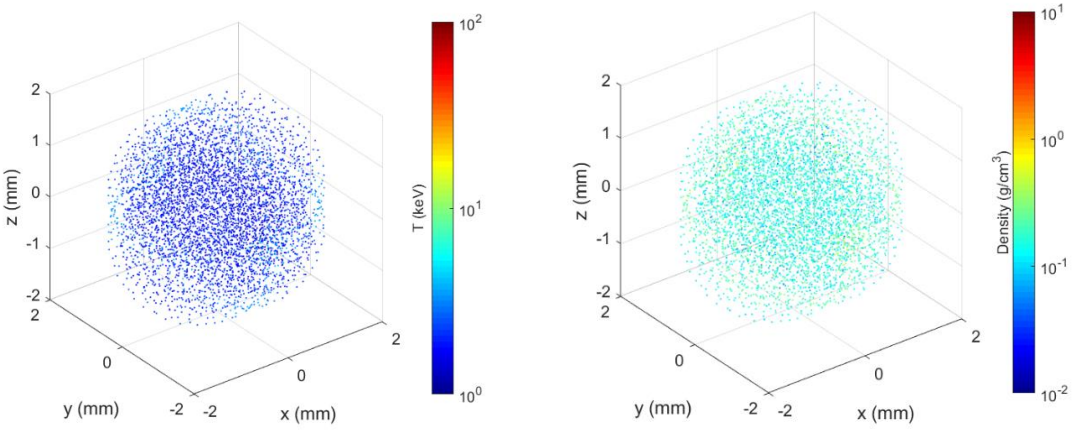

a) b)

Figure 7.30. Non-uniform unmagnetized target with l=2, m=1, and amplitude=0.5 initial a) temperature s and b) mass density at t=3 ns.

2D slices taken at 2 ns and 3 ns show the continued decrease in both the temperature and density throughout the target during the expansion process and a corresponding decrease in the fusion yield. This is similar to the time at which the fusion rate peaked for the uniform target case in section 7.2.

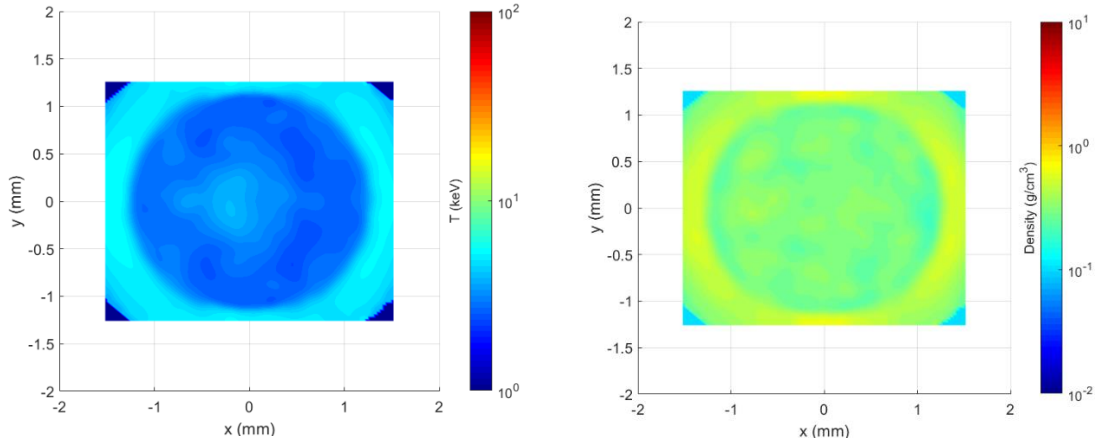

a) b)

Figure 7.31. 2D slice for non-uniform unmagnetized target case with l=2, m=1, and amplitude=0.5 initial a) temperature s and b) mass density at t=2 ns.

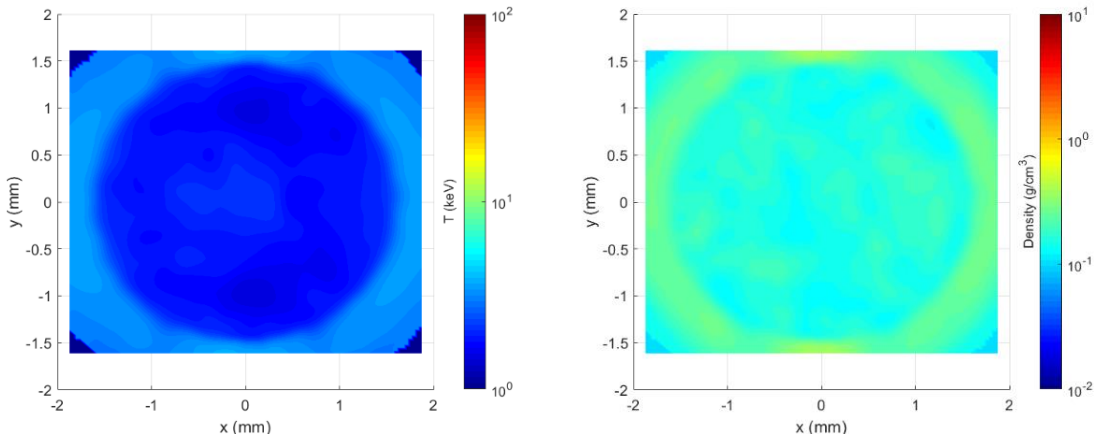

a) b)

Figure 7.32. 2D slice for non-uniform unmagnetized target case with l=2, m=1, and amplitude=0.5 initial a) temperature s and b) mass density at t=3 ns

The fusion and neutron yield for this case are shown in Figure 7.33 and Figure 7.34, respectively. The yield has peaked at about 2 ns, around the same time that peak yield occurred for the uniform case. The overall trend for both the yields and burn time are very similar to the uniform baseline case. This applies to the other non-uniform cases that were examined, as can be seen in the summarized simulation results in Table 7.4

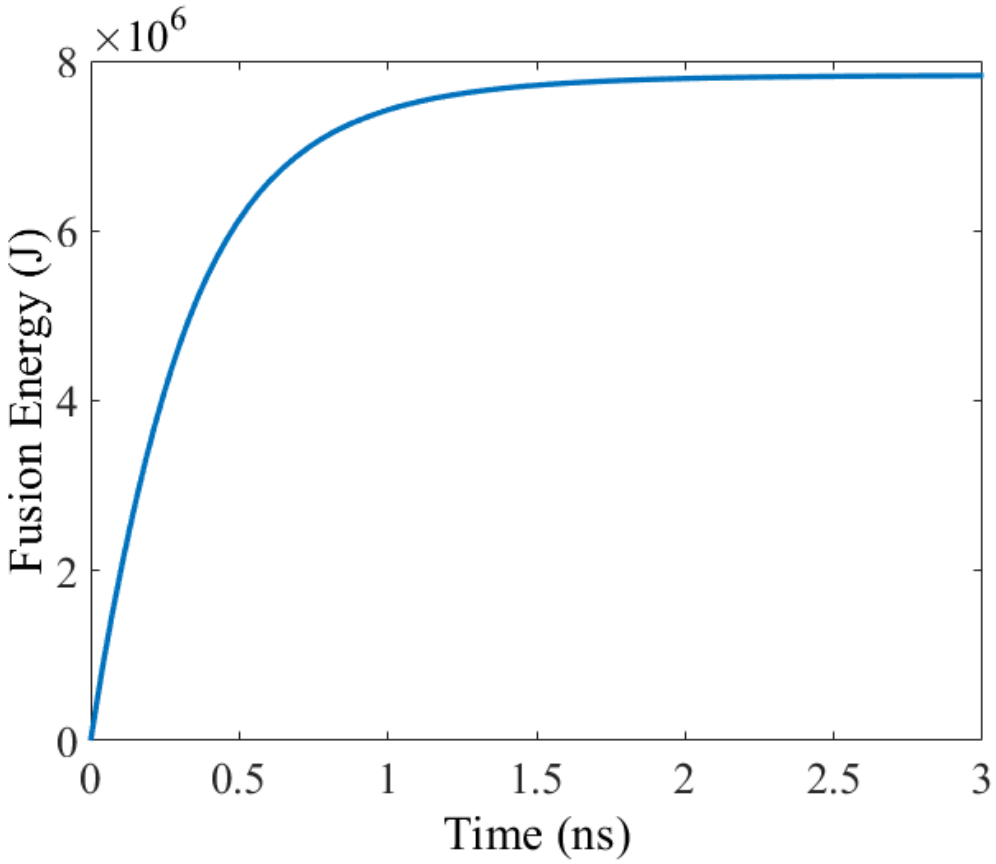

Figure 7.33. Fusion energy yield for non-uniform target with l=2, m=1, and amplitude=0.5.

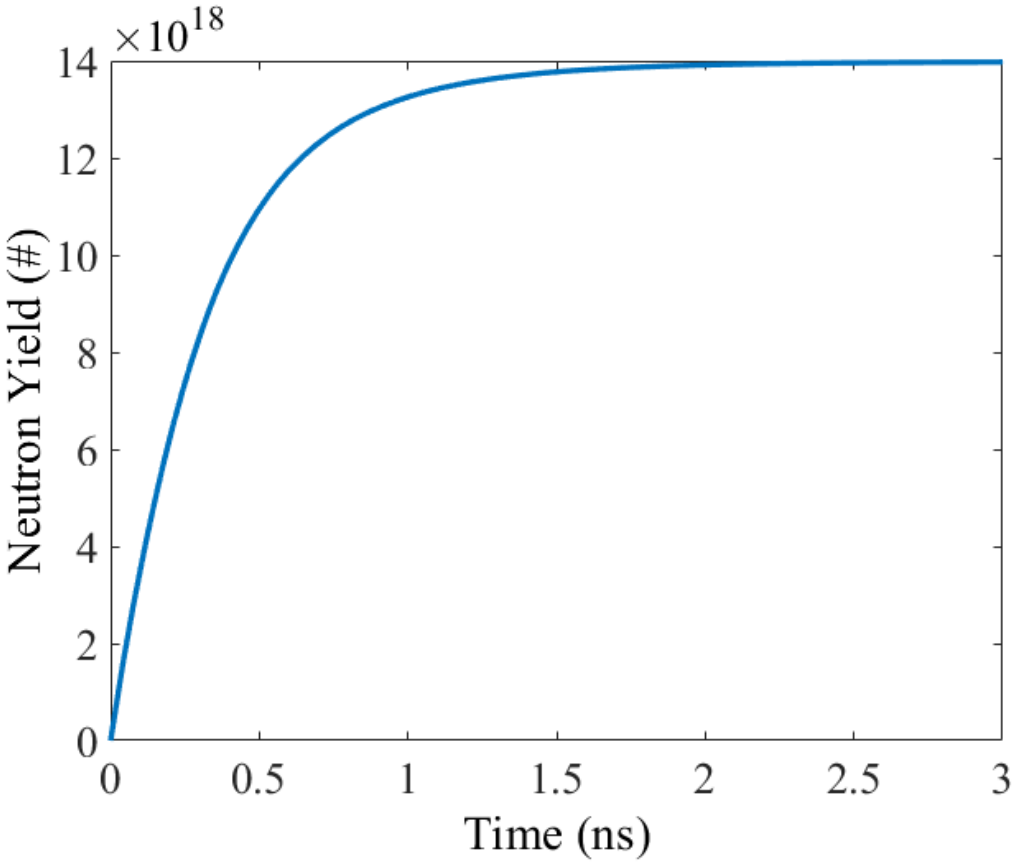

Figure 7.34. Neutron yield for non-uniform target with l=2, m=1, and amplitude=0.5

Table 7.4. Simulation results for non-uniform unmagnetized target.

Case	ρ (kg/m^3)	T (keV)	l	m	a	Neutron Yield (#)	Fusion Energy Yield (MJ)	Gain
1	1,000	14	0	0	0	8.01×10^{18}	4.5	0.526
2	1,000	14	2	1	0.5	7.849×10^{18}	4.4	0.514
3	1,000	14	14	8	0.5	8.615×10^{18}	4.82	0.5711
4	1,000	14	12	7	0.5	8.64×10^{18}	4.85	0.567
5	1,000	14	2	2	0.5	7.86×10^{18}	4.39	0.512
6	1,000	14	8	5	0.5	7.9×10^{18}	4.43	0.519
7	1,000	14	10	6	0.5	8.35×10^{18}	4.68	0.545

These results indicate that surface non-uniformities do not have a major effect on the yield of an unmagnetized target. However, as was shown in Section 7.3, an embedded magnetic field and cold afterburner are necessary in order to generate large yields and energy gains in the PJMIF concept. Therefore, it is necessary to determine if these same non-uniformities have an effect on the yield when both an embedded magnetic field and afterburner are included.

7.4.3 Non-uniform Magnetized Target and Afterburner

In these cases, the afterburner has the same initial mass, density, and temperature that were used in the uniform simulation discussed in Section 7.3. Figure 7.35 shows a scatter plot of the initial conditions of the uniform afterburner along with the non-uniform target.

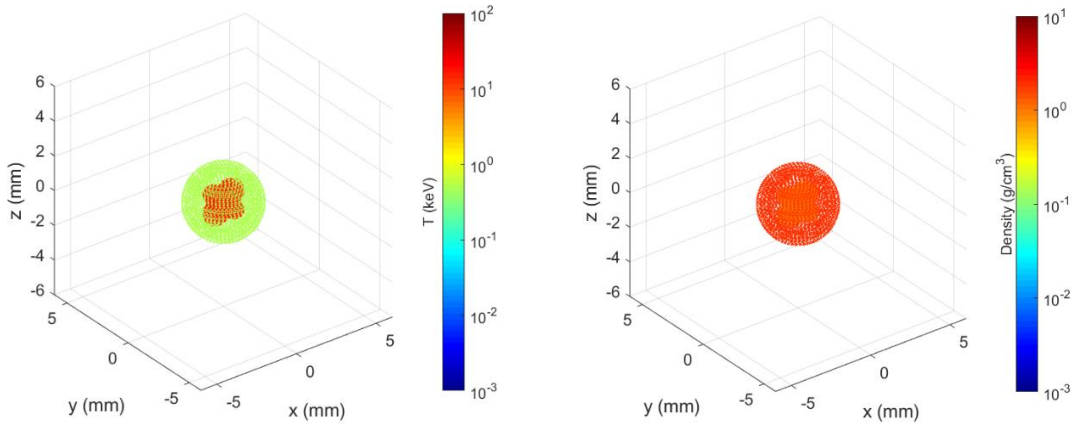

a) b)

Figure 7.35. Magnetized target with l=2, m=1, and amplitude=0.5 and uniform afterburner initial a) temperature and b) mass density.

In this case, only the lumps of the non-uniform target are in contact with the surface of the afterburner, with a significant volume occupied by vacuum due to the valleys in the non-uniform target. This can be seen more clearly with a planar slice through the target and afterburner at the initial conditions, shown in Figure 7.36

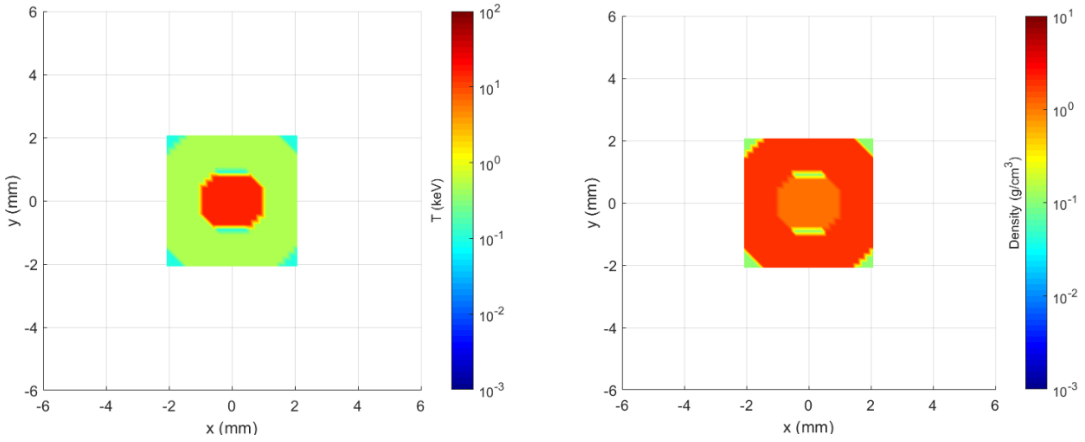

a) b)

Figure 7.36. 2D slice of non-uniform magnetized target with l=2, m=1, and amplitude=0.5 and uniform afterburner initial a) temperature and b) mass density.

The limited amount of contact between the target and afterburner limits the amount of thermal energy transferred from the target to the afterburner. This can be seen as the simulation progresses.

Figure 7.37 shows the temperature and density at 5 ns. Similar to the uniform target, much of the afterburner has been heated by the target at this point, allowing for a burn wave to be ignited.

Subsequent slices at 5 ns and 13 ns in Figure 7.37 and Figure 7.39 show a decrease in the temperature and density of the target and the afterburner as the plasma expands, ultimately limiting the fusion yield.

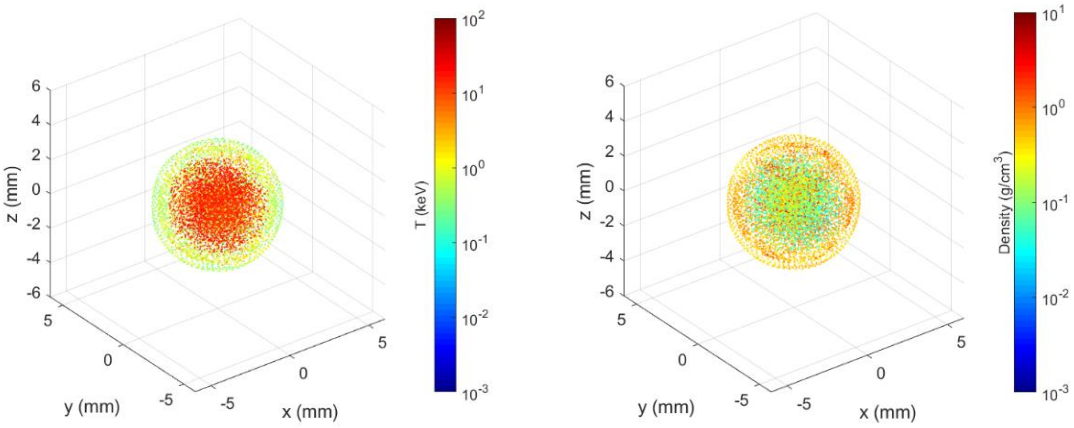

a) b)

Figure 7.37. Magnetized target with l=2, m=1, and amplitude=0.5 and uniform afterburner a) temperature and b) mass density at t=5 ns.

A 2D planar slice is shown in Figure 7.38. Superficially, this slice looks similar to what was obtained at the same point in time for the uniform target and afterburner case. However, it will be shown that the non-uniform surface area of the target in contact with the afterburner reduces the fusion yield by a considerable amount.

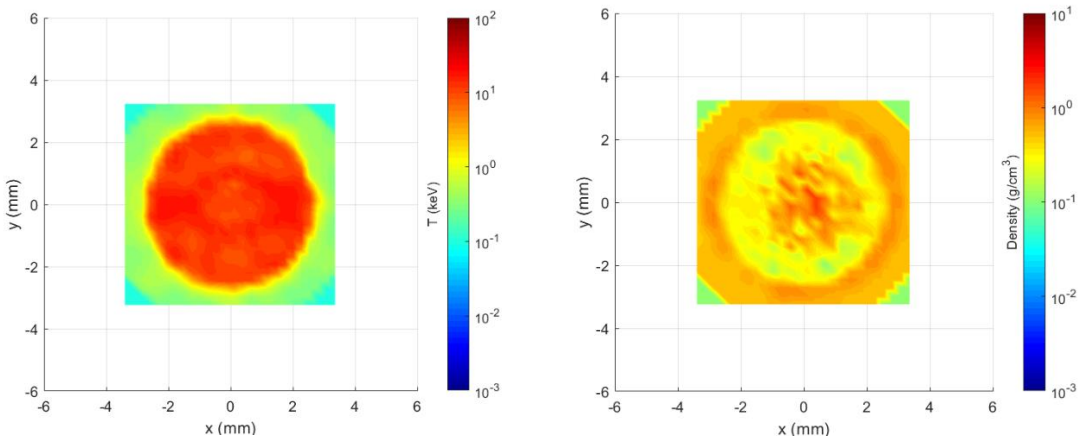

a) b)

Figure 7.38. 2D slice of non-uniform magnetized target with l=2, m=1, and amplitude=0.5 and uniform afterburner a) temperature and b) mass density at t=5 ns.

Figure 7.39 shows the target and afterburner have expanded to a radius of 6 mm by 13 ns, the same radius as the uniform target case for this point in time. Both temperature and density have fallen dramatically at this point due to the expansion process.

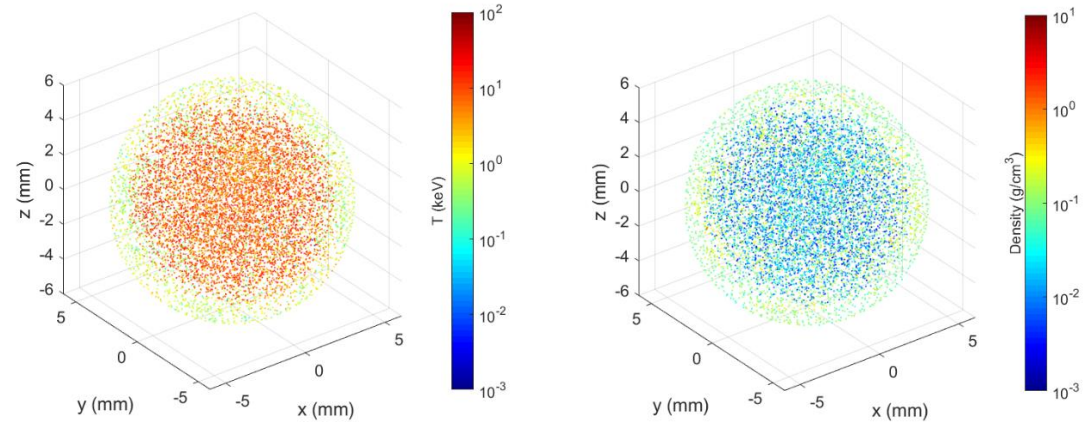

a) b)

Figure 7.39. Magnetized target with l=2, m=1, and amplitude=0.5 and uniform afterburner a) temperature and b) mass density at t=13 ns.

A 2D slice of temperature and density is shown in Figure 7.40. As with the uniform case, both the temperature and density having fallen dramatically and effectively brought an end to fusion reactions.

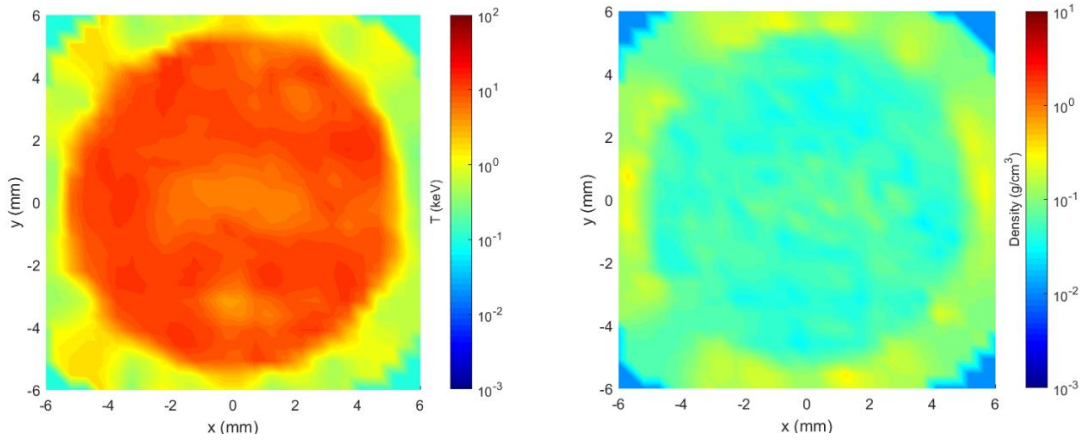

a) b)

Figure 7.40. 2D slice of non-uniform magnetized target with l=2, m=1, and amplitude=0.5 and uniform afterburner a) temperature and b) mass density at t=13 ns.

Plots of the total fusion energy and neutron yield vs time for the magnetized non-uniform target and afterburner are provided in Figure 7.41 and Figure 7.42, respectively.

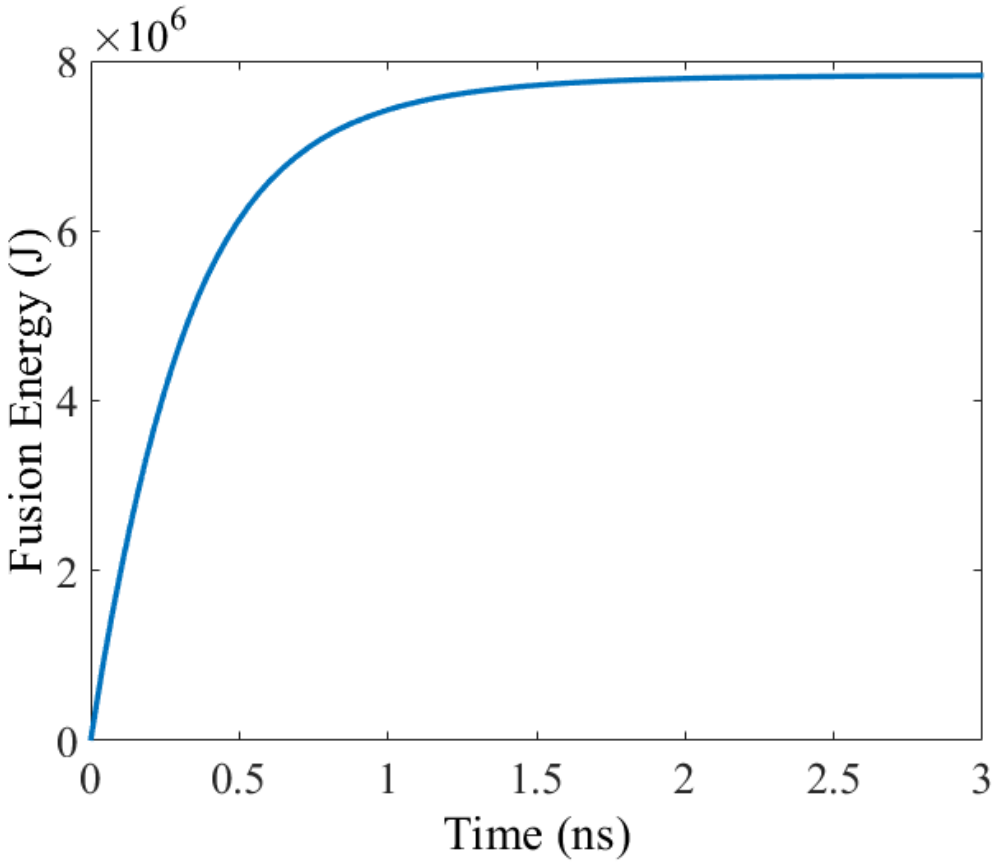

Figure 7.41. Total fusion energy yield for non-uniform target and uniform afterburner.

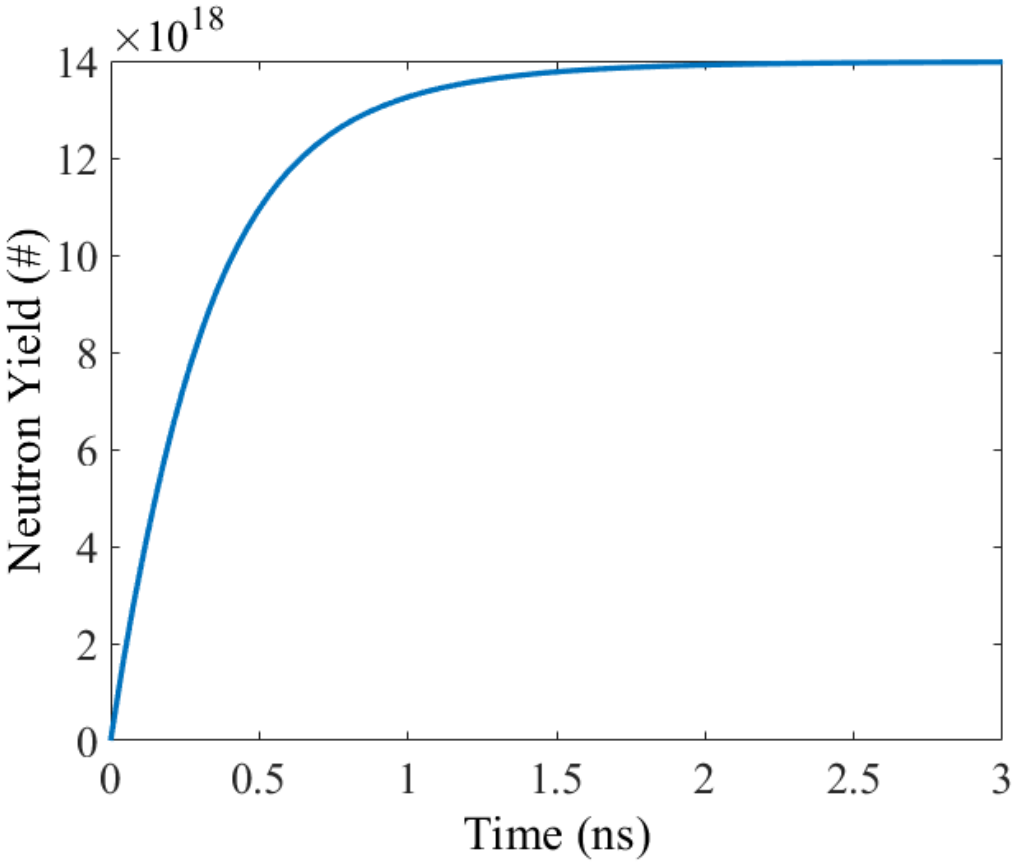

Figure 7.42. Total neutron yield for non-uniform target and uniform afterburner.

The non-uniformities are seen to have a significant effect on the yield compared to the uniform case, with the fusion energy yield and energy gain dropping to 222.6 MJ and 17.64, respectively. The initial conditions and summarized results for these cases are presented in Table 7.5 and Table 7.6, respectively. Therefore, high fusion gain is still possible with non-uniformities on the surface of the target, but the heat flux is lower due to a lower surface area for the target/afterburner boundary. An important aspect not studied here is the effect that these non-uniformities may have on achieving ignition conditions. It is known that instabilities during implosion limit peak compression and target heating, so

future research must investigate which instability modes dominate and how these modes affect compression.

Table 7.5. Initial conditions for non-uniform magnetized target and uniform afterburner cases.

	Target							Liner			
Case	r_t (mm)	ρ_t (kg/m^3)	T_t (keV)	B_t (T)	l	m	a	th_a (mm)	ρ_a (kg/m^3)	T_a (keV)	B_a (T)
1	1	1,000	14	1,000	0	0	0	0.4	2,000	0.5	1,000
2	1.33	1,000	14	1,000	2	1	0.5	0.545	2,000	0.5	1,000
3	1.3	1,000	14	1,000	10	6	0.5	0.565	2,000	0.5	1,000
4	1.3	1,000	14	1,000	12	7	0.5	0.385	2,000	0.5	1,000
5	1.33	1,000	14	1,000	14	8	0.5	0.565	2,000	0.5	1,000

Table 7.6. Simulation results for non-uniform magnetized target and uniform afterburner cases.

Case	Neutron Yield (#)	Fusion Energy Yield (MJ)	Gain
1	5.57×10^{20}	312.3	25.12
2	3.98×10^{20}	222.6	17.64
3	4.36×10^{20}	243.9	19.65
4	4.59×10^{20}	257.3	20.56
5	4.72×10^{20}	264.4	21.44

The results of the magnetized uniform liner and afterburner case are consistent with results from Knapp and Kirkpatrick, who reported a fusion energy yield of 272.6 MJ and a gain of 12.56 for a deuterium-tritium target and afterburner with a xenon liner that had an implosion velocity of 60 km/s. Knapp and Kirkpatrick also reported a maximum fusion

energy gain of 32.13 with a yield of 1,937.9 MJ for a plasma liner with an implosion velocity of 100 km/s. The differences in the yield can be attributed to several factors, including the fact that the Knapp and Kirkpatrick simulation had electron heat conduction turned off to approximate the effect of a strong magnetic field. The one-dimensional nature of their code also could not account for three-dimensional effects that emerge during the expansion process, which also will have lowered the yield and gain. This is consistent with research done at the National Ignition Facility, which has found non-uniformities on fuel capsules to degrade fuel implosion and fusion gain [152-154].

CHAPTER 8

CONCLUSIONS

This dissertation explored alpha particle and neutron yield for deuterium-tritium fusion in a study of three-dimensional physics in plasma jet-driven magneto-inertial fusion. Simulations were conducted for fusion fuel targets at peak compression conditions that are desirable to achieve for the PJMIF concept. These simulations compared the yield and gain obtained from unmagnetized and magnetized fusion fuel targets, as well as the enhancement in yield that can be obtained if a cold afterburner of fusion fuel surrounds the target and can be ignited. Non-uniformities on the surface of the target were found to degrade the yield by limiting the surface interface and heat flux between the target and the afterburner.

SPFMax, a three-dimensional smooth particle hydrodynamic code, was used to study these problems. Prior to conducting the fusion simulations, code verification was performed to verify the capability of using SPFMax to simulate test cases that incorporate the physics of radiation cooling, thermal conduction, viscosity, shock capturing, stopping power, and fusion yield with an accuracy comparable with what has been reported in other

SPH studies. Once this capability was demonstrated, a fusion power balance analysis was conducted in order to construct Lindl-Widner diagrams to determine the parameter space for a fusion fuel target at peak compression over which the PJMIF concept may be viable. These Lindl-Widner diagrams lead to the selection of a deuterium-tritium target with a density of 1 g/cm^3, a radius of 1 mm, and an initial temperature of 14 keV. This target was then simulated in SPFMax, with the results presented in Chapter 7.

An unmagnetized target was first simulated and was found to result in a low fusion yield and energy gain significantly below breakeven. Embedding a 1,000 T magnetic field within the target was seen to offer only marginal improvement in the fusion yield, with the gain still significantly below unity. Surrounding the unmagnetized target with a cold afterburner was found to greatly enhance the yield due to the target igniting the afterburner. Embedding a magnetic field in both the target and the afterburner resulted in the yield increasing by nearly two orders of magnitude compared to the unmagnetized target. An even greater yield was obtained by increasing the density of the afterburner from 2 g/cm^3 to 3 g/cm^3.

Simulations were then conducted with non-uniformities on the surface of the target. In cases without an embedded magnetic field or afterburner, the yield of the non-uniform target was found to be nearly the same as the uniform target. However, when an embedded magnetic field and afterburner are incorporated, the target surface non-uniformities were found to degrade the fusion yield and energy gain compared what was achieved with a uniform target. This yield degradation can be attributed to the non-uniformities reducing the surface interface and resulting heat flux between the target and the afterburner, which in turn reduces the number of fusion reactions that occur in the afterburner.

Conducting these three-dimensional simulations allows for much further investigation of the PJMIF concept. Of particular importance is the compression phase. While the simulations in this study were for a target and afterburner at peak compression, it is vital to simulate what must be done in order to achieve these conditions in a laboratory experiment. Future studies should investigate how to produce the spherical target at the center of a fusion reaction chamber and the subsequent formation of an afterburner to implode and compress the target to fusion conditions. In addition, a xenon plasma liner should also be investigated for compressing both the target and the afterburner, as a heavy noble gas will likely be vital for the PJMIF concept to be viable.

Simulating the liner formation and compression phases should also reveal what instabilities and non-uniformities are likely to emerge during these phases of the PJMIF process. The surface non-uniformities that were examined in this dissertation were predefined and are unlikely to actually occur in an experiment. Nonetheless, these simulations demonstrate the negative effect that a non-uniform target has on fusion yield. More complex non-uniformities and instabilities are likely to develop from the formation of the target, afterburner, and plasma liner. It is crucial for future studies to investigate how these non-uniformities will affect the viability of the PJMIF concept, and if any measures may be taken to mitigate or prevent these non-uniformities from forming.

Future studies may also investigate different magnetic field topologies that may enhance alpha particle energy deposition, as well as the intensity that the field should have once the target is initially magnetized. A wider parameter space for the initial conditions of the target, afterburner, and plasma liner should also be investigated. Much research must be conducted in order to determine what conditions can actually be achieved in laboratory

experiments. Finally, future studies may also investigate so-called advanced fuels such as pure deuterium, deuterium/helium-three mixtures, or p-boron-11 rather than the present deuterium-tritium study.

REFERENCES

[1] H. H. Pass, "Fusion and Advanced Fuel, Reaction Bibliography: Particle Reactions from H1 to B11," Air Force Astronautics Laboratory, Edwards Air Force Base, CA, 1987.

[2] W. M. Nevins, "A Review of Confinement Requirements for Advanced Fuels," *Journal of Fusion Energy,* vol. 17, no. 1, pp. 25-32, March 1998.

[3] J. R. J. McNally, "Advanced Fuels for Nuclear Fusion Reactors," Oak Ridge National Laboratory, Oak Ridge, TN, 1975.

[4] S. Atzeni and J. Meyer-Ter-Vehn, Physics of Interial Fusion: Beam Plasma Interaction, Hydrodynamics, Hot Dense Matter, Oxford: Oxford Science Publications, 2004.

[5] J. D. Lawson, "Some criteria for a useful thermonuclear reactor," Atomic Energy Research Establishment, Harwell, Berkshire, 1955.

[6] A. A. Harms, K. F. Schoepf, G. H. Miley and D. R. Kingdon, Principles of Fusion Energy, World Scientific Publishing, 2000.

[7] S. Hayakawa, N. Hokkyo, Y. Terashima and T. Tsuneto, "Cyclotron Radiation from a Magnetized Plasma," in *2nd Geneva Conference on Peaceful Uses of Atomic Energy,* Geneva, Switzerland, 1958.

[8] W. C. Elmore, J. L. Tuck and K. M. Watson, "On the Inertial-Electrostatic Confinement of a Plasma," *Physics of Plasmas,* vol. 2, no. 3, pp. 239-246, May 1959.

[9] R. W. Bussard, "Some Physics Considerations of Magnetic Inertial-Electrostatic Confinement: A New Concept for Spherical Converging-Flow Fusion," *Fusion Technology,* vol. 19, no. 2, pp. 273-293, 1991.

[10] T. McGuire and R. Sedwick, "Improved Confinement in Inertial Electrostatic Confinement for Fusion Space Power Reactors," *Journal of Propulsion and Power,* vol. 21, no. 4, pp. 697-706, July 2005.

[11] "Inertial Electrostatic Confinement Fusion," University of WIsconsin-Madison, [Online]. Available: https://iec.neep.wisc.edu/. [Accessed 14 December 2018].

[12] F. Winterberg, "Fussion-Fission-Fusion Fast Ignition Plasma Focus," *Physics Letters A,* vol. 336, no. 2-3, pp. 188-192, 2005.

[13] F. Winterberg, "On the ignition of high gain thermonuclear microexplosions with electric pulse power," *Physics of Plasmas,* vol. 11, no. 2, pp. 706-712, 2004.

[14] M. Shimada and et al, "Progress in ITER Physics Basis: Overview and Summary," *Nuclear Fusion,* vol. 47, no. 6, pp. S1-S17, June 2007.

[15] J. Cassibry, R. Cortez, M. Stanic, A. Watts, W. Seidler, R. Adams, G. Statham and L. Fabisinski, "Case and Development Path for Fusion Propulsion," *Journal of Spacecraft and Rockets,* vol. 52, no. 2, pp. 595-611, 2015.

[16] ITER Organization, [Online]. Available: https://www.iter.org/album/Media/7%20-%20Technical. [Accessed 3 May 2018].

[17] "https://lasers.llnl.gov/about/how-nif-works," Lawrence Livermore National Laboratory, [Online]. Available: https://lasers.llnl.gov/about/how-nif-works. [Accessed 12 December 2018].

[18] "What is NIF?," Lawrence Livermore National Laboratory, [Online]. Available: https://lasers.llnl.gov/about/what-is-nif. [Accessed 12 December 2018].

[19] "National Ignition Facility and Photon Sciene," Lawrence Livermore National Laboratory, [Online]. Available: https://lasers.llnl.gov/media/photo-gallery. [Accessed 2 May 2018].

[20] R. C. Kirkpatrick, I. R. Lindemuth and M. S. Ward, "Magnetized Target Fusion: An Overview," *Fusion Technology,* vol. 27, no. 3, pp. 201-214, 1995.

[21] S. A. Slutz and R. A. Vesey, "High-Gain Magnetized Inertial Fusion," *Physical Review Letters,* vol. 108, no. 2, January 2012.

[22] A. Y. Chirkov and Ryzhkov, "The Plasma/Laser Driven Compression of Compact Plasmoids to Fusion Conditions," *Journal of Fusion Energy,* vol. 31, pp. 7-12, February 2012.

[23] O. V. Gotchev, N. W. Jang, J. P. Knauer, M. D. Barbero, R. Betti, C. K. Li and R. D. Petrasso, "Magneto-inertial Approach to Direct-drive Laser Fusion," *Journal of Fusion Energy,* vol. 27, pp. 25-31, 2008.

[24] J. Cassibry, R. Cortez, S. Hsu and F. Whitherspoon, "Estimates of confinement time and energy gain for plasma liner driven magnetoinertial fusion using and analytic self-similar converging shock model," *Physics of Plasmas*, vol. 16, 2009.

[25] R. C. Kirkpatrick, I. R. Lindemuth, P. T. Sheehey, J. A. Guzik, F. J. Wysocki, D. A. Baker, R. W. Moses, A. G. Sgro, R. Siemon, R. A. Gerwin, K. F. Schoenberg and F. Y. C. Thio, "Generation and Compression of a Target Plasma for Magnetized Target Fusion," Los Alamos National Laboratory, Los Alamos, NM, 1998.

[26] J. Miernik, G. Statham, L. Fabisinski, C. Maples, R. Adams, T. Polsgrove, S. Fincher, J. Cassibry, R. Cortez, M. Turner and T. Percy, "Z-Pinch fusion-based nuclear propulsion," *Acta Astronautica,* vol. 82, pp. 173-182, 2013.

[27] R. Adams, R. Alexander, J. Chapman, J. Fincher, S. Philips, A. Polsgrove, T. Wayne, B. Patton, G. Statham, S. White and Y. Thio, "Conceptual Design of In-Space Vehicles for Human Exploration of the Outer Planets," NASA Technical Rept. 2003-212691, 2003.

[28] W. Moeckel, "Propulsion Systems for Manned Exploration of the Solar System," NASATM-X-1864, 1969.

[29] W. Moeckel, *Journal of Spacecraft and Rockets,* vol. 9, no. 12, p. 863, 1972.

[30] M. Stanic, J. Cassibry and R. Adams, "Project Icarus: Analysis of Plasma jet driven Magneto-Inertial Fusion as potential primary propulsion driver for the Icarus probe," *Acta Astronautica,* vol. 86, pp. 47-54, 2013.

[31] N. Schulze, "Fusion Energy for Space Missions in the 21st Century," NASA Office of Safety and Mission Quality, NASA Technical Memorandum TM4298.

[32] K. Long, R. Obousy and A. Hein, "Project Icarus: Optimisation of nuclear fusion propulsion for interstellar missions," *Acta Astronautica,* vol. 68, pp. 1820-1829, 2011.

[33] B. Wagstaff, "A Spaceship Named Orion," Air & Space, Smithsonian Institute, 1988.

[34] "Nuclear Pulse Space Vehicle Study," George C. Marshall Space Flight Center, Huntsville, AL, 1964.

[35] G. Dyson, "Project Orion: The True Story of the Atomic Spaceship," Henry Holt and Co., New York, NY, 2002.

[36] J. D. Balcomb, L. Booth, T. Cotter, J. Hedstrom, C. Robinson, T. Springer and C. Watson, "Nuclear Pulsed Space Propulsion Systems," LA-4541-MS, Los Alamos Scientific Laboratory, Los Alamos, NM, November 1970.

[37] R. Hyde, L. Wood and J. Nuckolls, "Prospects for rocket propulsion with laser-induced fusion microexplosions," AIAA Paper No. 72-1063, December 1972.

[38] C. Orth, "VISTA - A Vehicle for Interplanetary Space Transport Application Powered by Inertial Confinement Fusion.3," Lawrence Livermore National Laboratories: Livermore, California, 2003.

[39] R. A. Hyde, "A Laser Fusion Rocket for Interplanetary Propulsion," in *34th International Astronautical Federation*, Budapest, Hungary, 10-17 October 1983.

[40] F. Winterberg, "Rocket propulsion by thermonuclear micro-bombs ignited with intense relativistic electron beams," *Raumfahrtforschung,* vol. 15, pp. 208-217, 1971.

[41] A. Bond, A. Martin and et al., "Project Daedalus – The Final Report on the BIS Starship Study," *Journal of British Interplanetary Society,* 1978.

[42] K. Beals, M. Beaulieu, F. J. Dembia, J. Kerstiens, D. L. Kramer, J. R. West and J. A. Zito, "Project Longshot: An Unmanned Probe To Alpha Centauri," U S Naval Academy. NASA-CR-184718, 1988.

[43] R. Obousy, "Project Icarus: A Technical Review of the Daedalus Propulsion Configuration and Some Engineering Considerations for the Icarus Vehicle," in *Advanced Space Propulsion Workshop,* 2010.

[44] A. K. Martin, R. H. Eskridge, P. J. Fimognari and M. H. Lee, "FIREBALL: Fusion Ignition Rocket Engine with Ballistic Ablative Lithium Liner," *AIP Conference Proceedings,* vol. 813, no. 1, pp. 783-794, 2006.

[45] A. M. Buyki and et al, "Investigations of Thermonuclear Magnetized Plasma Generation in the Magnetic Implosion System MAGO," All-Russion Institute of Experimental Physics, Arzamas-16, Nizhny Novgorod Region, Russia.

[46] D. D. Ryutov and Y. C. F. Thio, "Solving the Stand-off Problem for Magnetized Target Fusion: Plasma Streams as Disposable Electrodes, Together with a Local Spherical Blanket," *Journal of Fusion Energy,* vol. 26, pp. 173-177, 2007.

[47] J. M. Taccetti and et al, "FRX-L: A Field-Reversed Configuration Plasma Injector for Magnetized Target Fusion," *Review of Scientific Instruments,* vol. 74, no. 10, pp. 4314-4323, October 2003.

[48] "FRX-L: A Plasma Injector for Magnetized Target Fusion," Los Alamos National Laboratory, [Online]. Available: http://fusionenergy.lanl.gov/Documents/FRX-L-Flyer.pdf. [Accessed 5 May 2018].

[49] J. P. Chittenden, P. Vincent, C. A. Jennings and A. Ciardi, "Hotspot ignition using a Z-pinch precursor plasma in a magneto-inertial ICF scheme," *AIP Conference Proceedings,* vol. 808, no. 1, pp. 335-338, 2006.

[50] M. E. Cuneo and et al, "Magnetically Driven Implosions for Inertial Confinement Fusion at Sandia National Laboratories," *IEEE Transactions on Plasma Science,* vol. 40, no. 12, pp. 3222-3245, December 2012.

[51] S. A. Slutz, M. C. Herrmann, R. A. Vesey, A. B. Sefkow, D. B. Sinars, D. C. Rovang, K. J. Peterson and M. E. Cuneo, "Pulsed-power-driven cylindrical liner implosions of laser preheated fuel magnetized with an axial field," *Physics of Plasmas,* vol. 17, p. 056303, 2010.

[52] M. R. Gomez and et al, "Experimental Demonstration of Fusion-Relevant Conditions in Magnetized Liner Inertial Fusion," *Physical Review Letters,* vol. 113, no. 15, p. 155003, 2014.

[53] K. A. Munson, U. Shumlak and B. A. Nelson, "Extreme ultraviolet light production from a ZaP Flow Z-Pinch xenon plasma," *Journal of Micro Nanolithography, MEMS, and MOEMS* , vol. 7, no. 1, p. 013003, January 2008.

[54] U. Shumlak, B. A. Nelson and B. Balick, "Plasma jet studies via the flow Z-pinch," *Astrophysics and Space Science,* vol. 307, no. 1, pp. 41-45, March 2007.

[55] R. Adams, "Pulsed Fission-Fusion (PuFF) Propulsion Concept," NASA, 30 March 2018. [Online]. Available: https://www.nasa.gov/directorates/spacetech/niac/2018_Phase_I_Phase_II/Pulsed Fission-Fusion_Propulsion_Concept. [Accessed 4 May 2018].

[56] "Introduction to LTD's," NASA, [Online]. Available: https://www.nasa.gov/puff/ltd. [Accessed 12 July 2018].

[57] T. Polsgrove, R. Adams, L. Fabisinski, S. Fincher, C. Maples, J. Miernik, T. Percy, G. Statham, M. Turner and J. Cassibry, "Z-Pinch Pulsed Plasma Propulsion Technology Development," NASA Marshall Space Flight Center, Huntsville, AL, 2010.

[58] "Fusion Propulsion and Power," University of Alabama in Huntsville, [Online]. Available: https://www.uah.edu/prc/capabilities/fusion-propulsion-power. [Accessed 9 July 2018].

[59] C. Sijoy and C. Shashank, "Conversion of plasma into electrical pulse by magnetic flux compression," *Fusion Engineering and Design,* vol. 86, pp. 174-182, 2011.

[60] Y. Nagamine and H. Nakashima, "Analysis of plasma behavior in a magnetic thrust chamber of a laser fusion rocket," *Fusion Technology,* vol. 35, p. 62–70, 1999.

[61] N. Sakaguchi, Y. Kajimura and H. Nakashima, "Thrust Efficiency Calculation for Magnetic Nozzle in Laser Fusion Rocket," *Transactions of the Japan Society for Aeronautical and Space Sciences,* vol. 48, no. 161, pp. 180-182, 2005.

[62] Y. Kajimura, R. Kawabuchi and H. Nakashima, "Control techniques of thrust vector for magnetic nozzle in laser fusion rocket," *Fusion Engineering and Design,* vol. 81, no. 23, pp. 2871-2875, 2006.

[63] N. Matsuda, A. Maeno, Y. Kajimura and H. Nakashima, "A magnetic nozzle chamber design for a laser fusion rocket based on impact fast ignition," in *14th International Congress on Plasma Physics*, Fukuoka, Japan, 2008.

[64] A. Maeno, T. Hanaya, N. Yamamotoz, H. Nakashima, S. Fujioka, A. Sunahara and T. Johza, "Preliminary Experiments for Demonstrating Magnetic Thrust Chamber Concept in Laser Fusion Rocket," in *31st International Electric Propulsion Conference,* Ann Arbor, Michigan.

[65] M. G. Haines, "A review of the dense Z-pinch," *Plasma Physics and Controlled Fusion,* vol. 53, 2011.

[66] P. V. Subhasha, S. Madhavan and S. Chaturvedi, "Effect of liner non-uniformity on plasma instabilities in an inverse Z-pinch magnetized target fusion system: liner-on-plasma simulations and comparision with linear stability analysis," *Physica Scripta,* vol. 77, no. 3, 2008.

[67] M. Laberge, S. Howard, D. Richardson, A. Froese, V. Suponitsky, M. Reynolds and D. Plant, "Acoustically driven Magnetized Target Fusion," in *IEEE 25th Symposium on Fusion Engineering*, San Francisco, CA, 2013.

[68] "Our Technology-How does Magnetized Target Fusion Work?," General Fusion, 2018. [Online]. Available: http://generalfusion.com/technology-magnetized-target-fusion/. [Accessed 13 July 2018].

[69] M. Laberge, "Magnetized Target Fusion with a Spherical Tokamak," *Journal of Fusion Energy*, 2018 https://doi.org/10.1007/s10894-018-0180-3.

[70] M. Laberge, "Magnetized Target Fusion at General Fusion," in *25th IEEE Symposium on Fusion Engineering*, 2017.

[71] P. J. Turchi, S. D. Frese and M. H. Frese, "Stabilized LIner Compressor for Low-Cost Controlled Fusion at Megagauss Field Levels," *IEEE Transactions on Plasma Science,* vol. 45, no. 10, pp. 2800-2809, October 2017.

[72] D. Kirtley and J. Slough, "Macron Formed Liner as a Practical Method for Enabling Magneto-Inertial Fusion," *Journal of Fusion Energy,* vol. 29, no. 6, pp. 561-566, 2010.

[73] Y. C. F. Thio, C. E. Knapp, R. C. Kirkpatrick, R. E. Siemon and P. J. Turchi, "A Physics Exploratory Experiment on Plasma Liner Formation," *Journal of Fusion Energy,* vol. 20, no. 1-2, pp. 1-11, 2001.

[74] Y. C. F. Thio, E. Panarella, R. C. Kirkpatrick, P. Parks and G. Schmidt, "Magnetized Target Fusion in a Spheroidal Geometry With Standoff Drivers," in *Current Trends in International Fusion Research*, Ottawa, Canada, 1999.

[75] R. Samulyak, P. Parks and L. Wu, "Spherically symmetric simulation of plasma liner driven magnetoinertial fusion," *Physics of Plasmas,* vol. 17, no. 9, pp. 1-10, 2010.

[76] Y. Thio, B. Freeze, R. Kirkpatrick, B. Landrum, H. Gerrish and G. Schmidt, "High-Energy Space Propulsion based on Magnetized Target Fusion," in *35th AIAA/ASME/SAE/ASEE Joint Propulsion Conference and Exhibit*, Los Angeles, California, 1999.

[77] J. T. Cassibry, "Numerical Modeling Studies of a Coaxial Plasma Accelerator as a Standoff Driver for Magnetized Target Fusion, a Disertation," University of Alabama in Huntsville, Huntsville, AL, 2004.

[78] C. E. Knapp and R. C. Kirkpatrick, "Possible energy gain for a plasma-liner-driven magneto-inertial fusion concept," *Physics of Plasmas,* vol. 21, no. 7, pp. 1-6, 2014.

[79] J. T. Cassibry, M. Stanic and S. C. Hsu, "Ideal hydrodynamic scaling relations for a stagnated imploding spherical plasma liner formed by an array of merging plasma jets," *Physics of Plasmas*, vol. 20, no. 3, pp. 1-12, 2013.

[80] J. Cassibry, M. Stanic and S. Hsu, "Ideal hydrodynamic scaling relations for a stagnated imploding spherical plasma liner formed by an array of merging plasma jets," *Journal of Plasma Physics,* vol. 20, p. 032706, 2013.

[81] J. F. Santarius, "Compression of a spherically symmetric deuterium-tritium plasma liner onto a magnetized deuterium-tritium target," *Physics of Plasmas*, vol. 19, no. 7, pp. 072705-02705-9, 2012.

[82] H. Kim, R. Samulyak, L. Zhang and P. Parks, "Influence of atomic processes on the implosion of plasma liners," *Physics of Plasmas,* vol. 19, no. 8, pp. 1-12, 2012.

[83] H. Kim, L. Zhang, R. Samulyak and P. Parks, "On the structure of plasma liners for plasma jet induced magnetoinertial fusion," *Physics of Plasmas,* vol. 20, no. 2, pp. 1-10, 2013.

[84] T. J. Awe, C. S. Adams, J. S. Davis, D. S. Hanna, S. C. Hsu and J. T. Cassibry, "One-dimensional radiation-hydrodynamic scaling studies of imploding spherical plasma liners," *Physics of Plasmas,* vol. 18, no. 7, pp. 1-11, 2011.

[85] J. S. Davis, S. C. Hsu, I. E. Golovkin, J. J. MacFarlane and J. T. Cassibry, "One-dimensional radiation-hydrodynamic simulations of imploding spherical plasma liners with detailed equation-of-state modeling," *Physics of Plasmas,* vol. 19, no. 10, pp. 1-8, 2012.

[86] J. Cassibry, M. Stanic, S. Hsu, F. Witherspoon and S. Abarzhi, "Tendency of spherically imploding plasma liners formed by merging plasma jets to evolve toward spherical symmetry," *Journal of Plasma Physics,* vol. 19, p. 052702, 2012.

[87] P. B. Parks, "On the efficacy of imploding plasma liners for magnetized fusion target compression," *Physics of Plasmas,* vol. 15, no. 6, pp. 1-12, 2008.

[88] S. Hsu, T. Awe, A. Brockington, J. Case, J. Cassibry, G. Kagan, S. Messer, M. Stanic, X. Tang, D. Welch and F. Witherspoon, "Spherically Imploding Plasma Liners as a Standoff Driver for Magneto-Inertial Fusion," *IEEE Transactions: Plasma Science,* 2012.

[89] S. C. Hsu, T. J. Awe, S. Brockington, A. Case, J. T. Cassibry, G. Kagan, S. J. Messer, M. Stanic, X. Tang, D. R. Welch and F. D. Witherspoon, "Spherically Imploding Plasma Liners as a Standoff Driver for Magnetoinertial Fusion," *IEEE Transactions on Plasma Science,* vol. 40, no. 5, pp. 1287-1298, 2012.

[90] E. C. Merritt, A. L. Moser, S. C. Hsu, J. Loverich and M. Gilmore, "Experimental Characterization of the Stagnation Layer between Two Obliquely Merging Supersonic Plasma Jets," *Physical Review Letters,* vol. 111, no. 8, 2013.

[91] E. C. Merritt, A. L. Moser, S. C. Hsu, C. S. Adams, J. P. Dunn, A. M. Holgado and M. A. Gilmore, "Experimental evidence for collisional shock formation via two obliquely merging supersonic plasma jets," *Physics of Plasmas,* vol. 21, no. 5, 2014.

[92] S. C. Hsu, S. J. Langendorf, J. P. Dunn, K. C. Yates, M. A. Gilmore, F. D. Witherspoon, S. Brockington, A. Case, E. Cruz and Y. C. F. Thio, "Characterizing an Octant of a Spherically Imploding Plasma Liner as an MIF Driver," in *Bulletin of the American Physical Society Vol. 62. 12*, Milwaukee, WI, 2017.

[93] K. Schillo, J. Cassibry, M. Rodriguez and S. Thompson, "Test Suite for Smooth Particle Hydrodynamic Code Relevant to Spherical Plasma Liner Formation and Implosion," *Journal of Nuclear Engineering and Radiation Science,* Accepted for publication August 2018.

[94] S. C. Hsu, S. J. Langendorf, K. C. Yates, J. P. Dunn, S. Brockington, A. Case, E. Cruz, F. D. Witherspoon, M. A. Gilmore, J. T. Cassibry, R. Samulyak, P. Stoltz, K. Schillo, W. Shih, K. Beckwith and Y. C. F. Thio, "Experiment to Form and

Characterize a Section of a Spherically Imploding Plasma Liner," *IEEE Transactions on Plasma Science,* vol. PP, no. 99, pp. 1-11, 2017.

[95] M. A. Rodriguez and J. T. Cassibry, "A 3-D Smoothed-Particle Hydrodynamics Model of Electrode Erosion," *IEEE Transactions on Plasma Science,* vol. 45, no. 11, pp. 3030-3037, 2017.

[96] J. T. Cassibry, R. Cortez, C. Cody, S. Thompson and L. Jackson, "Three dimensional modeling of pulsed fusion for propulsion and terrestrial power using smooth particle fluid with Maxwell equation solver (SPFMax)," in *53rd AIAA/SAE/ASEE Joint Propulsion Conference, AIAA Propulsion and Energy Forum,* Atlanta, GA, 2017.

[97] P. F. Hopkins, "A New Class of Accurate, Mesh-Free Hydrodynamic Simulation Methods," *Monthly Notices of the Royal Astronomical Society,* vol. 450, no. 1, pp. 53-110, June 2015.

[98] K. Schillo, *Three-Dimensional Modeling of an Ideal Nozzle for Advanced Propulsion, a thesis,* Huntsville, Al: University of Alabama in Huntsville, May 2014.

[99] J. Cassibry, B. Winterling and K. Schillo, "Pulsed Magnetic Nozzle for Fusion Propulsion," *Journal of the British Interplanetary Society.*

[100] J. T. Wendt and J. D. Anderson, "Governing Equations of Fluid Dynamics," in *Computational Fluid Dynamics: An Introduction, 3rd Edition,* Springer-Verlag Berlin Heidelberg, 2009, pp. 15-51.

[101] U. Shumlak, T. W. Hussey and R. E. Peterkin, "Three-Dimensional Magnetic Field Enhancement in a Liner Implosion System," *IEEE Transactions on Plasma Science*, vol. 23, no. 1, pp. 83-88, February 1995.

[102] R. E. Peterkin, M. H. Frese and C. R. Sovinec, "Transport of Magnetic Flux in an Arbitrary Coordinate ALE Code," *Journal of Computational Physics*, vol. 140, pp. 148-171, 1998.

[103] J. D. Huba, "NRL Plasma Formulary," Naval Research Laboratory, Washington, D.C., 2016.

[104] J. J. MacFarlane, I. E. Golovkin and P. R. Woodruff, "HELIOS-CR – A 1-D radiation-magnetohydrodynamics code with inline atomic kinetics modeling," *Journal of Quantitative Spectroscopy and Radiative Transfer*, vol. 99, no. 1-3, pp. 381-397, 2006.

[105] L. S. Brown, D. L. Preston and R. L. J. Singleton, "Charged particle motion in a highly ionized plasma," *Physics Reports*, vol. 410, no. 4, pp. 237-333, May 2005.

[106] C. K. Li and R. D. Petrasso, "Charged-Particle Stopping Powers in Inertial Confinement Fusion Plasmas," *Physical Review Letters*, vol. 70, no. 20, pp. 3059-3062, May 2993.

[107] K. A. Long and N. A. Tahir, "Theory and calculation of the energy loss of charged particles in inertial confinement fusion burning plasmas," *Nuclear Fusion*, vol. 26, no. 5, pp. 555-592, 1986.

[108] D. B. Harris and G. H. Miley, "Burn performance of inertial confinement fusion targets," *Nuclear Fusion,* vol. 28, no. 1, pp. 25-42, 1988.

[109] P. E. Grabowski, M. P. Surh, D. F. Richards, F. R. Graziani and M. S. Murillo, "Molecular dynamics simulations of classical stopping power," *Physical Review Letters,* vol. 111, no. 21, p. 215002, 19 November 2913.

[110] R. J. Cortez and J. T. Cassibry, "Stopping power in D6Li plasmas for target ignition studies," *Nuclear Fusion,* vol. 58, no. 2, p. 026009, 2017.

[111] R. J. Cortez, *Physics of Ignition and Burn Wave Propagation in Advanced Thermonuclear Fusion Targets: a dissertation,* Huntsville, Al: University of Alabama in Huntsville, 2018.

[112] R. Gingold and J. Monaghan, "Smoothed particle hydrodynamics: theory and application to non-spherical stars," *Monthly Notices of the Royal Astronomical Society,* vol. 181, pp. 375-389, 1977.

[113] L. Lucy, "A numerical approach to the testing of the fission hypothesis," *The Astronomical Journal,* vol. 82, pp. 1013-1024, 1977.

[114] J. Monaghan, "Smoothed particle hydrodynamics," *Reports on Progress in Physics,* vol. 68, pp. 1703-1759, 2005.

[115] D. J. Price, "Smoothed particle hydrodynamics and magnetohydrodynamics," *Journal of Computational Physics,* vol. 231, no. 3, pp. 759-794, 2012.

[116] G. Liu and M. Liu, Smoothed Particle Hydrodynamics: A Meshfree Particle Method, 2003.

[117] M. B. Liu and G. R. Liu, "Smoothed Particle Hydrodynamics (SPH): an Overview and Recent Developments," *Archives of Computational Methods in Engineering,* vol. 17, no. 1, pp. 25-76, March 2010.

[118] J. Hongbin and D. Xin, "On criterions for smoothed particle hydrodynamics kernels in stable field," *Journal of Computational Physics*, vol. 202, no. 2, pp. 699-709, 2005.

[119] L. D. G. Sigalotti, H. Lopez, A. Donoso, E. Sira and J. Klapp, "A shock-capturing SPH scheme based on adaptive kernel estimation," *Journal of Computational Physics*, vol. 212, p. 124–149, 2006.

[120] D. J. Price, "Magnetic fields in Astrophysics, a thesis," Institute of Astronomy and Churchill College, University of Cambridge, Cambridge, UK, 2004.

[121] M. Prakash and P. W. Cleary, "Three dimensional modelling of lava flow using Smoothed Particle Hydrodynamics," *Applied Mathematical Modelling,* vol. 35, pp. 3021-3035, 2011.

[122] R. A. Gingold and J. J. Monaghan, "Smoothed particle hydrodynamics: theory and application to non-spherical stars," *Monthly Notices of the Royal Astronomical Society,* vol. 181, pp. 375-389, 1977.

[123] R. Fatehi and M. T. Manzari, "Error estimation in smoothed particle hydrodynamics and a new scheme for second derivatives," *Computers and Mathematics with Applications,* vol. 61, no. 2, pp. 482-498, 2011.

[124] P. Randles and L. Libersky, "Smoothed Particle Hydrodynamics: some recent improvements and applications," *Computer Methods in Applied Mechanics and Engineering,* vol. 139, pp. 375-408, 1996.

[125] J. Bonet and T. Lok, "Variational and momentum preservation aspects of smooth particle hydrodynamics formulations," *Computer Methods in Appliled Mechanics and Engineering,* vol. 180, no. 1, pp. 97-115, 1999.

[126] J. Vila, "On particle weighted methods and Smoothed Particle Hydrodynamics," *Mathematical Models and Methods in Applied Sciences,* vol. 9, no. 2, pp. 161-210, 1999.

[127] L. Brookshaw, "A method of calculating radiative heat diffusion in particle simulations," *Astronomical Society of Australia,* vol. 6, pp. 207-210, 1985.

[128] M. Basa, N. J. Quinlan and M. Lastiwka, "Robustness and accuracy of SPH formulations for viscous flow," *International Journal for Numerical Methods in Fluids,* vol. 60, pp. 1127-1148, 2009.

[129] S. J. Watkins, A. S. Bhattal, N. Francis, J. A. Turner and A. P. Whitworth, "A new prescription for viscosity in Smoothed Particle Hydrodynamics," *Astronomy and Astrophysics,* vol. 119, pp. 177-187, 1996.

[130] J. H. Jeong, M. S. Jhon, J. S. Halow and J. v. Osdol, "Smoothed particle hydrodynamics: Applications to heat conduction," *Computer Physics Communications,* vol. 153, no. 1, pp. 71-84, 2003.

[131] J. P. Morris, J. F. Patrick and Y. Zhu, "Modeling Low Reynolds Number Incompressible Flows Using SPH," *Journal of Computational Physics,* vol. 136, pp. 214-226, 1997.

[132] W. Noh, "Errors for Calculations of Strong Shocks Using an Artificial Viscosity and an Artificial Heat Flux," *Journal of Computational Physics,* vol. 72, pp. 78-120, 1986.

[133] J. Castor, Radiation Hydrodynamics, Cambridge University Press, 2004.

[134] L. F. Shampine and M. W. Reichelt, "The MATLAB ODE Suite," *SIAM Journal on Scientific Computing,* vol. 18, pp. 1-22, 1997.

[135] J. H. VanSant, "Conduction Heat Transfer Solutions," UCRL-52863-Rev. 1, Lawrence Livermore National Laboratory, CA, 1983.

[136] J. J. MacFarlane, I. E. Golovkin and P. R. Woodruff, "HELIOS-CR-A 1-D Radiation-Magnetohydrodynamics Code with Inline Atomic Kinetics Modeling," *Journal of Quantitative Spectroscopy and Radiative Transfer,* vol. 99, no. 1-3, pp. 381-397.

[137] Q. Zhu, L. Hernquist and Y. Li, "Numerical Convergence in Smoothed Particle Hydrodynamics," *The Astrophysical Journal,* vol. 800, no. 6, February 2015.

[138] J. D. Anderson, Fundamentals of Aerodynamics, Second Edition, New York City, NY: McGraw-Hill, Inc., 1991.

[139] R. Liska and B. Wendroff, "Comparison of Several Different Schemes on 1D and 2D Test Problems for the Euler Equations," *SIAM Journal on Scientific Computing,* vol. 25, no. 3, pp. 995-1017, 2003.

[140] D. Balsara, "Divergence-Free Adaptive Mesh Refinement for Magnetohydrodynamics," *Journal of Computational Physics,* vol. 174, no. 2, pp. 614-648, 2001.

[141] J. Anderson, Modern Compressible Flow, Third Edition, Chapter 4, New York, NY: McGraw-Hill, 2003.

[142] G. I. Taylor and A. E. Green, "Mechanism of the Production of Small Eddies from Larger Ones," *Proceedings of the Royal Society of London. Series A, Mathematical and Physical Sciences,* vol. 158, no. 895, pp. 499-521, February 1937.

[143] J. R. DeBonis, "Solutions of the Taylor-Green Vortex Problem Using High-Resolution Explicit Finite Difference Methods," Glenn Research Center, Cleveland, Ohio, February 2013.

[144] B. S. Adami, X. Y. Hu and N. A. Adams, "Simulating three-dimensional turbulence with SPh," Center for Turbulence Research, 2012.

[145] A. Kajzer, J. Pozorski and K. Szwec, "Large-eddy simulations of 3D Taylor-Green vortex: comparison of Smoothed Particle Hydrodynamics, Lattice Boltzman and Finite Volume Methods," *Journal of Physics: Conference Series 530,* 2014.

[146] M. Deserno, "How to generate equidistributed points on the surface of a sphere," Max Planck Institute for Polymer Research, Mainz, Germany, 2004.

[147] J. D. Lindl, "Physics of Ignition for ICF Capsules," in *Inertial Confinement Fusion Course and Workshop*, Varenna, Italy, 1988.

[148] R. C. Kirkpatrich and I. R. Lindemuth, "Magnetized Target Fusion: An Overview of the Concept," in *Current Trends in International Fusion Research*, Panarella, Plenum Press, 1997, pp. 319-332.

[149] S. Thompson, *Lindl-Widner diagrams for plasma liner driven magneto-inertial fusion, a thesis,* Huntsville, AL: University of Alabama in Huntsville, 2007.

[150] E. W. Weisstein, "Spherical Harmonic," From MathWorld--A Wolfram Web Resource, [Online]. Available: http://mathworld.wolfram.com/SphericalHarmonic.html. [Accessed 7 November 2018].

[151] A. Politis, "Real/Complex Spherical Harmonic Transform, Gaunt Coefficients and Rotations," 13 November 2016. [Online]. Available: https://www.mathworks.com/matlabcentral/fileexchange/43856-real-complex-spherical-harmonic-transform-gaunt-coefficients-and-rotations. [Accessed 8 November 2018].

[152] P. W. McKenty, V. N. Goncharov, R. P. Town, S. Skupsky, R. Betti and R. L. McCrory, "Analysis of direct-drive ignition capsule designed for the National Ignition Facility," *Physics of Plasmas,* vol. 8, no. 5, pp. 2315-2322, May 2001.

[153] S. R. Nagel, S. W. Haan, J. R. Rygg, M. Barrios, L. R. Benedetti, D. K. Bradley, J. E. Field, B. A. Hammel, N. Izumi, O. S. Jones, S. F. Khan, T. Ma, A. E. Pak, R. Tommasini and R. P. J. Town, "Effect of the mounting membrane on shape in inertial confinement fusion implosions," *Physics of Plasmas,* vol. 22, no. 2, p. 022704, 2015.

[154] R. Tommasini and et al., "Tent-induced perturbations on areal density of implosions at the National Ignition Facility," *Physics of Plasmas,* vol. 22, no. 5, p. 056315, May 2015.